Mechanics of Biological Materials, Structures and Tissues at Multiple Scales

by

Yue Liu

B.Sc., University of Science and Technology of China,
P. R. China, 2014

A dissertation submitted in partial fulfillment of the

requirements for the Degree of Doctor of Philosophy

in the School of Engineering at Brown University

Providence, Rhode Island

May 2020

This dissertation by Yue Liu is accepted in its present form by

the School of Engineering as satisfying the

dissertation requirement for the degree of Doctor of Philosophy.

Date_____ _____

Prof. Huajian Gao, Advisor

Recommended to the Graduate Council

Date_____ _____

Prof. David Henann, Reader

Date_____ _____

Prof. Ian Wong, Reader

Approved by the Graduate Council

Date_____ _____

Prof. Andrew G. Campbell

Dean of the Graduate School

Vita

Yue Liu was born June 29, 1994 in Nanchang, Jiangxi Province, P. R. China. He attended University of Science and Technology of China through the Special Class for the Gifted Young in 2010, and received the B.Sc. in Theoretical and Applied Mechanics, Department of Modern Mechanics in 2014. Upon graduation, he started his graduate study in the Solid Mechanics group at Brown University. His research mainly focused on mechanics of biological tissues, structures and materials.

Acknowledgments

First, I would like to express my gratitude to my PhD advisor, Prof. Huajian Gao, for all his mentoring and advising during the last five years. It was his patience and constant support that encouraged me to move forward. His unparalleled insights and vision for science, persistent passion for research and high standard for work set an incredible example for me to learn from, both for the years past and the future to come.

I would also like to thank my dissertation committee members, Prof. David Henann and Prof. Ian Wong, who generously spend their time reading my thesis and offering advices. I also want to thank the entire faculty of Mechanics of Solids at Brown University for the providing the wonderful education and research environment. Thanks also the administrative staffs at School of Engineering for providing support.

My research works benefited greatly from my collaborators around the world and fellow colleagues at Brown. Most of my works were conducted in collaboration with experimentalist, and I'm sincerely grateful for Prof. Jun Liao, Prof. Lei Yang, Prof. Ning Sun and Prof. Sang Ho Oh for their professional collaboration and inspiring discussions. Many thanks for Dr. Xin Yi, Dr. Wenpeng Zhu, Dr. Fatemeh Ahmadpoor, Dr. Guijin Zou, and many other group members who shared their valuable experience and insightful discussions with me.

Finally, I want to thank my families with my whole heart, for all the love and support they offered me. They gave me the light when the road was dark, and covered me with warmth when the wind was cold. I would never be able to travel such a long way without them.

Contents

List of Tables

List of Figures

Chapter 1

Introduction

1.1. Brief overview of mechanics in biological tissues and materials

Mechanical integrity is one of the most important goals which biological tissues and biomaterials aim to achieve in order to support the life processes inside a living organism. A variety of mechanical structures and mechanisms are adopted from the nanoscale to the level of organisms, and mechanics plays an essential role. Understanding of these mechanisms provides us valuable insights for developing medical applications that restore damaged mechanical integrity and designing engineering materials for which mechanical integrity is vital. Conversely, we can also specifically attack the mechanical integrity to kill undesired biological organisms such as bacteria.

On the macroscopic scale, a living system can protect itself from mechanical damage via introducing pre-strain into its soft tissue through growth or other development processes (1, 2). Most constituents of those tissues such as collagen fibers and muscle fibrils exhibit strong exponential-like stiffening behavior (3-6), and thus pre-strain can effectively increase their tangential stiffness under physiological conditions (7), sometimes even up to three orders (8) and therefore reduce the likelihood of damage. Pre-strain has been revealed in many organs and tissues. Three decades ago, both arteries and hearts were found to possess significant pre-strains as they formed open angles when cut apart (9-11). Recently, the epicardium layer covering the left ventricle was also found pre-strained *in vivo*, which

could significantly reduce the myocardial stress and limit over-filling (12). In cartilage, the pre-strain could increase both cell viability and the local resistance against cracks (13). Therefore, to develop treatment methods for supporting or restoring tissue's or organ's mechanical integrity, pre-strain is a critical factor to consider. For example, in the anterior cruciate ligament reconstruction, the graft pre-strain requires careful tuning to restore the joint mechanics (14, 15). Moreover, a viscoelastic epicardial patch was specifically designed to mechanically support infarct heart with a self-adaptive pre-strain and showed optimal therapeutic efficacy (16).

As on the microscopic level, microstructure can be a critical factor governing the mechanics of biomaterials. To improve and protect their mechanical integrity, biomaterials adopt a wide spectrum of structural strategies such as limiting the length scale to tens of nanometers to become flaw-insensitive (17), employing specific deformation mechanisms like tension-shear chain (18, 19) together with a hierarchical structure (20-24), and tuning its gradation (25) and anisotropy (26) to optimize their mechanical properties including strength and toughness by orders of magnitude compared with their individual constituents. By leveraging microstructure, biomaterials can incorporate properties that were generally believed to compromise their mechanical integrity. For instance, limpet teeth exhibit an unusual combination of both extraordinary strength (27) and a negative Poisson's ratio, as the latter tends to require voids in the structure which weakens the material. Inspired by these microstructural strategies, new engineering composite materials can be engineered and designed with robust and multifunctional mechanical properties (28-31).

We can now develop specific strategies to kill biological targets like bacteria by degrading their mechanical integrity. A lipid bilayer membrane is a defining mechanical

structure in living cells, and a potentially effective target. During recent years such membrane-targeting antibiotics designed to disrupt membrane integrity have started to acquire increasing research interests. Starting with daptomycin (32), the first clinically successful membrane-targeting antibiotics, a line of membrane active agents were discovered like telavancin (33), oritavancin (33) and etc. They can adopt a variety of mechanisms such as permeabilization, depolarization and lipid extraction (33-38). By targeting the outmost mechanical structure, these agents are capable of killing bacteria even in their dormant state, or "persister", in contrast to conventional antibiotics(39). In two recent studies (40, 41), the effects of two agents on membranes were captured with a camera, where vesicles showed a large quantity of domain aggregations, followed by bursting. Since the underlying mechanism remains unclear, these observations call for further mechanistic investigation to provide systematic guidance for future agent design.

1.2. Thesis organization

In this thesis, we investigate the role of mechanical behaviors inside various biological tissues, structures and materials at different scales, including deformation, remodeling, functioning and how they preserve/challenge the mechanical integrity. This thesis consists of six chapters and is organized as follows.

Chapter 1 is an overview introduction about the mechanics and mechanical integrity of biological tissues and materials, specifically what mechanical and design strategies can be learned from those systems and how we can utilize them.

In Chapter 2, we investigate an experimentally observed pre-strain from the epicardial layer on the porcine left ventricle. We first quantify the pre-strain value from experimental

data and then incorporate the data of both the pre-strain and biaxial tension into a finite element model to characterize the mechanical confinement from the pre-strain on the ventricular cavity volume and the first principle stress in the myocardium.

In Chapter 3, we aim to study the interaction between a pre-strained gel patch and infarct human left ventricle. We conduct finite element modeling of both the ventricle and gel to reveal the critical effect of pre-strain on both reducing the stroke volume and limiting the long-term ventricular dilatation. We point out that a viscoelastic, instead of elastic, gel patch at the gel point can provide the optimal mechanical support of the ventricle after myocardial infarction (MI). In experiments the designed material was fabricated and applied on post-MI rats and showed a significant therapeutic efficacy.

In Chapter 4, we focus on the characterization and modeling of auxetic limpet teeth. We employ digital image correlation to reveal its auxeticity and obtain its spin pattern during deformation. The spin pattern is then correlated with the microstructure of the limpet teeth and sheds light on a spin-dominated deformation mechanism resulting in auxeticity. A finite element model, inspired by and aimed to mimic the experimentally observed deformation mechanism, is constructed and further characterized by micropolar elasticity theory. The importance and the connection with auxeticity of micropolar elasticity in the constructed model is discovered.

In Chapter 5, we study the pore growth on a liquid membrane with an aggregated inclusion domain through both theoretical and numerical approaches. We prove mathematically that the domain interface and curvature can contribute concomitantly to promote the pore growth, while a smooth gradient inter-domain boundary tends to resist the pore growth compared with a sharp interface. Molecular dynamics simulations are

performed to confirm the drop of both critical tension and work of rupture as a result of both the inter-domain line tension and intrinsic curvature.

Chapter 6 concludes the entire thesis with major scientific findings and future perspectives.

Chapter 2

Mechanical confinement on ventricle through epicardial pre-strain

2.1 Introduction

Between 2011 and 2014, approximately 6.5 million adults experienced heart failure in the US, representing a major healthcare burden (42). After coronary artery blockage, the downstream cardiomyocytes die and lead to myocardial infarction (MI), commonly known as heart attack (43-45). This subsequently results in expansion of the infarcted region, formation of scar tissues, left ventricular wall thinning and dilatation, loss of cardiac function, and eventually fatal heart failure (HF) (46-53). Current therapies for HF provide modest symptom relief but fail in preventing dilation and improving long-term survival outcomes (54-56). The collagenous, parietal pericardium sac of the heart is not sufficient in preventing ventricular dilation during HF (57). As a result, passive prosthetic devices that wrap the heart, such as woven textile (CorCap), Nitinol mesh (Paracor), and polyurethane half-ellipsoid balloon (Plyzen) (58-60), have been developed to limit ventricular dilation. During the past 20 years, passive prosthetic wrap devices have demonstrated an encouraging clinical safety profile and improved left ventricle (LV) function. However, they still face challenges with respect to limited reverse LV remodeling and long-term ventricular function or survival (58-60). Improvements in elastic support device development and their modes of application can only be done once ventricular mechanics and its post-MI alteration are better understood (46-53, 58-60).

The heart ventricular wall has three anatomically distinguishable layers: the epicardium, myocardium, and endocardium. The epicardium (also known as visceral pericardium) is the outermost thin layer that is largely made of elastin fibers along with a network of collagen (61-64). The myocardium is the thick middle layer that fuses immediately with the epicardium and forms the main body of the heart wall. Myocardium contains mainly heart muscle fibers, which are delicately bound together by a network of type I and type III collagen, and the amount of elastin fibers in the myocardial ECM is relatively sparse (62, 64). The innermost layer of the heart wall is the endocardium, which is also dominant with elastin fibers along with a network of collagen (62-64). The endocardium lines the chambers and controls the heart contraction through electrical signals conducted by the Purkinje fibers (63).

Previous research has mainly focused on myocardium and the myocardial ECM (types I and III collagen as the dominant components). These studies have shown that heart muscle fibers interact with the myocardial ECM to perform the active contraction in systole and passive stretch in diastole in an effective and efficient manner. The myocardial ECM binds heart muscle fibers together, enables the overall architecture of multilayered helical orientation, provides tethering among muscle fibers, and prevents the over-stretch of muscle fibers during LV diastolic expansion (64-70). However, the mechanical properties and the impact of epicardial layer to the LV during heart contraction and diastole have so far been largely ignored. From a material perspective, the previous cardiac ECM studies mainly focused on the collagen; the epicardial layer, with elastin as the dominant material component, has not been well investigated. Despite a few studies that hint that elastin may have an important role in cardiac mechanics and function (61, 64), the biological and

mechanical functionalities of elastin in the heart are poorly understood when compared to the knowledge of elastin in other dynamic soft tissues, such as blood vessels, lung, and ligaments (64). In those dynamic tissues, elastin provides long-range deformability, elastic passive recoil, and efficiency in storing and releasing energy during dynamic loading.

During our dissection of tissue samples from the heart surface, which were consisting of an epicardial layer and cardiac muscle, we discovered an interesting phenomenon that the bi-layered LV surface strip always curls towards the epicardial side. This surface curling reveals that there is residual stress in the epicardial layer. Once dissected off the heart, the contraction of the epicardial layer bends the LV surface strip and a curling morphology occurs. Residual stress in an organ is the stress that remains in tissue after all external loads are removed (71). A well-known example is the residual stress and strain in blood vessels. After the blood vessel is cut into ring segments, a single radial cut releases the residual stress in the blood vessel wall. The closed ring configuration cannot be maintained, and the ring opens up, forming an arc conformation (71).

The concepts of residual stress have also been applied to the rat left ventricular wall. Omens and Fung showed that, if a radial cut was applied to an equatorial slice of a rat heart, the rat's left ventricle exhibited an open angle-like morphology (~ 30°), indicating the existence of residual stress in the whole ventricular wall (72). Using finite growth framework with fixed-point iteration, Genet *et al* analyzed and proposed that the residual stress of ventricular wall was likely induced by the growth of the organ (73). Jobsis *et al* performed a study on the residual stress of the left ventricle by examining the gross opening angle of the porcine left ventricle wall (61). They showed that peeling-off or disruption of the epicardium reduced the gross opening angle of the left ventricular wall, implying the

likely contribution of the epicardium to the ventricular wall residual stress (61).

In this chapter, we revealed and quantitatively assessed the pre-straining and residual stresses exerted by the epicardial layer on the heart left ventricle (LV). A finite element (FE) model was also constructed and analyzed to investigate the mechanical role of epicardial pre-straining in ventricular diastolic expansion. Our study addresses a critical question in ventricular biomechanics, i.e., what is the biomechanical role of the epicardial layer and how does epicardial pre-strained confinement contribute to cardiac function. The obtained knowledge will help design new therapies to target the maintenance/recreation of this ventricle confinement interface in diseases such as myocardial infarction and heart failure. This chapter is finished in collaboration with Prof. Jun Liao and published in Ref. (12).

2.2 Model and methods

2.2.1 Estimation of the regional residual stresses of the epicardial layer

A four-step estimation method was developed to quantify the regional residual stresses of the LV epicardial layer on the unpressurized intact porcine heart. The four steps were as follows: (i) quantify the epicardial pre-strains existing on the unpressurized intact heart; (ii) use a biaxial testing machine to capture the stress-strain curves along the circumferential and longitudinal directions of the dissected epicardial layer (with a 0.5g tare load required by software load control protocol); (iii) adjust the biaxial stress-strain curves to the 0g load reference status; (iv) for each location, estimate the residual stresses along the circumferential and longitudinal directions from the adjusted biaxial curves via the pre-strains reported from step (i).

2.2.2 Estimation of the pre-strains of the epicardial layer

Fresh porcine hearts (~ 6-month old, Yorkshire) were transported from a local abattoir to the laboratory. Seven epicardial locations (~ 10 mm × 10 mm) were chosen from the left ventricle (three from the basal region, three from the middle region, and one from the apex point) (**Fig. 2.1b**). By choosing ~10 mm × 10 mm sample dimension for prestrain measurement, we covered enough tissue in each anatomically-distinguishable location. If, instead, a much smaller sample dimension (e.g., ~5 mm × 5 mm) is used, the image resolution of maker-enclosed area will be much lower, which will decrease the accuracy of pre-strain measurement.

Before dissection, four markers were glued onto the surface of each location of the unpressurized intact left ventricle using a minimal amount of cyanoacrylate glue. The ruler with actual size was printed onto a paper and placed onto the left ventricle surface, perfectly fitting the surface curvature. By this way, the readings of sample dimensions between markers on the unpressurized intact heart can be accurate, avoid being skewed by using a straight ruler for a curved surface (**Fig. 2.1b**-left panel). Digital pictures of each location were then taken to record the *in situ* marker dimensions. Note that the shape of the unpressurized intact heart experienced no changes during measurement. Thus, there was no geometrical or surface distortion of left ventricle during the *in situ* marker dimension measurement. After the *in situ* measurement, the epicardial layer of each location was dissected, gently removed of the heart muscles, and immersed in 1X PBS in a petri-dish to ensure a stress-free status. Ruler with actual size was printed on a transparent film and then placed beside the stress-free epicardial layer sample. Digital pictures of each stress-free sample were taken to record the stress-free marker dimensions (**Fig. 2.1b**-right panel). For

each location, sample size is N = 5.

The x and y coordinates of each marker were first acquired using ImageJ. For each sample, we converted the length in pixel to length in mm using each actual size ruler. For the markers on the heart surface, the coordinates were (x_1, y_1), (x_2, y_2), (x_3, y_3), and (x_4, y_4) (**Fig. 2.1b**). For the markers on the stress-free samples, the coordinates were (x_1', y_1'), (x_2', y_2'), (x_3', y_3'), and (x_4', y_4') (**Fig. 2.1b**). To calculate the pre-strains (in the form of Green strain) of each location, we interpolated the displacements $\boldsymbol{u}_{(k)} = (x_k - x_k', y_k - y_k')$ of all 4 markers from stress-free (the reference configuration), to *in situ* states inside the sample using the first order shape function for quadrilateral element, as is commonly used for finite element method (**Eq. 2.1**, where k denotes the indices of 4 markers). Then based on such interpolation we computed the deformation gradient tensor (**Eq. 2.2**, where $\boldsymbol{I}$ is the unity tensor), which, by definition, will give us the Green strain tensor, as in **Eq. 2.3**. We calculated the area average of the Green strain tensor $\overline{\boldsymbol{E}}$, as in **Eq. 2.4** with Gaussian quadrature, and its components were used to estimate the pre-strains along the circumferential direction ($\varepsilon_X=\bar{E}_{xx}$) and longitudinal direction ($\varepsilon_Y=\bar{E}_{yy}$).

$$\boldsymbol{u}(\boldsymbol{x}') = \sum_{k=1}^{4} N^{(k)}(\boldsymbol{x}')\boldsymbol{u}_{(k)} \tag{2.1}$$

$$\boldsymbol{F}(\boldsymbol{x}') = \boldsymbol{I} + \frac{\partial \boldsymbol{u}(\boldsymbol{x}')}{\partial \boldsymbol{x}'} \tag{2.2}$$

$$\boldsymbol{E}(\boldsymbol{x}') = \frac{1}{2}(\boldsymbol{F}^T(\boldsymbol{x}')\boldsymbol{F}(\boldsymbol{x}') - \boldsymbol{I}) \tag{2.3}$$

$$\overline{\boldsymbol{E}} = \frac{1}{A}\int \boldsymbol{E}(\boldsymbol{x}')dA' \tag{2.4}$$

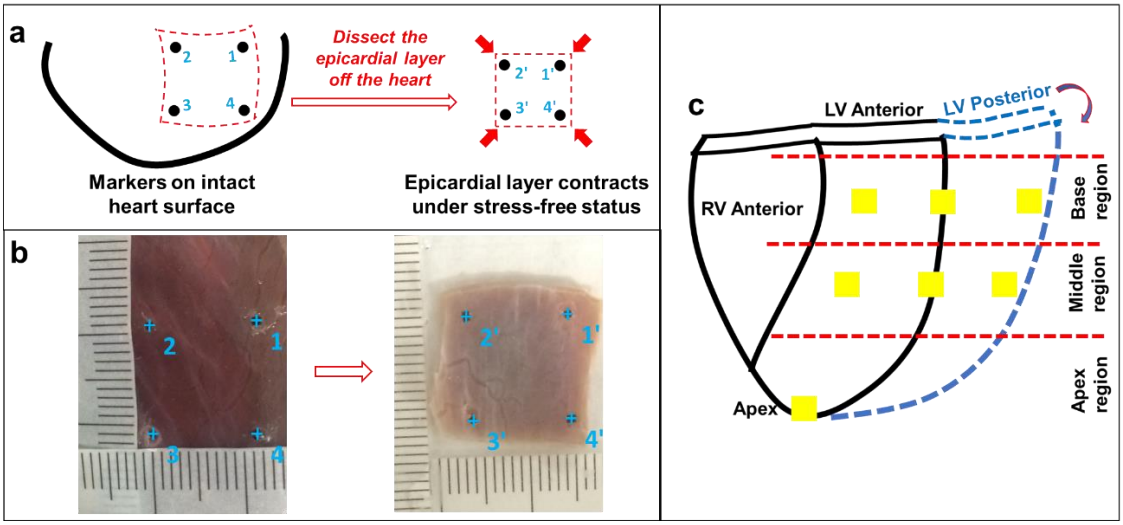

Figure 2.1. Schematic illustration shows the protocol to estimate the pre-strains of the epicardial layer on the unpressurized intact heart. (a) By putting four squarely-arranged markers on the epicardial surface of the unpressurized intact heart, we could obtain the *in situ* marker dimensions while the pre-strains existed. After dissecting the same region off the heart, the marker dimensions of the stress-free epicardial layer could be measured for the calculation of the pre-strains. (b) Markers tagged from ImageJ for *in situ* unpressurized intact heart (left panel) and stress-free epicardial sample (right panel). The ruler with actual size was printed on a paper. The paper ruler could be placed onto the left ventricle surface, perfectly fitting the left ventricle surface curvature (left panel). By this way, the readings of the real marker dimensions on the unpressurized intact heart can be accurate, without being skewed by using a straight ruler for a curved surface. By immersing the isolated epicardial layer in the 1X PBS in a petri-dish, we obtained the new marker dimension of the epicardial layer under stress-free status (right panel). Ruler with actual size was printed on the transparent film and then placed besides the stress-free epicardial layer sample (right panel). (c) Sample dissection plan for estimating pre-strains of the epicardial layer on the unpressurized intact heart.

2.2.3 Finite element (FE) modeling of left ventricle and epicardium

For simplicity, we used a truncated ellipsoid to represent the shape of porcine left ventricle (**Figure 2.3a**). The lengths of the semi-axes of the endocardial surface are $a_{endo} = 15mm$ and $b_{endo} = 39mm$, while those for the epicardial surface $a_{epi} = 30mm$ and $b_{epi} = 47mm$. The distance between the apex and the base plane is $h = 78mm$.

These geometrical parameters of left ventricle were obtained by averaging the measurements from four porcine hearts (~6-month old, Yorkshire). The myocardium part consisted of 16326 quadratic tetrahedral solid elements, and the epicardium was modeled as a shell covering the epicardial surface with 4430 quadratic shell elements with thickness of 1mm, consistent with the overall thickness of the epicardial samples we dissected for biaxial mechanical testing. The mesh density has been increased to check potential mesh dependency but no significant difference in result was observed.

To model the passive mechanical properties of the myocardium, we adopted the Holzapfel-Ogden model (6, 74):

$$\Psi = \mathrm{U}(J) + \bar{\Psi}_{iso}(\bar{I}_1) + \bar{\Psi}_{aniso}(\bar{I}_{4f}, \bar{I}_{4s}, \bar{I}_{8fs})$$

$$\mathrm{U}(J) = \frac{\mu_K}{2}(\ln J)^2$$

$$\bar{\Psi}_{iso}(\bar{I}_1) = \frac{a}{2b}(\exp[b(\bar{I}_1 - 3)] - 1)$$

$$\bar{\Psi}_{aniso}(\bar{I}_{4f}, \bar{I}_{4s}, \bar{I}_{8fs}) = \sum_{i=f,s} \frac{a_i}{2b_i}(\exp[b_i(\bar{I}_{4i} - 1)^2] - 1) + \frac{a_{fs}}{2b_{fs}}(\exp\left[b_{fs}(\bar{I}_{8fs})^2\right] - 1)$$

with

$$\bar{\boldsymbol{F}} = \boldsymbol{F}/J^{1/3}, \bar{\boldsymbol{C}} = \bar{\boldsymbol{F}}^T\bar{\boldsymbol{F}}, \bar{I}_1 = tr\bar{\boldsymbol{C}}, \bar{I}_{4f} = \boldsymbol{f}_0 \cdot \bar{\boldsymbol{C}} \cdot \boldsymbol{f}_0, \bar{I}_{4s} = \boldsymbol{s}_0 \cdot \bar{\boldsymbol{C}} \cdot \boldsymbol{s}_0, \bar{I}_{8fs} = \boldsymbol{f}_0 \cdot \bar{\boldsymbol{C}} \cdot \boldsymbol{s}_0$$

where $\boldsymbol{f}_0$ and $\boldsymbol{s}_0$ are fiber and sheet orientations in the original configuration. Note that if $\bar{I}_{4i} \leq 1$, the corresponding term in the above formula will be dropped since fibers buckle under compression. The parameters we used are (75) $a = 0.496\ kPa, b = 7.209, a_f = 15.193\ kPa, b_f = 20.417, a_s = 3.283\ kPa, b_s = 11.176, a_{fs} = 0.662\ kPa, b_{fs} = 9.466$, and we chose $\mu_K = 3333\ kPa$ to impose incompressibility.

To characterize the distribution of material orientations, we used the local coordinate

system with $\boldsymbol{e}_c$, $\boldsymbol{e}_l$ and $\boldsymbol{e}_n$ (**Fig. 2.3a**) as the circumferential, longitudinal and transmural normal vectors, assuming $\boldsymbol{f}_0 = \cos\alpha\,\boldsymbol{e}_c + \sin\alpha\,\boldsymbol{e}_l$ with α ramping linearly from $-\pi/2$ on endocardial surface to $\pi/2$ on epicardial surface (76), and $\boldsymbol{s}_0 = \boldsymbol{e}_n$.

For epicardium, we also used the Holzapfel-Ogden model assuming $\boldsymbol{f}_0 = \boldsymbol{e}_c$ and $\boldsymbol{s}_0 = \boldsymbol{e}_l$. We assumed that the values of a_{fs} and b_{fs} are the same as those of the porcine myocardium. By fitting the biaxial tension data of the middle lateral sample (**Fig. 2.2e**), we obtained $a = 0.496\ kPa, b = 6.82, a_f = 19.85\ kPa, b_f = 32.59, a_s = 11.26\ kPa$ and $b_s = 8.20$. The fitted stress-strain curve was compared against the experimental data in **Fig. 2.3b** which showed good agreement. The pre-strains we applied come from the middle lateral sample (**Table 2.1**) and were introduced through a pre-factor in deformation gradient $\boldsymbol{F}^{pre} = (1+\epsilon_X)\boldsymbol{e}_c\otimes\boldsymbol{e}_c + (1+\epsilon_Y)\boldsymbol{e}_l\otimes\boldsymbol{e}_l + \frac{1}{(1+\epsilon_X)(1+\epsilon_Y)}\boldsymbol{e}_n\otimes\boldsymbol{e}_n$. To compute stress, we will use $\boldsymbol{F} = \boldsymbol{F}^e\boldsymbol{F}^{pre}$, where $\boldsymbol{F}^e$ represents the deformation happening afterwards.

For boundary conditions, we prescribed $u_z = 0$ on the basal plane, and on its outer edge we prescribed $u_c = 0$ in the circumferential direction (**Fig. 2.3a**). On the endocardial surface, we applied a pressure that increases from 0 to 40 mmHg. The calculations were performed using the open-source package FEBio (77).

2.3 Results

2.3.1 Estimation of the pre-strains of the epicardial layer

The average pre-strains (ε_X and ε_Y) for each anatomical location were calculated and listed in **Table 2.1**. Several observations of **Table 2.1** are summarized as follows: (i) For nearly all the anatomical locations, the pre-strains of both the circumferential and

longitudinal directions (ε_X and ε_Y) were positive, except for ε_X in the basal anterior location (M1) and middle anterior location (B1). The positive pre-strains on the unpressurized intact heart mean that the epicardial layer was under tension and positive residual stresses existed. (ii) We found that ε_Y was much larger than ε_X in the basal anterior location (B1: ε_X = -0.30 ± 4.25%; ε_Y = 8.59 ± 3.37%) and middle anterior location (M1: ε_X = -3.51 ± 3.07%; ε_Y = 8.72 ± 6.70%). (iii) ε_X was slightly smaller than ε_Y in the basal lateral location (B2: ε_X = 4.66 ± 0.44%; ε_Y = 6.75 ± 1.85%) and middle lateral location (M2: ε_X = 7.09 ± 3.34%; ε_Y = 10.70 ± 1.30%), while both ε_X and ε_Y were large. (iv) ε_X was smaller than ε_Y in the basal posterior location (B3: ε_X = 3.01 ± 4.58%; ε_Y = 7.72 ± 4.38%) and middle posterior location (M3: ε_X = 5.50 ± 3.10%; ε_Y = 8.31 ± 4.55%). (v) For the apex location, both ε_X and ε_Y were relatively large (Apex: ε_X = 4.89 ± 1.72%; ε_Y = 8.84 ± 3.37%).

Table 2.1. Estimated pre-strains and residual stresses of the epicardial layer on the unpressurized intact heart. Pre-strains (ε_X, ε_Y) for each anatomical location were estimated by comparing stress-free marker dimensions (dissected epicardial layer) and *in situ* marker dimensions (epicardial layer on the unpressurized intact heart). Note: Stress-free marker dimensions were used as reference to calculate the pre-strains. The residual stresses ($\sigma_{X(residual)}$, $\sigma_{Y(residual)}$) for each anatomical location were predicted by ε_X and ε_Y using the adjusted biaxial stress-stretch curves (**Fig. 2.2**).

N = 5	ε_X	$\sigma_{X(residual)}$ (kPa)	ε_Y	$\sigma_{Y(residual)}$ (kPa)
Basal Anterior (B1)	-0.30 ± 4.25%	0	8.59 ±3.62%	2.39
Basal Lateral (B2)	4.66 ± 0.44%	8.95	6.75 ± 1.85%	3.05
Basal Posterior (B3)	3.01 ± 4.58%	4.68	7.72 ± 4.38%	4.48
Middle Anterior (M1)	-3.51 ± 3.07%	0	8.72 ± 6.70%	4.29
Middle Lateral (M2)	7.09 ± 3.43%	12.09	10.70 ± 1.36%	7.88
Middle Posterior (M3)	5.50 ± 3.10%	2.89	8.31 ± 4.55%	2.06
Apex	4.89 ± 1.72%	12.24	8.84 ± 3.37%	3.89

2.3.2 Estimation of the residual stresses for each anatomical location

With the biaxial stress-strain data (**Fig. 2.2**) and the pre-strain data (**Table 2.1**), we

could estimate the residual stresses for each anatomical location. In **Fig. 2.2**, red dashed lines label the circumferential residual stresses ($\sigma_{X(residual)}$) predicted by the circumferential pre-strains (ε_X), and blue dashed lines label the longitudinal residual stresses ($\sigma_{Y(residual)}$) predicted by the longitudinal pre-strains (ε_Y). The detailed numbers of $\varepsilon_X \rightarrow \sigma_{X(residual)}$ and $\varepsilon_Y \rightarrow \sigma_{Y(residual)}$ for each anatomical location are listed in **Table 2.1**.

The mapping of residual stresses on the left ventricle showed that residual stresses did exist and varied with different anatomical locations. Both the basal anterior location (B1) ($\sigma_{X(residual)}$ = 0 kPa, $\sigma_{Y(residual)}$ = 2.39 kPa) and middle anterior location (M1) ($\sigma_{X(residual)}$ = 0 kPa, $\sigma_{Y(residual)}$ = 4.29 kPa) showed a longitudinal residual stress of several kPa but predicted negligible circumferential residual stress. The basal posterior location (B3) ($\sigma_{X(residual)}$ = 4.68 kPa, $\sigma_{Y(residual)}$ = 4.48 kPa) had both the circumferential residual stress and longitudinal residual stresses of several kPa; the middle posterior location (M3) ($\sigma_{X(residual)}$ = 2.89 kPa, $\sigma_{Y(residual)}$ = 2.06 kPa) also had comparable circumferential and longitudinal residual stresses around 1 kPa. However, both the basal lateral location (B2) ($\sigma_{X(residual)}$ = 8.95 kPa, $\sigma_{Y(residual)}$ = 3.05 kPa) and middle lateral location (M2) ($\sigma_{X(residual)}$ = 12.09 kPa, $\sigma_{Y(residual)}$ = 7.88 kPa) showed a pattern of circumferential residual stress being larger (around 10 kPa) than the longitudinal residual stress. The apex region ($\sigma_{X(residual)}$ = 11.24 kPa, $\sigma_{Y(residual)}$ = 2.80 kPa) showed a pattern similar to the laterals, i.e., a large circumferential residual stress around 10 kPa, but a longitudinal residual stress of several kPa.

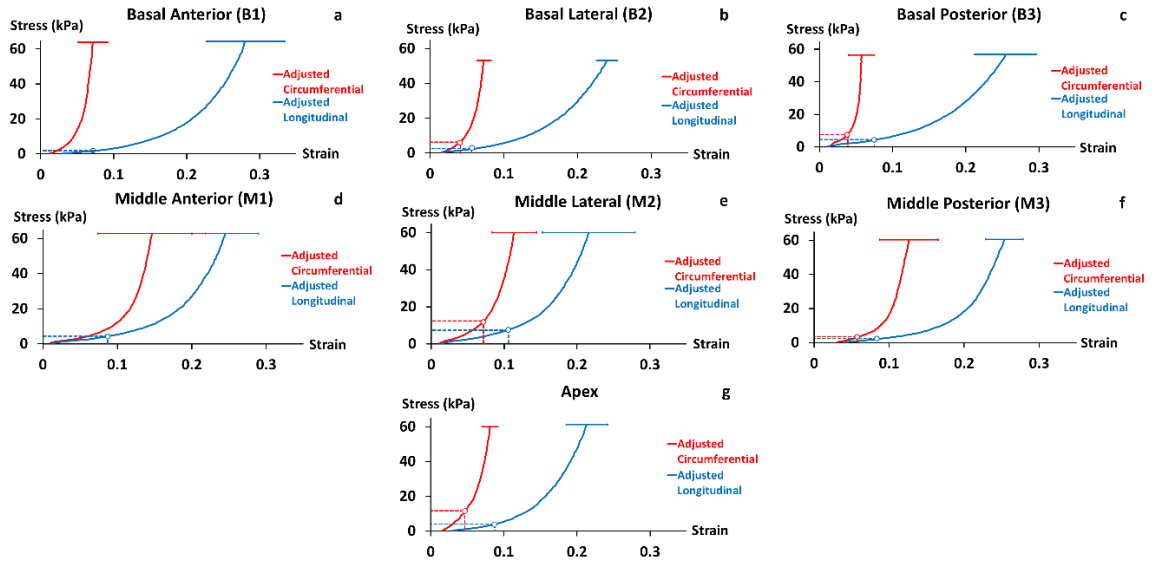

Figure 2.2. Circumferential residual stresses $\sigma_{X(residual)}$ (red dashed lines) and longitudinal residual stress $\sigma_{Y(residual)}$ (blue dashed lines) predicted by pre-strains (ε_X and ε_Y) for seven anatomical locations: (a) basal anterior, (b) basal lateral, (c) basal posterior, (d) middle anterior, (e) middle lateral, (f) middle posterior, and (g) apex locations. Adjusted biaxial stress-strain curves were used for the quantitative estimation of the regional residual stresses. Red solid curve: stress-strain curve along circumferential direction with error bar (red solid bar); blue solid curve: stress-strain curve along longitudinal direction with error bar (blue solid bar).

2.3.3 Mechanical confinement from epicardial pre-straining in FE simulation

The computed cavity volume-pressure curve is plotted in **Fig. 2.3c** and the relation between the pressure and the average myocardial first principle stress is shown in **Fig. 2.3d**, where the blue curve showed the case without epicardial pre-strain, the red curve with pre-strain, and the black curve without epicardium at all. We could notice that, with the presence of epicardial layer alone, the cavity volume barely differed from the pristine ventricle model and the average myocardial first principle stress only decreased slightly. Yet when pre-strain was applied, a non-trivial shift (up to ~4.8 mL, ~13% shift) towards smaller volume and lower average myocardial first principle stress emerged (**Fig. 2.3c,d**).

When the pressure is small, the first principle stress is actually negative as both the pre-strain and the endocardial pressure bring compression in the ventricle. And due to the stiffening of the epicardium, the relative drop in the first principle stress became more prominent as the cavity pressure increased. This showed that, by contracting against the myocardial tension, the epicardial layer provided additional confining and protection to LV wall. The contrast between the pre-strained and the un-prestrained cases also implied the majority of the confinement effect actually comes from the pre-straining instead of the epicardial layer alone.

We also noted that the end-diastolic pressure-volume curve was in good agreement with the experiment data (78) despite the simplified geometry in our model. However, in this chapter for simplicity, we didn't account for the inhomogeneous distribution of epicardial mechanical properties and pre-strain, and it may imply important local features as the epicardial curvature varies spatially as well. As a preliminary attempt to investigate how the different epicardial parameters at different locations may influence the ventricle system, we employed the pre-strain data and biaxial tension data from several other locations (**Fig. 2.2, Table 2.1**) in our homogeneous model. The results (**Fig. 2.4**) showed that, though the magnitudes varied, the parameters from different locations all had confining capability. Among all locations, the pre-strains from apex and middle lateral samples exhibited most significant confining while middle anterior and posterior samples produced medium relief in the first principle stress.

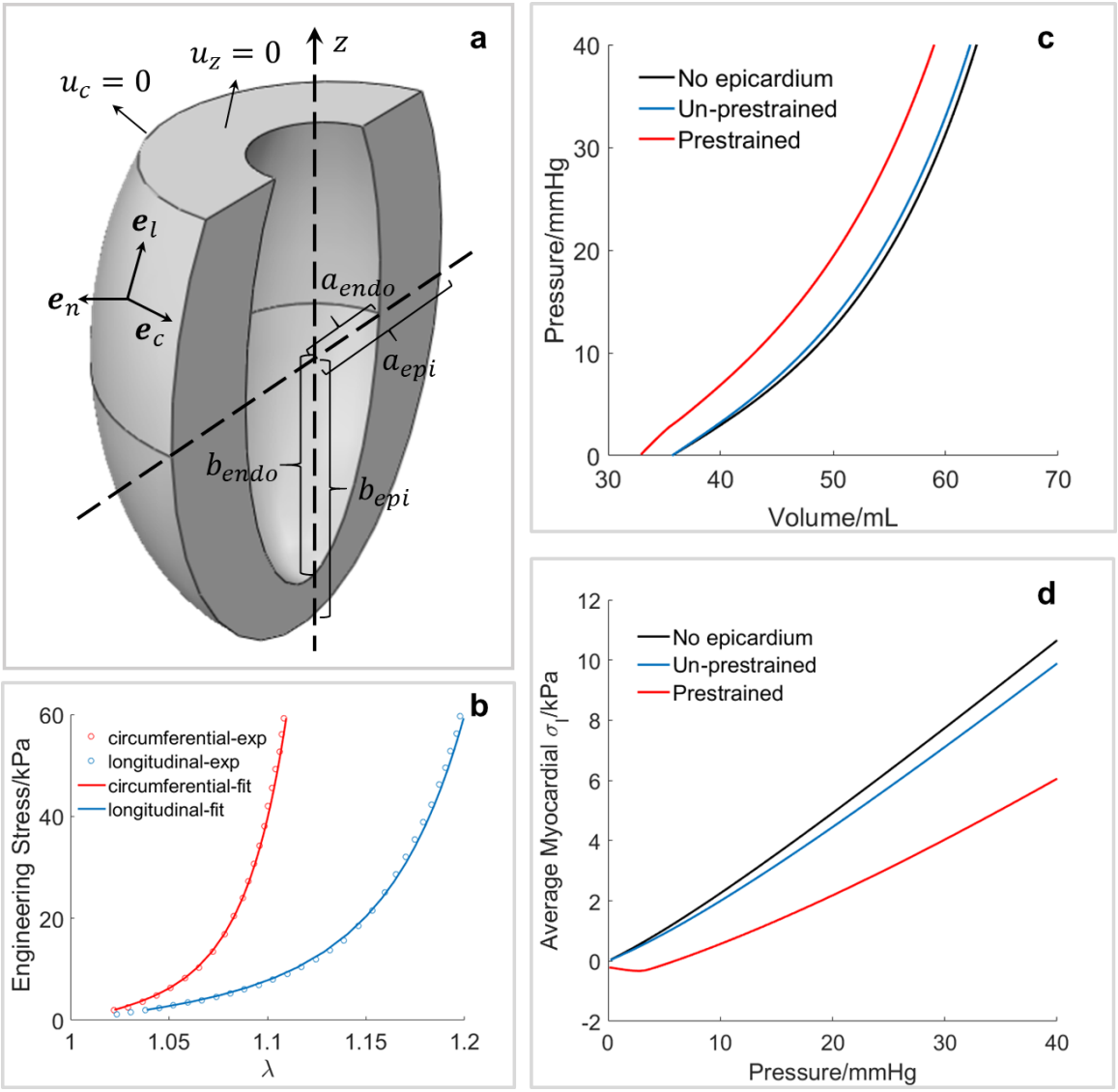

Figure 2.3. FE modelling of the effect of epicardial prestrain. (a) An illustration of the model geometry. The left ventricle is modeled as a truncated ellipsoid, characterized by 5 parameters: the semi-axes lengths of the endocardial (a_{endo}, b_{endo}) and the epicardial (a_{epi}, b_{epi}) surface, and the distance between apex and the basal plane (h). To denote the material orientations, we employ the local coordinate system whose base vectors are $\boldsymbol{e}_c$, $\boldsymbol{e}_l$ and $\boldsymbol{e}_n$, the circumferential, the longitudinal and the transmural normal vector. On the basal plane we prescribe $u_z = 0$, and on its outer edge $u_c = 0$ (in circumferential direction). (b) The fitted biaxial stress-stretch curve of the middle lateral sample. (c) The cavity volume and (d) the averaged myocardial first principle stress, plotted against the cavity pressure. The blue line shows the case without epicardial prestrain, and the red curve shows the case with epicardial prestrain, while the black line shows the case without epicardium.

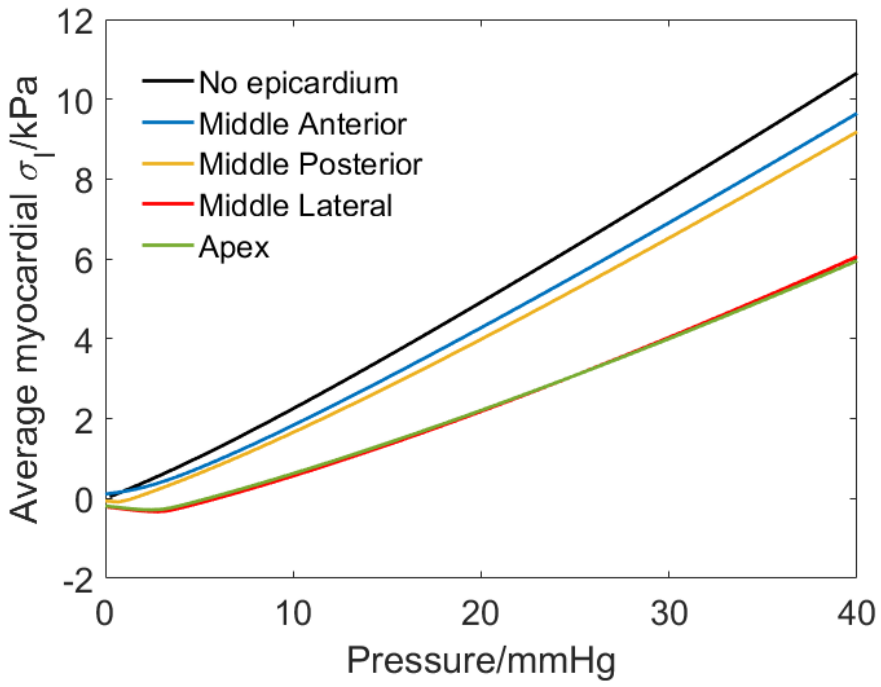

Figure 2.4. Effect of epicardial parameters from different locations. We employed the prestrain and the mechanical parameters from different locations on our homogeneous model and computed the average myocardial first principle stress as a function of the pressure. The results showed that, though the effects varied, the parameters from different locations all had confining capability.

2.4 Discussion

Considering the geometry of the intact heart, the circumferential direction of the lateral locations as well as the apex location experience large curvature. The relatively large circumferential residual stresses ($\sigma_{X(residual)}$) of the basal lateral location (B2), middle lateral location (M2), and apex might be correlated with the large curvature of the heart surface. We also noticed that the basal anterior location (B1) and middle anterior location (M1) had very low circumferential residual stresses ($\sigma_{X(residual)}$) and prestrains (**Table 2.1**). We speculate that this might also be related to their anatomical configuration, possibly a relatively flat circumferential contour.

In most FE modelling of ventricles, epicardium is usually absent and considered negligible. Yet in our model, we found that the ventricular volume would be nontrivially smaller under the same static pressure with pre-strained epicardium and lower average myocardial first principle stress was observed due to the epicardial pre-straining. Usually, parietal pericardium sac is associated with an important function of limiting ventricular filling and preventing high diastolic pressure (57), and our results indicate that such capability can also come from epicardial pre-straining. If pre-strain is absent, the confining capability of the epicardium to reduce the cavity volume and average myocardial first principle stress would be significantly impaired even if the epicardium itself is intact. Moreover, how the epicardial pre-straining would participate in the cardiac cycle, affect ventricular filling and protect the myocardium, especially during the early ejection phase, remains an open but interesting question. Additionally, how the pre-straining can influence the long-term behaviors of the ventricle like growth and remodeling, especially under pathological conditions will also lead to important insight into the cardiac system. These could be some important aspects in cardiac biomechanics/physiology to be addressed in the future studies and modelling.

2.5 Conclusion

We developed a method to quantitatively assess the epicardial residual stresses of the left ventricle by combining pre-strain measurement and biaxial mechanical testing. For the first time, we were able to quantitatively estimate (i) the epicardial pre-strains along the circumferential direction (ε_X) and longitudinal direction (ε_Y), and (ii) the circumferential residual stress ($\sigma_{X(residual)}$) and the longitudinal residual stress ($\sigma_{Y(residual)}$) of the left ventricular epicardial layer. We also noticed certain correlation between our pre-

strain/residual stress results and curling angle measurements. For instance, we found that the basal lateral location (B2) had relatively large circumferential pre-strain (ε_X) and residual stresses ($\sigma_{X(residual)}$) when compared to the basal anterior (B1) and basal posterior (B3) location, and the middle lateral location (M2) also had relatively large circumferential pre-strain (ε_X) and residual stresses ($\sigma_{X(residual)}$) when compared to the middle anterior (M1) and middle posterior (M3) location (**Table 2.1**). We know that the circumferential direction of the lateral location experiences very large curvature. The relatively large $\sigma_{X(residual)}$ of the basal lateral location (B2) and middle lateral (M2) might be correlated with the large curvature of the heart surface at those locations.

The existence of residual stresses and pre-straining has its physiological relevance for organ/tissue functionality. To investigate the potential mechanical effect of epicardial pre-straining, a FE model was constructed, and we found that the pre-strained epicardial layer can provide additional confining to the ventricle and reduce its cavity volume. We further showed that, such resistance mainly comes from the pre-straining instead of the epicardium alone.

In short, the epicardial layer, with its rich elastin content, acts like a pre-strained "balloon" wrapping around the heart. From a biomechanical perspective, the epicardial pre-strained confinement (residual stress) provides an additional resistance mechanism during LV diastolic expansion, and might further assist with the contraction of the LV by epicardial recoiling. Our future studies will focus on the understanding of how the epicardial pre-straining facilitates cardiac biomechanical functions, and how heart diseases, such as MI, could possibly alter the pre-strained confinement (residual stress) of the epicardial layer and hence weaken the protection in ventricular diastolic expansion and

efficiency of ventricular contractions. Future therapeutic efforts for MI might target the maintenance or recreation of this ventricle confinement interface. For example, passive prosthetic wrap devices and cardiac patch/meshing techniques might benefit from applying a pre-strained confinement. In the next chapter, we will present a viscoelastic epicardial patch with specifically designed viscoelastic traits to provide the optimal mechanical support the post-infarct myocardium.

Chapter 3

Mechanical interaction between infarcted ventricle and viscoelastic gel

3.1 Introduction

Ischemic heart disease remains the most fatal cause of death worldwide. Cardiac patches, made from biomaterials or biological substances and sometimes in combination with cells or drugs, offer a potential treatment for severe myocardial infarction (MI) and subsequent heart failure (79-84). The biomaterial-based acellular epicardial patch is designed to passively restrain the infarct area of the myocardium following MI, which functions to reduce myocardium wall stress and subsequently prevent left ventricular (LV) dilation and remodeling. Although the therapeutic effect of various acellular epicardial patches on MI have been reported for over the years (83, 85-95) and the benefits of mechanical support from such patches to the myocardial wall have been established (79, 85, 91-95), the optimal patch design is still unknown due to the lack of understanding of the mechanisms involved in limiting LV remodeling and restoring cardiac function following MI (95, 96). In fact, it is not even clear if the appropriate patch stiffness exists. The patches reported in the literature to be effective in reducing LV dilation or preserving cardiac function to different extent have stiffness values varying from tens of kilopascals to tens of megapascals(83, 86, 87, 89, 90, 97-99). This ambiguity calls for a more rational design of the acellular epicardial patch that could maximize the mechanical benefit and subsequent therapeutic efficacy for the infarcted myocardium. Here, we introduce a

simulation-guided strategy to design and develop a type of self-adaptive epicardial patch that accommodates the time-varying deformation of the beating heart and maintains a reliable efficacy in restraining ventricular dilatation and preventing adverse LV remodeling and cardiac failure after MI. This chapter is finished in collaboration with Prof. Lei Yang and Prof. Ning Sun and published in Ref. {Lin, 2019 #282}.

3.2 Model and methods

3.2.1. General setup for finite element (FE) simulation

We used a truncated ellipsoid as a generic geometrical representation of the human left ventricle, with semi-axes length and height taken from Ref (100). The semi-axes lengths are 49.25 mm, 26.85 mm for the epicardial surface, and 42.75 mm, 19.4 mm for the endocardial surface. The height between the basal plane and the apex point is 63.58 mm. We assumed the material orientations of the myocardium to ramp linearly in the transmural direction, the fiber angle rotating from $\pi/3$ on endocardial surface to $-\pi/3$ on the epicardial surface, and the sheet angle from $\pi/4$ to $-\pi/4$ (101). On the basal plane, we prescribed zero vertical displacement and along its edge we fixed the circumferential displacement (74). The degree of myocardial infarction was characterized by an index M which ranges from 0 in the healthy zone to 1 in the infarction zone and varies continuously in a transition zone in between. The stiffness of the myocardium was assumed to change linearly with M (102), and be twice of the normal value in the infarction zone, where the wall thickness and the active contraction were taken as only half of the normal value, corresponding to a mild degree of myocardium remodeling under infarction (Fig 3.1a). A tied interface between the ventricle and patch ensured the displacement continuity.

We performed two types of simulations. The first was a cyclic loading simulation

aimed to characterize the stroke volume of the ventricle under the effect of infarction and patch. On the endocardial surface, a time-varying pressure $p(t)$ was applied. The simulation included several stages: (i) the initialization stage, where p increased to the end-diastolic pressure (EDP) while the patch deformed plastically. At the end of this stage, the deformation gradient within the patch was recorded as $\mathbf{F}^p$, and then based on this configuration, a circumferential pre-stretch $\mathbf{F}^{\mathrm{pre}} = \lambda^{\mathrm{pre}}\mathbf{e}_c \otimes \mathbf{e}_c + (\lambda^{\mathrm{pre}})^{-1/2}(\mathbf{I} - \mathbf{e}_{\mathrm{c}} \otimes \mathbf{e}_{\mathrm{c}})$ was applied to the patch ($\mathbf{e}_{\mathrm{c}}$ is the unit vector in the circumferential direction). Starting from this point, the total deformation gradient of the patch can be written as $\mathbf{F} = \mathbf{F}^{\mathrm{e}}\mathbf{F}^{\mathrm{pre}}\mathbf{F}^{\mathrm{p}}$ where $\mathbf{F}^e$ denotes the subsequent elastic deformation and only $\mathbf{F}^{\mathrm{e}}\mathbf{F}^{\mathrm{pre}}$ contributes to the stress generation; (ii) the isovolumetric contraction stage, where the active contraction began while the ventricular cavity volume was fixed through a penalty method; (iii) the ejection phase after p reached 80 mmHg (103), where a two-element Windkessel model was adopted to simulate the hemodynamics:

$$C\frac{\mathrm{d}p}{\mathrm{d}t} + \frac{p}{R} = -\frac{\mathrm{d}V}{\mathrm{d}t}$$

(V denoting the volume of the cavity) which has an analogy with the electrical circuit system; (iv) the isovolumetric relaxation stage after the blood flow became reversed ($\mathrm{d}V/\mathrm{d}t \geq 0$), where the cavity volume again was fixed; (v) the filling stage after p reached 4.5 mmHg (103), the pressure was increased back to the EDP, which was chosen to be 8 mmHg for a healthy ventricle (102) and 15 mmHg in the case of infarction (104). For all cases we computed 3 cycles which was sufficient for convergence and then recorded the stroke volume (SV) value.

The second type of simulation was a ventricular remodeling test that aimed to study the ventricular dilatation under the infarction conditions and the patch effect. The

simulation consisted of two stages: (i) the initialization stage which was identical to the cyclic loading simulation; (ii) the remodeling stage where the myocardial lengthening started to develop under constant endocardial pressure.

3.2.2. Constitutive models and parameters for finite element simulations

For both cyclic loading and remodeling simulations, again we modeled the passive elasticity of the myocardium through the Holzapfel-Ogden model (6, 74) with the strain energy density function taking the following form:

$$\Psi = U(J) + \bar{\Psi}_{\text{iso}}(\bar{I}_1) + \bar{\Psi}_{\text{aniso}}(\bar{I}_{4f}, \bar{I}_{4s}, \bar{I}_{8fs})$$

$$U(J) = \frac{\mu_K}{2}(\ln J)^2$$

$$\bar{\Psi}_{\text{iso}}(\bar{I}_1) = \frac{a}{2b}(\exp[b(\bar{I}_1 - 3)] - 1)$$

$$\bar{\Psi}_{\text{aniso}}(\bar{I}_{4f}, \bar{I}_{4s}, \bar{I}_{8fs}) = \sum_{i=f,s} \frac{a_i}{2b_i}(\exp[b_i(\bar{I}_{4i} - 1)^2] - 1) + \frac{a_{fs}}{2b_{fs}}\left(\exp[b_{fs}(\bar{I}_{8fs})^2] - 1\right)$$

where, based on the deformation gradient $\mathbf{F} = \frac{\partial \mathbf{x}}{\partial \mathbf{X}}$ with determinant J, we have defined $\bar{\mathbf{F}} = \mathbf{F}/J^{1/3}$, $\bar{\mathbf{C}} = \bar{\mathbf{F}}^T\bar{\mathbf{F}}$, $\bar{I}_1 = tr(\bar{\mathbf{C}})$, $\bar{I}_{4f} = \mathbf{f}_0 \cdot \bar{\mathbf{C}} \cdot \mathbf{f}_0$, $\bar{I}_{4s} = \mathbf{s}_0 \cdot \bar{\mathbf{C}} \cdot \mathbf{s}_0$, $\bar{I}_{8fs} = \mathbf{f}_0 \cdot \bar{\mathbf{C}} \cdot \mathbf{s}_0$, where $\mathbf{f}_0$ and $\mathbf{s}_0$ are the initial fiber and sheet (cross-fiber) orientations. The parameters used were taken from Ref (102) as: $a = 0.24\,kPa$, $b = 5.08$, $a_f = 1.46\,kPa$, $b_f = 4.15$, $a_s =$ 0.87 kPa, $b_s = 1.6$, $a_{fs} = 0.3$ kPa, $b_{fs} = 1.3$.

For the active contraction during cyclic loading, we adopted the time-varying elastance model (105, 106): $T^{active} = \frac{T_{\max}}{2}\frac{Ca_0^2}{Ca_0^2 + ECa_{50}^2}(1 - \cos\omega)$. In this model, $T_{\max}$ is the isometric tension developed under the maximum sarcomere length; $ECa_{50} = (Ca_0)_{\max}/\sqrt{\exp[B(l - l_0)]}$ accounts for the cellular sensitivity for calcium ion, which depends on the intracellular calcium concentration $(Ca_0)_{\max}$, the current sarcomere length $l = l_r\lambda_f$

and its value without activation l_0 (B is a constant; l_r is the unloaded sarcomere length and λ_f is the stretch ratio in the fiber direction); ω is a time factor defined as

$$\omega = \begin{cases} \pi \dfrac{t}{t_0}, & \text{when } 0 \le t \le t_0 \\ \pi \dfrac{t - t_0 + t_{\mathrm{r}}}{t_{\mathrm{r}}}, & \text{when } t_0 \le t \le t_0 + t_{\mathrm{r}} \\ 0, & \text{when } t_0 + t_{\mathrm{r}} \le t \end{cases}$$

with t_0 being the maximum tension development time, $t_r = ml + b$ a relaxation time that depends on the sarcomere length through constants m and b. The parameters used here are $Ca_0 = 4.35\ \mu\text{mol/L}$, $Ca_0 = 4.35\ \mu\text{mol/L}$, $(Ca_0)_{\max} = 4.35\ \mu\text{mol/L}$, $B = 4.75\ \mu m^{-1}$, $l_0 = 1.58\ \mu m$, $m = 1.0489\ s \cdot \mu m^{-1}$, $b = -1.429\ s$; l_r was set to vary linearly from $1.78\ \mu m$ on endocardium to $1.91\ \mu m$ on epicardium(107, 108); $T_{max} = 120\ kPa$ was obtained by fitting the peak pressure and the ejection fraction in Ref(103). The active stress $\boldsymbol{\sigma}^{\text{active}} = J^{-1} T^{active} \mathbf{f} \otimes \mathbf{f} / |\mathbf{f}|^2$ is added to the stress tensor.

In the left ventricular (LV) remodeling test, we adopted a mechanically induced lengthening law (109, 110); the total deformation gradient was decomposed as $\mathbf{F} = \mathbf{F}^e \mathbf{F}^{\mathrm{g}}$ where the remodeling part, which does not contribute to stress, takes the form $\mathbf{F}^{\mathrm{g}} = \mathbf{I} + (\lambda^g - 1)\mathbf{f}_0 \otimes \mathbf{f}_0$. The lengthening ratio evolves as (109)

$$\dot{\lambda}^{\mathrm{g}} = \begin{cases} \dfrac{1}{\tau^{\mathrm{g}}} \left(\dfrac{\lambda^{\max} - \lambda^{\mathrm{cr}}}{\lambda^{\max} - 1} \right)^{\gamma} \left(\dfrac{\lambda_f}{\lambda^{\mathrm{g}}} - \lambda^{\mathrm{cr}} \right), & \text{if } \dfrac{\lambda_f}{\lambda^{\mathrm{g}}} - \lambda^{\mathrm{cr}} > 0 \\ 0, & \text{if } \dfrac{\lambda_f}{\lambda^{\mathrm{g}}} - \lambda^{\mathrm{cr}} \le 0 \end{cases}$$

In our model, $\gamma = 1$, $\lambda^{\max} = 1.5$ and we took λ^{cr} to be the stretch ratio along the fiber direction at the end-diastole (EDP=8 mmHg) in the healthy model. The remodeling simulations were carried out for a time period ($10\ \tau^g$) which could represent physical time on the order of months to years (111).

The patch, on the other hand, was first modeled as an incompressible neo-Hookean solid with shear modulus G. To model the pre-stretch, we multiply the deformation by $\mathbf{F}^{\mathrm{pre}} = \lambda^{pre}\mathbf{e}_c \otimes \mathbf{e}_c + (\lambda^{\mathrm{pre}})^{-\frac{1}{2}}(\mathbf{I} - \mathbf{e}_{\mathrm{c}} \otimes \mathbf{e}_{\mathrm{c}})$, so the total stress-inducing deformation is $\mathbf{F}^{\mathrm{e}}\mathbf{F}^{\mathrm{pre}}$, where $\mathbf{F}^{\mathrm{e}}$ is the elastic deformation after the pre-stretch. To investigate the potential effect of fluidity and viscosity, we also employed the Maxwell fluid model: $\mathbf{S} = \int_{-\infty}^{\infty} \exp[-(t-s)/\tau] \frac{d\mathbf{S}^e}{ds} ds$ (112), τ being the characteristic time for stress relaxation and $d\mathbf{S}^e$ the incremental first Piola-Kirchhoff stress under the neo-Hookean model with shear modulus G. Note such model, under small deformation, gives a shear storage modulus of $G'(\omega) = \frac{\tau^2\omega^2}{\tau^2\omega^2+1} G$ and loss modulus of $G''(\omega) = \frac{\tau\omega}{\tau^2\omega^2+1} G$. We focused on the moduli at the working frequency of $f = 1\ s^{-1}$, which is a characteristic frequency for human heart. Here we simulated up to 6 cycles for all cases and recorded stroke volume. Please note in reality if the patch exhibits stress relaxation with a power-law instead of exponential decay, the equilibration process will be much longer. All simulations were carried out using the open-source package FEBio (77).

3.2.3. The hemodynamics simulation

To fit the experimental hemodynamics we chose the parameters C and R in the Windkessel model and the T_{max} in the active contraction by matching the peak pressure and the ejection fraction in Ref (103). Some typical results of the P-V loop were shown in **Fig. 3.2a**. Here the circles were taken from Ref (103) with volume normalized by its EDV, while the volume in the simulation curves were normalized by the healthy model simulation (EDP = 8 mmHg). It can be seen that both peak pressure and ejection fraction in our healthy model agreed well with the experiment. The volume-averaged stretch ratio

in the fiber direction λ_f in a healthy model during a loop was plotted in **Fig. 3.2b**, which varied between 0.92 and 1.18.

3.3 Results and discussion

3.3.1 Finite-element modeling of elastic epicardial patch under pre-stretch

Ideally, the patch should balance between restraining the normal cardiac loop and providing protection against the adverse dilatation cascade. When seeking materials for mechanical support in biological systems, we focused on the compatibility of static elastic properties such as stiffness(113), which is insufficient in the cardiovascular system. Due to the time-varying geometry of the system, applying the patch at different moments can set different reference points for deformation, thus introducing different amounts of pre-deformation into the patch, with a non-trivial mechanical effect. Along this line, we constructed a finite element ventricle infarction model with a patch with pre-deformation, characterized by a pre-stretch factor λ^{pre} (a sketch of the model is shown in **Fig. 3.1a**, and the detailed setup is described in the Section 3.2.1), with which simulations of both cardiac loop and dilatation remodeling were performed.

First, we studied how the elastic patch with different stiffness and pre-stretch characteristics could influence the cardiac cycle. **Fig. 3.2a** shows some typical simulated Pressure-Volume (P-V) loops. The general influence of patch elasticity on stroke volume (SV) is summarized in **Fig. 3.1b**. Apart from the fact that higher patch stiffness decreases the SV, a major observation was the strong effect of the pre-stretch, especially at the high stiffness regime where pre-stretch can severely deform the ventricle and restrain the filling. In comparison, the pre-stretched patch did not introduce a significant promotion in the contraction, or a significantly lower end-systolic volume (**Fig. 3.2a**). This can be a major

drawback for high stiffness as pre-stretch is usually very difficult to avoid.

We also conducted a remodeling simulation to investigate the ventricular dilatation with the elastic patch, where the change in end-diastole ventricular cavity volume was computed (**Fig. 3.1c**). Some distributions of the lengthening factor λ^g are shown in **Fig. 3.1d**. As can be intuitively expected, higher patch stiffness and pre-stretch brought better confinement against the lengthening and dilatation. However, it should be noted that, for the case without pre-stretch ($\lambda^{pre} = 1$), at a high stiffness regime the confinement reached a plateau, indicating saturation of the stiffness. In comparison, in the presence of pre-stretch, the confinement was substantially enhanced.

3.3.2 Alternative design with fluid-like material near gel point

Combining the cyclic loading and LV remodeling simulations, we noticed that a stiff elastic patch appears not ideal due to the risk of over-reducing the SV whenever a pre-stretch exists (for example, when the patch is applied near end-systole or when the ventricle grows or remodels). In comparison, a patch with $G_{\mathrm{patch}}h_{\mathrm{patch}}/G_{\mathrm{myo}}h_{\mathrm{myo}}$ (G denotes the shear modulus and h the thickness, the subscript *patch* denotes the patch, and *myo* the myocardium) in the range of 10^{-2} to 10^{-1}, together with about 10%–20% (**Fig. 3.1b, c**) pre-stretch could both resist against dilatation and stay robust on SV around pre-stretch perturbations. However, tuning the pre-stretch becomes another challenge. Since the ordinary magnitude of myocardial strain during a heartbeat is also approximately ±10%–20% (**Fig. 3.2b**), one solution was to replace the solid elastic patch with a fluid-like material with the storage modulus being minimal at zero frequency (static modulus) yet finite at working frequency. This way, the patch generates stress only according to the dynamic variation of strain, instead of the absolute deformation, and effectively we could obtain a

pre-stretch near the desired value. Because viscoelasticity is usually accompanied by viscous dissipation, we used the Maxwell fluid model on the patch with $\lambda^{pre} = 1.5$ and computed the associated SV, as presented in **Fig. 3.1e**. It was found that, at working frequency, the SV dropped promptly as the order of magnitude of $G"/G'$ approached 10^1, whereas, near 10^{-1}, the ventricle had a longer exposure to the lowered SV under initial pre-stretch during the equilibration process, from which we concluded that the patch would be most adaptive to cardiac functioning as $G"/G'$ stayed close to 1. Although here we only considered the working frequency $f = 1s^{-1}$, to accommodate the varied biological heartbeat frequencies under different physiological conditions, it is desirable to have $G"/G' \sim 1$ for a wider frequency range, which can be satisfied at the so-called gel point (114, 115). That is, a material near the gel point can not only provide necessary fluidity but also avoid excessive dissipation. With this design (i.e., $G_{\text{patch}}h_{\text{patch}}/G_{\text{myo}}h_{\text{myo}} \sim 10^{-2} \sim 10^{-1}$ and $G"/G' \sim 1$), the patch is expected to balance between restraining the dilatation and maintaining the normal cardiac function. Moreover, since both $G_{\text{patch}}h_{\text{patch}}/G_{\text{myo}}h_{\text{myo}}$ and $G"/G'$ are non-dimensional parameters, the above conclusions regarding their effects should remain independent of the size or temporal scale of the ventricle system.

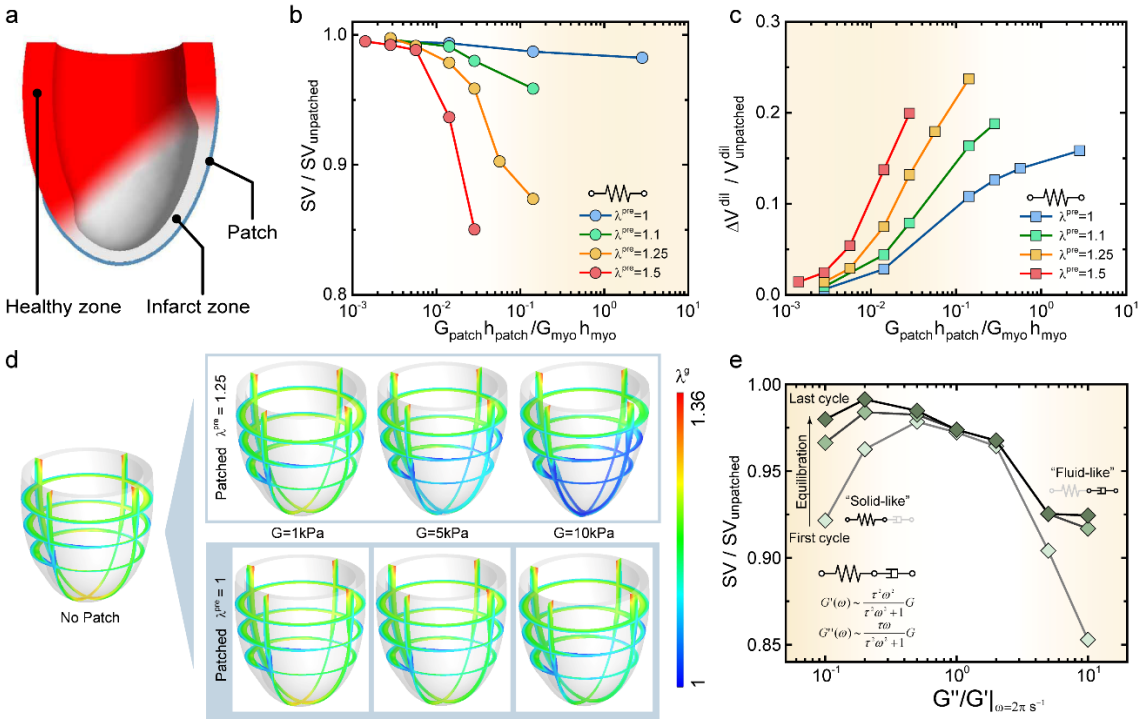

Figure 3.1. Finite element simulation model for the epicardial patch. (a) An illustration of the model geometry. Infarct zone is located around the apex and part of the ventricle wall, with half of the contractility and thickness yet double the stiffness of the healthy zone. (b) The relation between SV (15 mmHg EDP) and patch shear modulus at different pre-stretch levels, with SV normalized by the unpatched value, and modulus normalized by the end-diastole myocardium shear modulus (44 kPa in our model) and the patch-myocardium thickness ratio ($h_{\text{patch}}/h_{\text{myo}}$~$1/8$). (c) The relation between the dilated cavity volume V^{dil} and patch shear modulus at different pre-stretch levels; $\Delta V^{\text{dil}} = V^{\text{dil}}_{\text{unpatched}} - V^{\text{dil}}$ denotes the difference in dilated cavity volume with and without patch. (d), Distribution of the lengthening factor after dilatation under various values of patch stiffness and pre-stretch, where $\lambda^{\text{g}} = 1$ corresponds to no local lengthening. The patch is not shown in the figures for clarity. (e) Effect of viscous dissipation with a Maxwell viscoelastic patch with $\lambda^{\text{pre}} = 1.5$ initially. Horizontal axis is the ratio between loss and storage modulus at the working frequency of $f = 1\text{s}^{-1}$ with $G'(2\pi f) = 10\text{kPa}$, whereas vertical axis is the SV ratio to the unpatched case. Three curves from the bottom to top show SV from three different cycles during the equilibration. The bottom curve is the computed first cycle, the middle curve an intermediate cycle and the top curve the converged cycle.

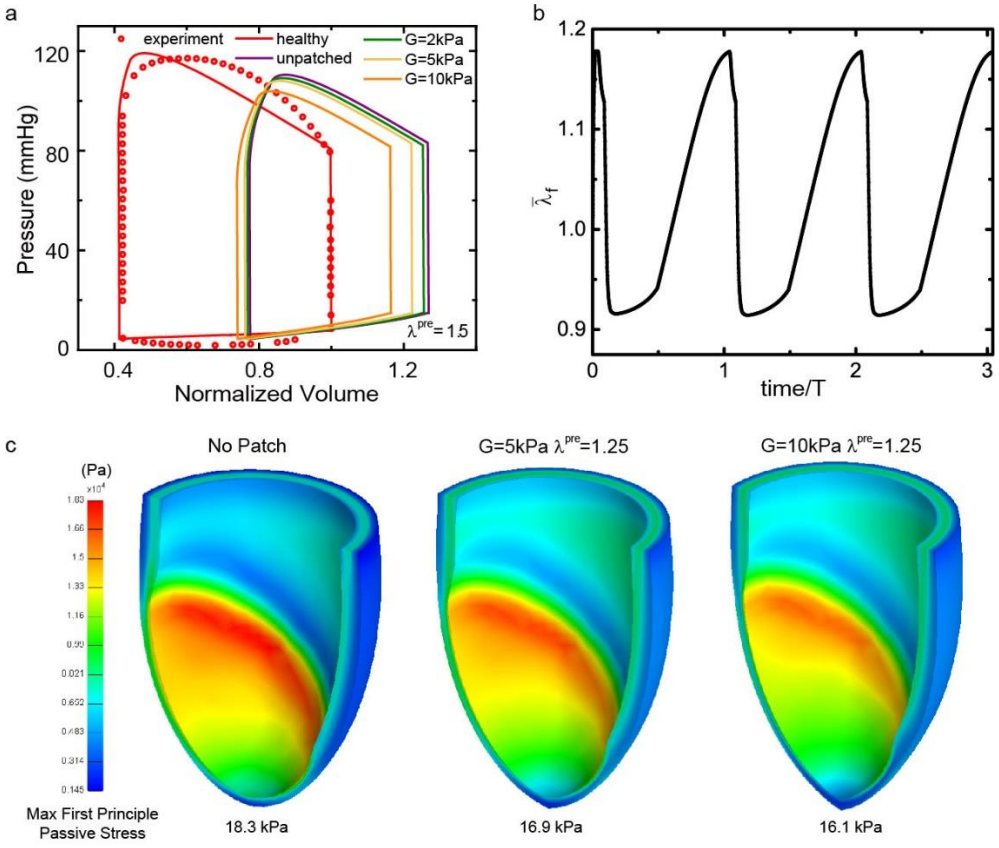

Figure 3.2. Typical simulated human cardiac cycles. (a), The P-V loop from experiment (103), healthy model, infarct model without and with patch ($\lambda^{\mathrm{pre}} = 1.5$). Volumes are normalized by that of the healthy model, which has a lower end-diastolic pressure (8 mmHg) than infarct model (15 mmHg). (b), Time variation curve of the volume-averaged stretch ratio in the fiber direction of myocardium. (c), Distribution of first principle passive stress at end diastole for three different cases. Numbers on the bottom: the maximal value of the first principle passive stress in the system.

3.3.3 Developing a simulation-guided gel-point adhesive patch

To validate the above simulation-guided design, we developed a gel-point adhesive patch possessing the viscoelastic traits as suggested by the theoretical predictions (GPAP, **Fig. 3.3a, b**). In essence, GPAP is an ionically cross-linked transparent starch hydrogel whose dynamic moduli (**Fig. 3.3c**) indeed fit well with the power law relations given by the gel equation of crosslinking polymer at the gel point (114, 115). GPAP has a markedly

higher stretchability (~3500 % measured at a strain rate of 0.143 s^{-1}) than most conventional or engineered hydrogels(116) and its stretching behavior under a constant strain rate also fits well with the neo-Hookean model (**Fig. 3.3b**). We have verified that GPAP exhibits almost identical loss and storage moduli ($G"/G' = 0.95{\sim}1.15$, **Fig. 3.3c**) over a wide range of temperature (20–60 °C), humidity (40%–80% RH), and shear strain (1%–100%) and frequency (0.1–10 Hz). GPAP is also injectable, and its moduli can be adjusted by slightly tuning the starch concentration (e.g., SGP1 shown below), enabling more versatility for future clinical uses such as minimally invasive surgery and personalized treatment. According to the theoretical design, the GPAP was prepared to possess storage moduli of ~3 kPa and ~1 kPa at the oscillation frequencies close to the rat (~6 Hz) and human (~1.25 Hz) heart rates, respectively, within the body temperature range (37–40 °C) (**Fig. 3.3c**).

Also, the adhesiveness of GPAP is higher than that of commercially available collagen and similar to that of fibrin glue, as shown by the strength and interfacial toughness results from adhesion tests (**Fig. 3.3d, e**). In contrast, although the commercial cyanoacrylate glue has a much higher adhesiveness than GPAP and other tissue glues, its high stiffness is not compliant enough to accommodate the cyclic deformation of the beating heat, causing 100% rate of death in rats after 2 days of implantation.

We further conducted a cyclic tensile test on the GPAP at a frequency of 1.25 Hz and strain of 25% to mimic the dynamic deformation of the human heartbeat. GPAP is mechanically stable under cyclic loading as its neo-Hookean tensile behavior remains identical after 2000 cycles (**Fig. 3.3b**). More importantly, the stress converges to a steady state within 5000 cycles following a rapid decay of stress within the first 100 cycles (**Fig. 3.3f**), and the steady state stress appeared to be independent of the pre-stretch. This

mechanical behavior is in agreement with the aforementioned simulation-based design, and such unique self-stabilization ability, attributed to the gel-point characteristic of the material, indicates that GPAP has a self-adaptive stiffness that yields appropriate stress to the myocardium in response to the cyclic deformation magnitude. The self-adaptive capability is key to circumvent the reliability issue associated with the magnitude of pre-stretch during patch deployment, which is difficult to optimize and remains an challenge for existing ventricular restraint devices (95, 117, 118), leading to a class of patches that are mechanically safe to be applied on the myocardium regardless of the magnitude of the pre-stretch and diastole or systole phases.

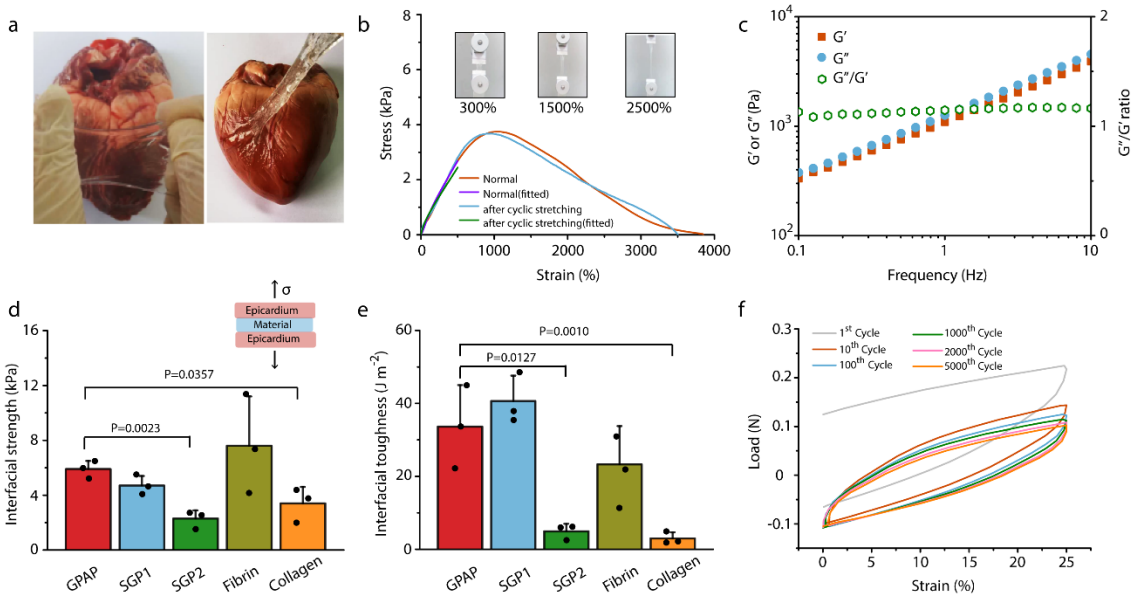

Figure 3.3. Gel point adhesive patch for MI treatment. **(**a), A stretched GPAP film (left) adhering firmly on the pig epicardium (right). (b), Stress-strain curves of GPAP under strain rate $\dot{\epsilon} = 0.143s^{-1}$ before (blue) and after (red) cyclic stretching and are fitted with neo-Hookean model to 500% strain. Inset photos are GPAP stretched at different ratios. (c), Dependence of G', $G"$, and their ratios of GPAP upon frequency of oscillation. (d), The material/epicardium interfacial strength. The inset is a diagram of the adhesion test. e, The material/epicardium interfacial toughness. (f), Load-strain curves of GPAP (pre-strain of 50%) at different stretching cycles up to 5000 cycles. For (d) and (e), original data with their

means and standard deviations are presented. n = 3 distinct samples for all groups. Two-tailed unpaired Student's t-test for comparison between two groups.

3.3.4 GPAP reverses LV remodeling after acute MI in rat

We next patched the GPAP on the hearts of acute or sub-acute MI rat models established by left anterior descending coronary artery (LAD) ligation. Cardiac function and structure were assessed by echocardiography and histology at different time points after MI (**Fig. 3.4a**). In our experiment, the selection of $G_{\mathrm{patch}}h_{\mathrm{patch}}/G_{\mathrm{myo}}h_{\mathrm{myo}}$~$8.8 \times 10^{-2}$ (rat myocardium stiffness was estimated from Ref.(119) and $h_{\mathrm{patch}}/h_{\mathrm{myo}}$ was measured to be around 1/8) is in the expected optimal range from our simulation and this parameter $G_{\mathrm{patch}}h_{\mathrm{patch}}$ was demonstrated to remain unchanged for at least 8 weeks. In order to validate the therapeutic effect of the simulation-optimized GPAP and elucidate the underlying mechanisms, two biocompatible starch gel patches (SGP) with almost identical composition but differed mechanical properties were also tested. SGP1 had similar gel-point characteristics as GPAP while SGP2 was more solid-like (i.e., $G' > G"$). Since both SGPs were much stiffer than GPAP (storage moduli SGP2>>SGP1>GPAP), the parameter $G_{\mathrm{patch}}h_{\mathrm{patch}}/G_{\mathrm{myo}}h_{\mathrm{myo}}$ for SGP1(~0.58) and SGP2 (~4.23) did not fall in the simulation-suggested optimal range.

Among the 4-week echocardiographic results of all groups, the MI+GPAP group showed the smallest values of left ventricular interior diameter at diastole (LVIDd) and systole (LVIDs) (**Fig. 3.4b**), indicating less dilatation of the heart and cardiac remodeling after the mechanical treatment. Left ventricular ejection fraction (LVEF) and fractional shortening (LVFS) were among the highest compared to those of the MI only and two SGP groups at week 4 (**Fig. 3.4b**), indicating a better improvement of left ventricular heart

function after patching the GPAP on the infarcted heart in acute MI.

Histological examinations by hematoxylin & eosin (HE) and trichrome staining 4 weeks after MI showed that the left ventricular wall was thicker in the GPAP group and preserved substantially more myocardia than those in the MI and two SGP groups (**Fig. 3.4c,d**). Fibrosis was also significantly alleviated in the MI+GPAP group (**Fig. 3.4c**), suggesting that the events of cardiomyocyte death and subsequent replacement with fibrotic tissues in the damaged area were greatly reduced after immediate application of GPAP after MI. Moreover, morphological evaluation demonstrated that the left ventricular wall thickness increased (**Fig. 3.4d**) and infarction size (IS) decreased (**Fig. 3.4e**) significantly in the MI+GPAP group compared to those in the MI and two SGP groups. These results demonstrated that the unique mechanical properties of GPAP alone, without support from any additional biological agents or cells, had a substantial reversing effect on the pathological cardiac remodeling after acute MI. Micro-CT evaluation showed that GPAP was stably patched on the epicardium at 3 months after MI (**Fig. 3.4a**). Further, GPAP application reduced myocyte hypertrophy at the border zone 4 weeks after MI (**Fig. 3.5a**). Hemodynamic measurements of MI hearts with and without patched GPAP at 4 weeks showed that GPAP significantly enhanced left ventricular pressure and the maximum value of dP/dt (**Fig. 3.5b**), indicating markedly improved left ventricular systolic and diastolic function when GPAP was applied after MI. Simulation results of local change in LV wall stress also revealed that the passive stress at end diastole near the border zone of MI had a non-trivial drop when the patch was applied (**Fig. 3.2c**). To our knowledge, in terms of therapeutic efficacy defined by the overall changes in LVEF, LVFS, and IS before and after epicardial patch treatment for MI in the rat model, the present GPAP surpasses

many other biomaterial-based acellular patches developed so far (86, 88, 90, 120-123) as well as extracellular matrix (ECM)-based acellular patches (124, 125), and even some cell-loaded and/or therapeutic agent-loaded patches.

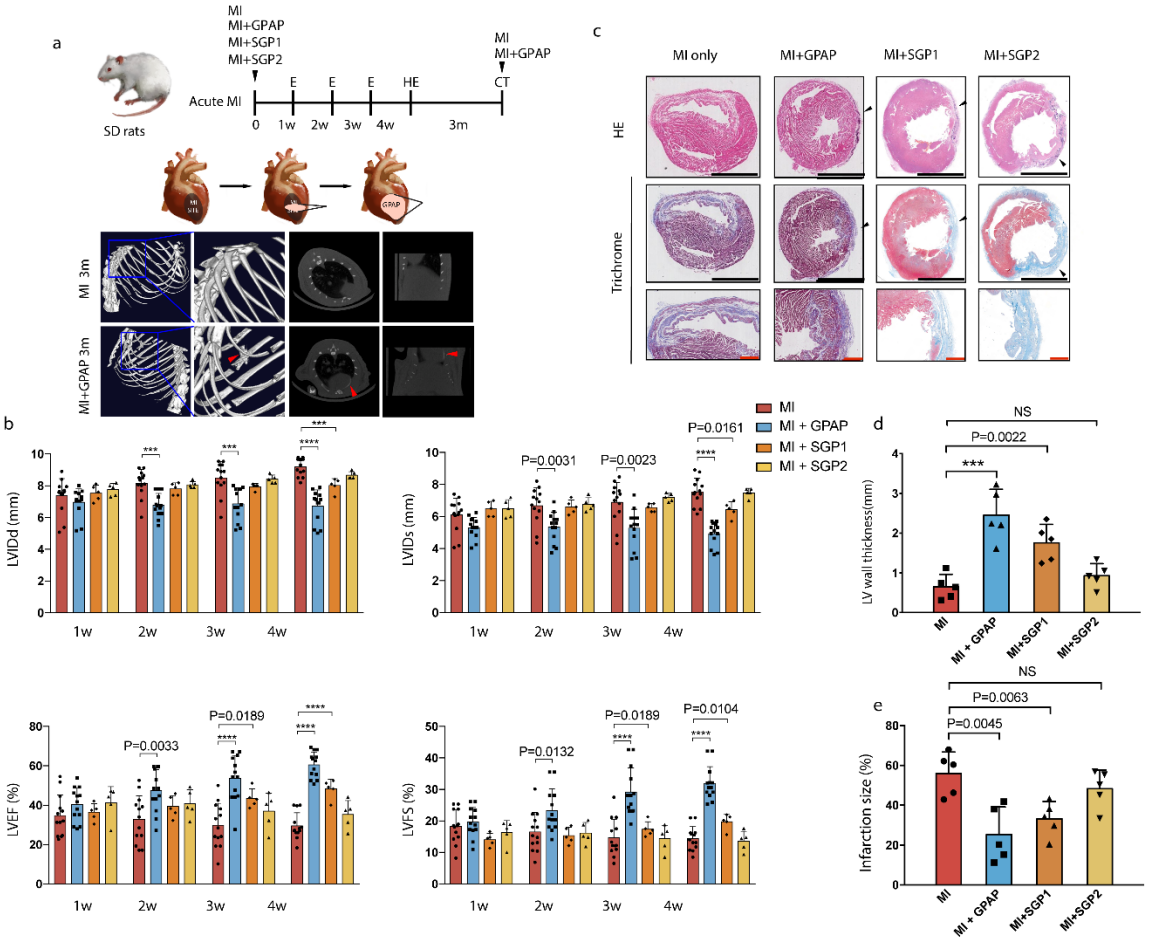

Figure 3.4. GPAP improved heart function and reduced pathological cardiac remodeling after acute MI. (a), Experimental design for testing treatment effects of GPAP, SGP1 and SGP2 in acute MI model (1-4 weeks) and Micro-CT images of MI rat heart patching with GPAP for 3 months (arrow heads). E, echocardiography; H, histology; CT, Micro-CT. **(**b), Echocardiographic assessment of cardiac function 4 weeks after patching with GPAP (n=13), SGP1 (n=5), SGP2 (n=5) and without treatment (n=13) in acute MI models. (c), HE and Masson's trichrome staining of heart sections 4 weeks after patching with GPAP, SGP1 and SGP2 in acute MI models. Black arrow heads indicate gel patches. Scale bars (black, 5 mm; red, 1 mm; yellow, 500 μm). (d)-(e), Statistics of the left ventricular wall thickness (d) and IS (e) 4 weeks after operation in acute MI models (n=5). Original data with their means and standard deviations are presented, $P>0.05$ non-significant (NS), ***$P<0.001$, ****$P<0.0001$, two-tailed

unpaired Student's t-test.

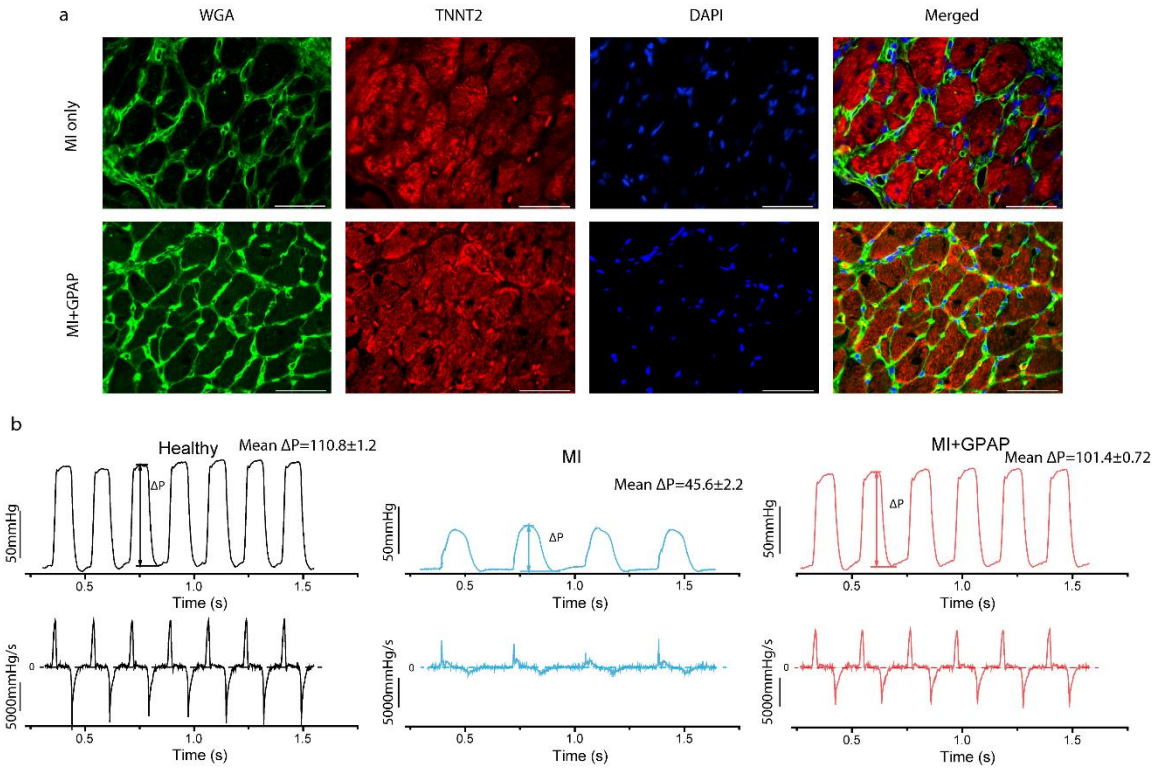

Figure 3.5 GPAP reduced myocyte hypertrophy and improved left ventricular systolic and diastolic functions after acute MI. (a), Heart sections were stained with wheat-germ agglutinin (green), TNNT2 (red) and DAPI (blue) 4 weeks after operation in acute MI models. Scale bars: 50μm. The experiments were repeated 3 times independently and each image represented at least 12 images taken. (b), Hemodynamic measurement of left ventricular functions (pressure and its changing rate) 4 weeks after patched with or without GPAP in acute MI models. Healthy rats served as control. The ΔP here were defined as the difference between the peak pressure of each stroke and the lowest pressure after relaxation. The means and the standard deviations were calculated on the strokes shown in the figure.

3.4 Conclusions

This simulation-guided design of epicardial patch points to a critical viscoelastic behavior at the gel point leading to a self-adaptive dynamic stiffness that balances the fluid and solid properties of the patch in response to cyclic deformation. This understanding reveals a mechanism by which an epicardial patch becomes self-adaptive to the time-

varying deformation of heart contraction-relaxation cycles, thereby not only appropriately restraining dilatation but also effectively reversing the decaying cardiac output following MI. Guided by this mechanism, we fabricate a viscoelastic adhesive epicardial patch, which to our knowledge creates a unique and safer solution for treating MI without additional agents or cells. It is also worth mentioning that the fabrication of GPAP is extremely simple and low in cost (material costs in our lab for 1 cm^2 GPAP with a thickness of 1 mm is less than a penny). This work paves the way for further investigations, including MI models of large animals and clinical studies, to fully uncover the translational value of the GPAP therapy. The simulation-based approach established here may also lead to the future design of customized GPAP according to patient's information, including the gender, age, infarction area, and individual-specific heart geometry, enabling more precision in treatment with improved simulation algorithms and fabrication techniques of GPAP for personalized needs. In addition, our findings set a promising mechanism and technology, expandable to further combine biological substances, such as cytokines, cells, and even engineered tissues, for perfecting the treatment of ischemic heart diseases in the future. Finally, it should also be noted that, apart from the ventricle system presented above, the mechanical design proposed in this study which balanced fluidity and solidity could potentially serve as a general principle to provide mechanical support on cyclic loaded biological or engineering systems, which usually lack a well-defined reference point for deformation. Although this clinical protocol used a mini-incision for implantation, with the appropriate equipment an injectable approach can be envisioned with this biomaterial technology.

Chapter 4

Mechanics of limpet teeth auxeticity

4.1 Introduction

Auxeticity, or negative Poisson's ratio, has been a material property of great research interest for a long time. When stretched longitudinally, an auxetic material will expand, instead of shrinking, transversely. It is theoretically admissible in linear elasticity yet rarely observed. Researchers proposed a variety of specifically designed structures to attain this exotic property. For example, re-entrant type of structures which effectively turn structural units into lever and pivot to achieve transverse expansion, were adopted in synthetic materials like foams (126) and metamaterials (127). Spin on chiral units is another popular deformation mechanism, incorporated with various materials and structures such as perforated silicone rubber elastomer (128) and metallic glass (129). With these auxetic materials and structures, many new inventions and applications become possible in architecture, clothing, acoustic adsorption and medical devices (130-133).

These materials exhibit large volumetric/areal variation under loading due to the nature of auxeticity. Under such consideration, a large volume of voids is usually an inevitable constituent for the engineered auxetic materials to accommodate the deformation. Yet the presence of voids can lead to a compromised strength due to the loss of load-bearing components, a significant drawback for many engineering materials. Therefore, how to combine the auxeticity with a high strength becomes a major challenge in material design.

One source of guidance can be biomaterials. Many biomaterials like cat skin(134),

cow teat skin(135), cancellous bone(136) and human tendon(137) are auxetic. On the other hand, many biomaterials have been widely studied and known to possess high strength or toughness. They usually have a composite structure at nanoscale, and a highly inhomogeneous deformation mechanism. In particular, an unparalleled high strength (27) was discovered in the teeth of limpet consisting of hydrated silica and goethite at nanoscale (138), and in this chapter we will show its leading edge exhibits auxeticity. Limpets are a kind of aquatic snails that mostly live on the intertidal rocks and feed themselves by scraping the algae off the rock surface with their toothed tongue-like structure called radula, on which grow rows of teeth formed by biomineralization. Then two questions arise: how do limpet teeth attain auxeticity without strength-degrading voids, and how can we translate the deformation mechanism in this strong biomaterial into our auxetic material design principle?

In this chapter we report a negative Poisson's ratio in the leading edge of the limpet teeth. We investigate and characterize their micro-structure and correlate them with the spin pattern during uniaxial tension obtained by digital image correlation (DIC). We will reveal that their micro-structure implements a spin-dominated deformation mechanism by orienting nanorods in a specific pattern. And inspired by the observed structure, we develop a representative element to mimic the deformation mechanism, and we find that such structure requires description from micropolar elasticity rather than the conventional linear elasticity. Through a parametric study we discover the significant correlation between auxeticity and the micropolar elasticity, and that the structural/material parameters of the nanorods in limpet teeth may be optimized for acquiring auxeticity.

4.2 Methods

4.2.1 Ab initio computation of goethite elasticity

To compute the elastic constants of goethite, ab initio computation is employed. Here we use the ab initio computation package VASP with the option IBRION=5, which computes the elastic constants of the goethite lattice by imposing displacement perturbation and thus obtaining the hessian matrix of the energy. Both the orthorhombic lattice structure and the obtained results are shown in **Fig. 4.1**. Note in limpet teeth the rod orientation aligns with the y-axis shown below.

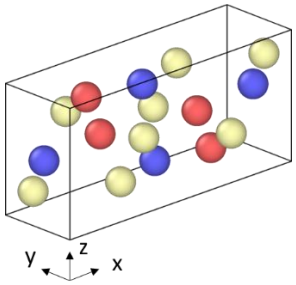

$$C = \begin{bmatrix} 288.6 & 98.0 & 84.0 & 1.5 & -2.3 & -0.8 \\ & 298.0 & 86.0 & 1.4 & -2.1 & -0.9 \\ & & 199.7 & 1.6 & -2.4 & 0.3 \\ & & & 93.6 & -0.03 & -0.06 \\ & & & & 84.2 & 1.4 \\ & & & & & 108.3 \end{bmatrix} \text{GPa}$$

Figure 4.1. The structure for ab initio computation (left) and the obtained elastic constants (right).

4.2.2 DIC on the experiment images

We employ the open-source digital image correlation package ncorr (139) to process the dark-field TEM images generated in uniaxial tension experiments. In DIC, the images before and after deformation are compared. For each region from the before-deformation image, the most correlated region on the after-deformation image is chosen, and therefore a displacement mapping $\big(u(\mathbf{x}), v(\mathbf{x})\big)$ is established, with which we can compute the strain field. The maximum iteration number of the correlation process is set to 100 for all images. The software package is modified to compute the spin around the out-of-plane axis, defined

as $\omega = \frac{1}{2}(\frac{\partial v}{\partial x} - \frac{\partial u}{\partial y})$. For one of the high resolution data sets (**Fig. 4.4d**) the raw images are small segments of the large sample image, and we stitch them together through the open-sourced image processing package ImageJ (140). During the DIC process, the regions of interests are manually chosen to cover as much of the center of the sample as possible and avoid the side regions where samples have different thickness. And the acquired strain fields $\epsilon_{\mathrm{xx}}(\mathbf{x})$ and $\epsilon_{\mathrm{yy}}(\mathbf{x})$ are averaged to obtain the mean $\bar{\epsilon}_{\mathrm{xx}}$ and $\bar{\epsilon}_{\mathrm{yy}}$, leading to the Poisson's ratio of the sample (here x is the loading direction) $\nu = -\bar{\epsilon}_{\mathrm{yy}}/\bar{\epsilon}_{\mathrm{xx}}$. The obtained spin field is further compared and correlated with the spatial pattern of the goethite nanorods.

4.2.3 Finite element modeling of a representative element

Here we locally homogenize the goethite-hydrated silica composite as an orthotropic material with in-plane isotropy, and therefore we only need to specify one material orientation. The theory adopted for homogenization is Mori-Tanaka theory, which needs the input of elastic constants of materials of both phases, $\lambda_{\mathrm{rod}}, \mu_{\mathrm{rod}}$ and $\lambda_{\mathrm{mat}}, \mu_{\mathrm{mat}}$, together with the effective rod aspect ratio and the volume fraction v of the goethite nanorods. Note here the rod aspect ratio is the "effective" value, which can be different from the real rod geometry. Discrepancy can arise due to the local variation of the rod orientation with a characteristic wavelength comparable with the rod length itself. Next, with the Eshelby's transformation tensor S_{ijkl} (rods align in x_1-direction) we define the following dimensionless constants (141):

$$D_1 = 1 + 2(\mu_{\mathrm{rod}} - \mu_{\mathrm{mat}})/(\lambda_{\mathrm{rod}} - \lambda_{\mathrm{mat}})$$

$$D_2 = (\lambda_{\mathrm{mat}} + 2\mu_{\mathrm{mat}})/(\lambda_{\mathrm{rod}} - \lambda_{\mathrm{mat}})$$

$$D_3 = \lambda_{\mathrm{mat}}/(\lambda_{\mathrm{rod}} - \lambda_{\mathrm{mat}})$$

$$B_1 = vD_1 + D_2 + (1-v)(D_1 S_{1111} + 2S_{2211})$$

$$B_2 = v + D_3 + (1-v)(D_1 S_{1122} + S_{2222} + S_{2233})$$

$$B_3 = v + D_3 + (1-v)[S_{1111} + (1+D_1)S_{2211}]$$

$$B_4 = vD_1 + D_2 + (1-v)(S_{1122} + D_1 S_{2222} + S_{2233})$$

$$B_5 = v + D_3 + (1-v)(S_{1122} + S_{2222} + D_1 S_{2233})$$

$$A_1 = D_1(B_4 + B_5) - 2B_2$$

$$A_2 = (1+D_1)B_2 - (B_4 + B_5)$$

$$A_3 = B_1 - D_1 B_3$$

$$A_4 = (1+D_1)B_1 - 2B_3$$

$$A_5 = (1-D_1)/(B_4 - B_5)$$

$$A = 2B_2 B_3 - B_1(B_4 + B_5)$$

And the longitudinal Young's modulus of the homogenized composite can be written as:

$$\frac{E_{\parallel}}{E_{mat}} = \frac{E_l}{E_{mat}} = \frac{1}{1 + v(A_1 + 2\nu_{mat}A_2)/A}$$

while the transverse Young's modulus of the homogenized composite is equal to:

$$\frac{E_{\perp}}{E_{mat}} = \frac{E_t}{E_{mat}} = \frac{1}{1 + v[-2\nu_{mat}A_3 + (1-\nu_{mat})A_4 + (1+\nu_{mat})A_5 A]/2A}$$

The in-plane shear modulus takes the form:

$$\frac{\mu_{lt}}{\mu_{mat}} = 1 + \frac{v}{\frac{\mu_{mat}}{\mu_{rod} - \mu_{mat}} + 2(1-v)S_{1212}}$$

And the out-of-plane shear modulus is:

$$\frac{\mu_t}{\mu_{mat}} = 1 + \frac{v}{\frac{\mu_{mat}}{\mu_{rod} - \mu_{mat}} + 2(1-v)S_{2323}}$$

Finally, the major Poisson's ratio of the composite reads (142):

$$\nu_{lt} = \frac{\nu_{mat}A - \nu(A_3 - \nu_{mat}A_4)}{A + \phi(A_1 + 2\nu_{mat}A_2)}$$

Inspired by the nanorod-matrix distribution pattern observed in TEM images, we construct the representative orientation pattern on a hexagon in order to obtain a macroscopic isotropy, as shown in **Fig. 4.6a-b**. Here we have a central circular node with radius r and an out-of-plane orientation, resembling the vertical bundle. Surrounding it are the six "arm" domains wherein the orientations mainly align towards one direction in each domain, in line with the horizontal bundle. But note we have smoothened the orientation pattern near the domain boundaries to avoid any orientational discontinuity. Together these domains form a spiral-like structure revolving around the central node. Such pattern is similar to the spiral structures used in some previous studies of engineered auxetic materials, but here no void is present and the spirals were constructed through material anisotropy instead. Then we apply the periodic boundary conditions upon all the diagonal side pairs on the hexagon, and subject the model to various loadings including tension, shear and body moment under plane-strain condition to characterize its micropolar elastic constants (see next section). We also put the model under a uniaxial tension under plane-stress condition, similar to the experiments, to characterize its Poisson's ratio ν and the overall Young's modulus E_{tot}.

4.2.4 Micropolar elasticity modeling characterization

In linear elasticity we consider the material strain as the only strain energy inducing variables. But for materials with micro-structures treatment beyond strain is required, as generally described in micromorphic elasticity. For the case of limpet teeth and the

representative element constructed in the previous section, we are specifically interested in the micropolar elasticity, where a microscopic spin is introduced to account for the rotational deformation on the microstructure. In such theory, both the macroscopic strain and the microscopic spin can induce stress, and the latter can lead to couple-stress as well. Here we consider the 2D scenario, where the constitutive relation for the stress can be written as (143):

$$\begin{bmatrix}\sigma_{11}\\ \sigma_{22}\\ \sigma_{12}\\ \sigma_{21}\end{bmatrix}=\begin{bmatrix}2\mu+\lambda & \lambda & -A & A\\ \lambda & 2\mu+\lambda & -A & A\\ A & -A & \mu+\kappa & \mu-\kappa\\ A & -A & \mu-\kappa & \mu+\kappa\end{bmatrix}\begin{bmatrix}u_{1,1}\\ u_{2,2}\\ u_{2,1}-\phi\\ u_{1,2}+\phi\end{bmatrix}$$

with $u_{i,j}$ being the displacement gradient, σ_{ij} the stress, and ϕ the microscopic spin around the out-of-plane axis. Note here the stress tensor may no longer be symmetric ($\sigma_{12} \neq \sigma_{12}$) as a body moment can exist. Also we don't include the couple stress here, which is related to the gradient of the ϕ and introduce a characteristic length. Apart from the classical Lamé constants (λ, μ) in linear elasticity, we need the extra parameters (A, κ). We will only focus on $|A|$ for the remaining of the chapter as the sign of A only represents the left or right-handed chirality of the structure, not a major concern in this study. To characterize these constants of the proposed representative element, we first put the structure under a tension and a shear loading. Then we fix the six vertices of the hexagonal element while rotating the boundary of the central node and therefore induce a body moment. The last loading condition is necessary to trigger the micropolar elastic mode of deformation in our test. But in a larger lattice (**Fig. 4.6b**) the micropolar elastic deformation can be triggered by a heterogeneous distribution of strain and stress as well. Among all loading conditions, the area-averaged spin around the out-of-plane axis inside the central node is treated as the microscopic spin ϕ, while the average displacement gradient and stress inside the entire

model are regarded as the $u_{i,j}$ and σ_{ij}. Next we write down all the constitutive relations for all loadings with $(\lambda, \mu, A, \kappa)$ as variables, and solve the equations with least-square error.

4.3 Results

4.3.1 Characterization of limpet teeth composition and microstructure

The teeth of limpet are comprised of goethite (a-FeOOH) crystals embedded in amorphous hydrated silica (SiO_2•nH_2O) matrix. The microstructure of the teeth has been characterized in-depth using various electron microscopy techniques to assess the composite structure over large length scales and across multiple dimensions (**Fig. 4.2**), which can be correlated with site-specific nano-mechanical testing. All goethite crystals in the limpet teeth have a nanorod shape but their shape, size and volume fraction in the leading edge facing the direction of scraping are greatly different from those in the trailing edge at the opposite side (**Fig. 4.3a**). The nanorods in the leading edge are characterized to have the diameter of 32.13 nm and the length of 279.03 nm in average and the volume fraction of 51.40%.

The nanorods in the leading edge are arranged in a distinct pattern – bundles of vertical nanorods are embedded in the sea of horizontally aligned nanorods (**Fig. 4.2c**). The three-dimensional microstructure reconstructed by transmission electron microscopy (TEM) tilt-series tomography confirmed that the particle shaped crystals surrounded by the horizontally aligned nanorods are actually the cross-section of the vertical nanorods of the same kind (**Fig. 4.3b**). The size of the vertical nanorod bundle is ~0.5-1 μm and the bundle-to-bundle distance is in the range of ~1 μm. The horizontal nanorods wrap the vertical nanorod bundle with aligning them in a revolving pattern (**Fig. 4.2c**). The scanning

transmission electron microscopy (STEM) energy-dispersive X-ray spectroscopy (EDS) analysis (**Fig. 4.2d**) as well as electron energy loss spectroscopy (EELS) (**Fig. 4.3c**) shows that the nanorods are consisted of Fe and O while the matrix is consisted of Si and O. As confirmed by high-resolution TEM (HRTEM) and STEM images as well as electron diffraction patterns (**Figs. 4.2e-g**), the nanorods are single crystalline goethite phase without structural defects, pores and cracks. The perfect crystallinity as well as the small size of nanorods could be consistent with nanostructural optimization in biological materials to ensure optimum strength and maximum tolerance of flaws (17). We note that there exists a few nm-thick surface layer on the nanorods at the interface with the matrix, which has a similar chemical composition but different atomic structure (**Figs. 4.2e,f** and **Fig. 4.3c**). In addition, there exists a transient layer in the matrix side where the chemical composition of the nanorod and the matrix change gradually (**Fig. 4.3c**).

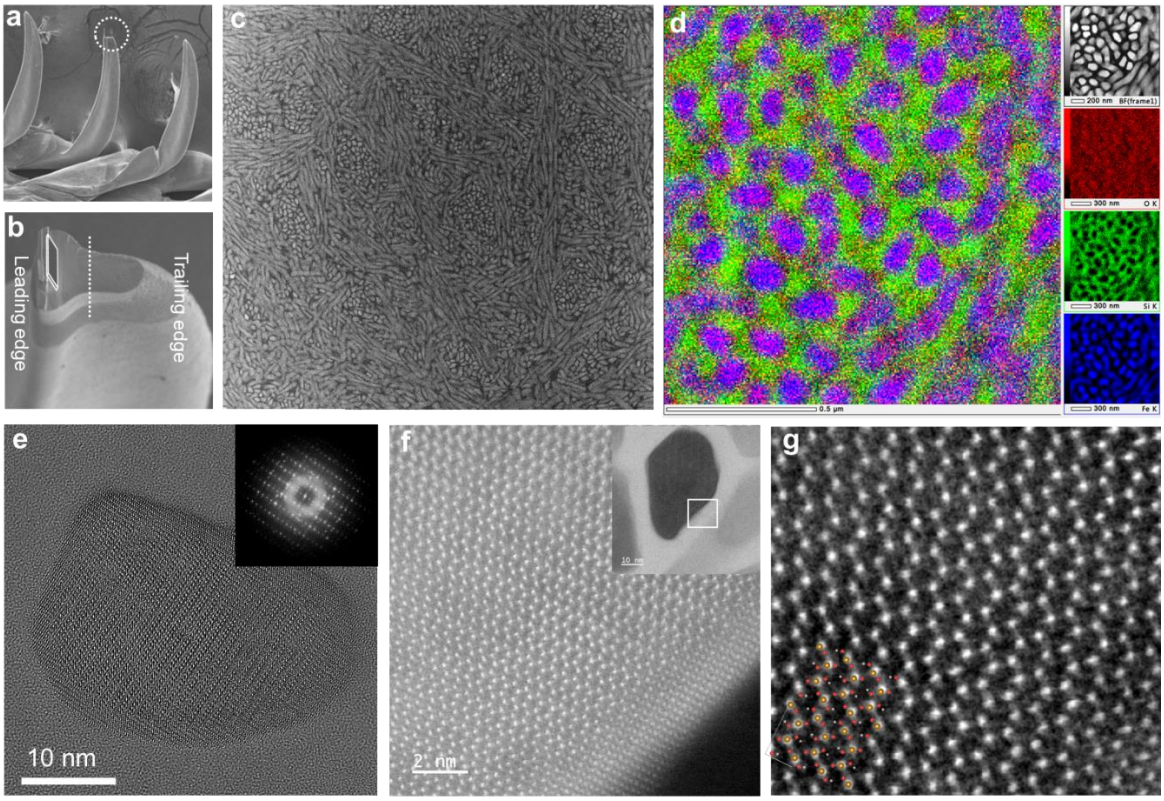

Figure 4.2. Microscopic imaging characterization of the limpet teeth with various electron microscopy techniques. (a) SEM image of limpet teeth. (b) Image of a limpet tooth cross-section, showing both a leading edge (where following samples are taken) and a trailing edge. (c) TEM image of the sample shown in (b), showing a complex of both vertically aligning goethite nanorods which tend to bundle together, and horizontally aligning rods. (d) STEM-EDS elemental mapping, where oxygen is marked red, silicon green and iron blue. (e-g) Atomic-resolution (S)TEM characterization of cross-section of a goethite nanorod at different resolution, which can show its orthorhombic crystal lattice structure.

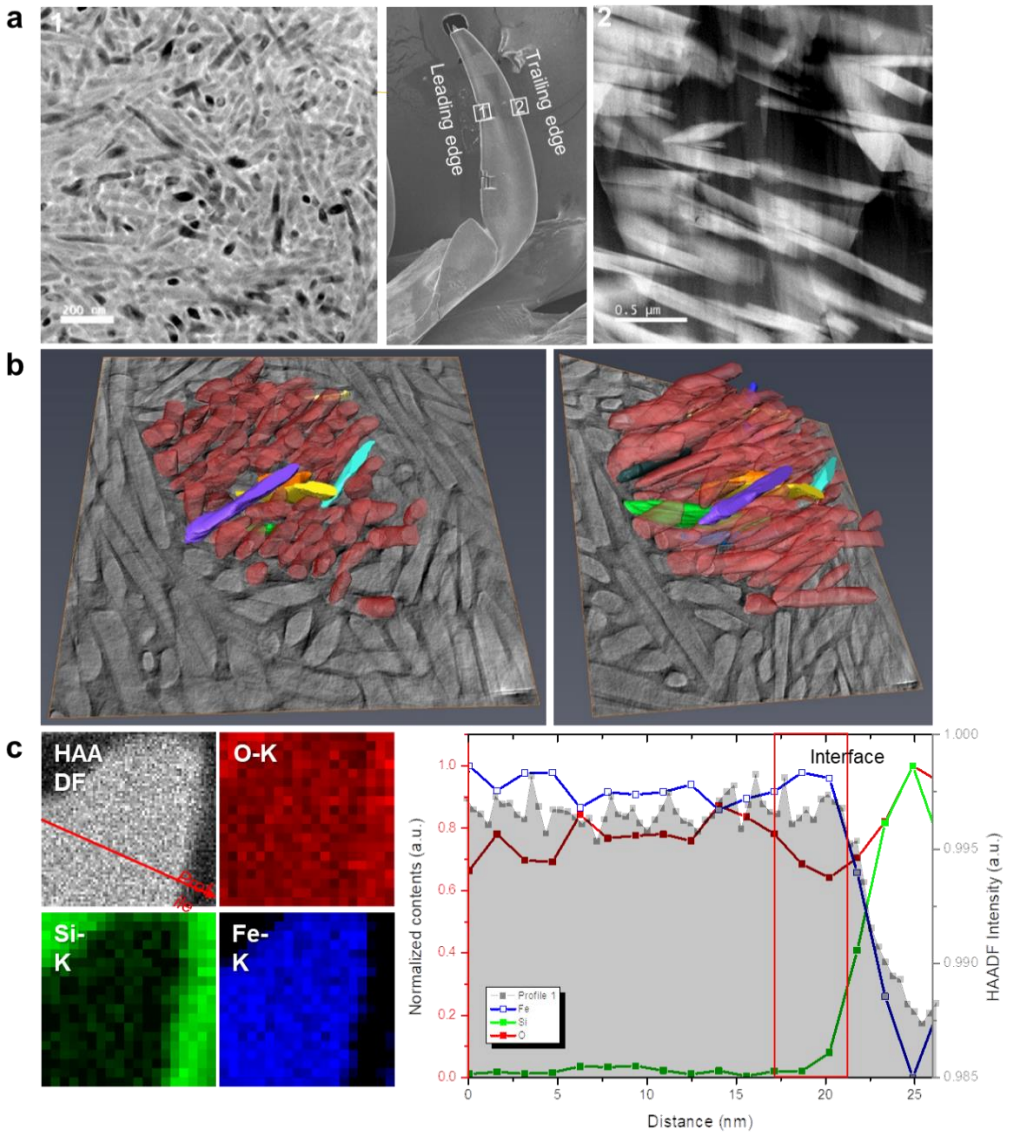

Figure 4.3. Further microscopic imaging characterization of the limpet teeth. (a) Comparison of TEM images between leading edge and the trailing edge. (b) 3D tomography reconstruction of the

microstructure of leading edge using series TEM images. (c) Elemental mapping with electron energy loss spectroscopy (EELS) across a nanorod cross-section.

4.3.2 DIC analysis of leading edge TEM image under uniaxial tension

To directly identify the auxetic deformation mechanism of the leading edge, we conducted in-situ TEM tensile straining experiments (**Fig. 4.4a**). The low magnification TEM images, recorded at the selected displacement and analyzed with digital image correlation technique, clearly show the large negative Poisson's ratio ($\nu = -0.54$) due to the increase in tensile strain in both the longitudinal and the transvers directions (**Fig. 4.4b**). The deformation microstructure analyzed with the DIC technique (**Fig. 4.4d**) shows a local revolution of the vertical nanorods in the bundles. A comparison of the TEM image and the DIC spin map shows that some vertical nanorod bundles correspond to the position of the local peak and valley of the rotation. The overlap of the TEM images taken at different strain values clearly visualizes the rotation of the individual vertical nanorod in a bundle (**Fig. 4.4c**). Thus, the collective and cooperative rotation of the vertical nanorods in the bundle resulting in a spin pattern could be the main microstructural origin leading to the observed auxeticity of the limpet tooth. We also performed DIC on high resolution image of a vertical-horizontal bundle complex, and it was revealed that such complex exhibited even lower local Poisson's ratio than the global field (**Fig. 4.5**). While models using rotating hinged squares and triangles could often replicate auxetic behavior, it is not always necessary to have empty space in a microstructure to achieve the auxetic behavior (144). In a natural material, climbing on one another of the nanostructures was suggested as the mechanism leading to a negative Poisson's ratio (145). The present work clearly shows that the rotation of nanostructures in the microstructure results in auxetic behavior. We

observed that the Poisson's ratio varies with strain and become positive value at a large strain, particularly close to the failure strain (**Fig. 4.5**). This indicates that the normal deformation behavior of positive Poisson's ratio is recovered when the collective and cooperative rotation of the nanorods is inactive. Note that the auxetic behavior was only observed in the longitudinal section of the leading edge, where the vertical nanorod bundles are embedded in the sea of horizontally aligned nanorods but not in other orthogonal sections from the leading edge. No auxetic behavior was observed in any sections of the trailing edge either.

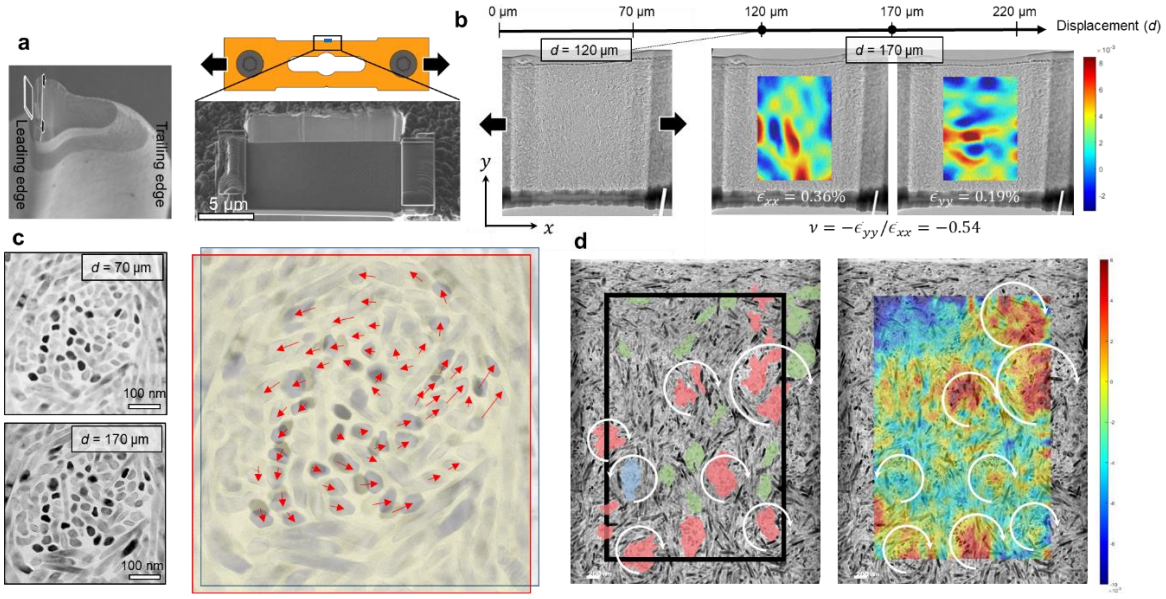

Figure 4.4. Displacement mapping and DIC analysis of uniaxial tension TEM images. (a) Experimental setup of the uniaxial tension test. (b) Uniaxial tension of sample at different mounter displacements d, and the DIC results of strains ϵ_{xx} and ϵ_{yy} which shows auxeticity. (c) Displacement mapping of vertical rods inside a vertical bundle during the uniaxial tension deformation step, which shows a revolving of vertical rods around the center of the bundle. (d) DIC result of spin pattern inside a deformation step. On the left the vertical bundles that are local spin peak (as shown in the DIC result on the right) are marked red, while the local spin valleys are marked green. The vertical bundles that are difficult to categorize are marked green. It can be observed that the vertical clusters have a strong correlation with the spin pattern.

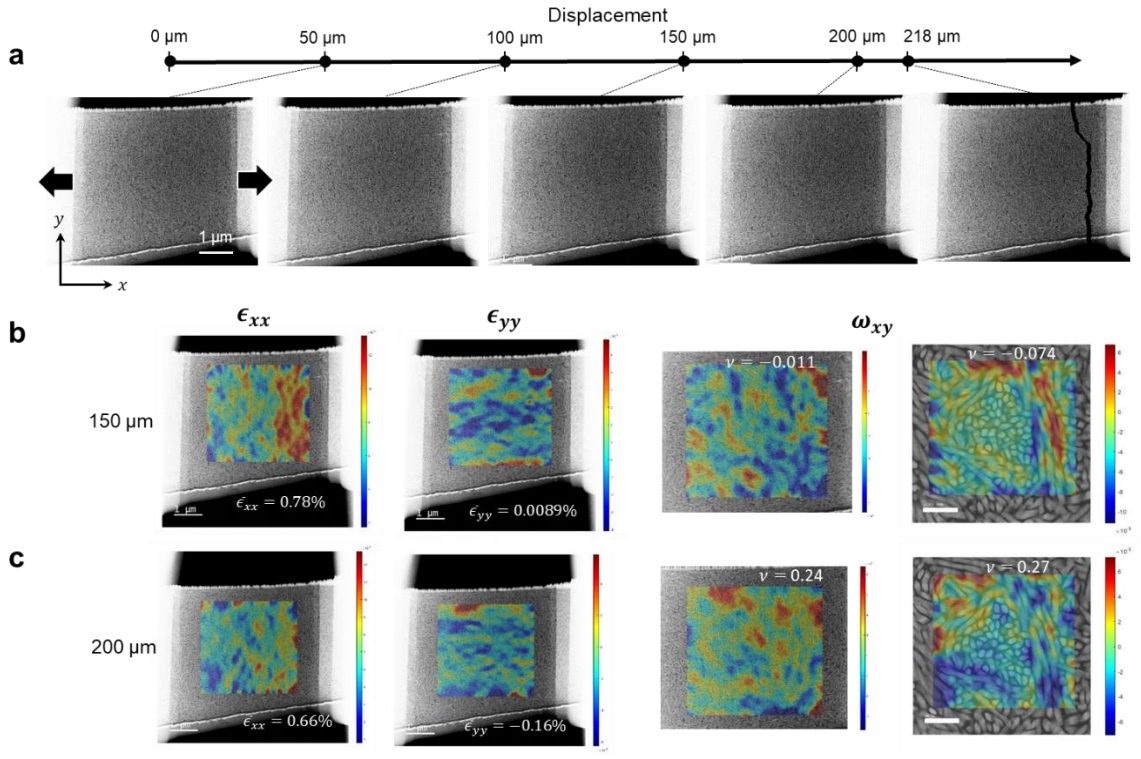

Figure 4.5. DIC analysis of uniaxial tension TEM images at different resolution. (a) Uniaxial tension of sample at different mounter displacements, up to sample fracture. (b-c) Strains ϵ_{xx}, ϵ_{yy} (left two columns), spin ω_{xy} at whole-sample resolution (third column) and zoomed-in high resolution (right column) obtained from DIC analysis during the deformation step between mounter displacement (b) 100-150 μm and (c) 150-200 μm. During (c) the 100-150 μm deformation step the Poisson's ratio is slightly negative ($\nu = -0.011$). But when zoomed into a complex with a vertical bundle and horizontal rods around it, the Poisson's ratio becomes more negative ($\nu = -0.074$). Also the spin pattern suggests the horizontal rods revolve around the vertical bundle. Yet in (d) the 150-200 μm, the Poisson's ratio turns positive on both the whole-sample resolution ($\nu = 0.24$) and the zoomed-in resolution ($\nu = 0.27$), whose revolving spin pattern also breaks down.

4.3.3 The microstructure attain auxeticity through micropolar elasticity

Inspired by the observation on the collective spin of nanorods during the deformation process, we construct a representative element of the microstructure in finite element modeling, with a spiral-like local material orientation aimed to mimic the microstructure in the TEM images. Locally, the nanorod-matrix composite is homogenized into a

transversely isotropic material with longitudinal modulus $E_{\parallel}$ and transverse modulus $E_{\perp}$ through Mori-Tanaka theory. The center node with an out-of-plane material orientation corresponds to the vertical bundle, while the six domains it around mimic the horizontal ones with in-plane orientations (**Fig. 4.6a,b**). We then characterize its 2D (plane-strain) micropolar elastic constant A, along with its Lamé constants λ, μ and plane-stress Poisson's ratio ν and Young's modulus E_{tot}. More details of the element can be found in the Section 4.2. The results can be found in **Fig. 4.6c-f**, where we plot the magnitude of micropolarity defined as $|A|/(\lambda+\mu)$, overall Poisson's ratio ν and overall Young's modulus E_{tot} against different relative center node size r/L and modulus anisotropy ratio $E_{\parallel}/E_{\perp}$. Note here different $E_{\parallel}/E_{\perp}$ values are obtained through different effective nanorod aspect ratios and relative nanorod moduli $E_{\mathrm{rod}}/E_{\mathrm{mat}}$ but they all fall under the same master curve governed by $E_{\parallel}/E_{\perp}$ (**Fig. 4.6c**), which thus is identified as the sole control parameter under given r/L. We also notice that $E_{\mathrm{rod}}/E_{\mathrm{mat}}$ needs to be larger than 10^2 to induce auxeticity, comparable in order with the modulus ratio between goethite (see Section 4.2) and hydrated silica (146). In **Fig. 4.6d-f**, an immediate observation is that larger $E_{\parallel}/E_{\perp}$ produces a lower Poisson's ratio. Besides, $|A|/(\lambda+\mu)$ and ν show a strong correlation under a given r/L: higher the micropolarity, lower the Poisson's ratio. Inside the parameter regime where the structure turns auxetic (enclosed by the black dashed line in **Fig. 4.6d**), the magnitude of $|A|/(\lambda+\mu)$ is no longer negligible. This means that the structure requires a micropolar elasticity description instead of the conventional linear elasticity, and that micropolar elasticity is the mechanism through which the auxeticity is achieved. Additionally, notice that (**Fig. 4.6d**) below $r/L < 0.3$ the parameter regime with auxeticity expands with increasing r/L, but when r/L exceeds 0.3, the auxeticity regime starts

shrinking with r/L. Therefore our model predicts $r/L{\sim}0.3$ should generates the maximum auxeticity. In **Fig. 4.4** the vertical bundle approximately occupies 20.1% of the area inside the black square, or equivalently has a $r/L{\sim}0.41$, comparable with the predicted most auxetic value. We also calculate the $E_{\parallel}/E_{\perp}$ given by Mori-Tanaka theory under different volume fraction (**Fig. 4.7**), and find that the highest value usually occur between volume fraction$\sim(50{,}60)\%$, in line with the 51% recorded in the experimental images. These observations imply that the microstructure of limpet teeth is specialized to acquire a Poisson's ratio as low as possible.

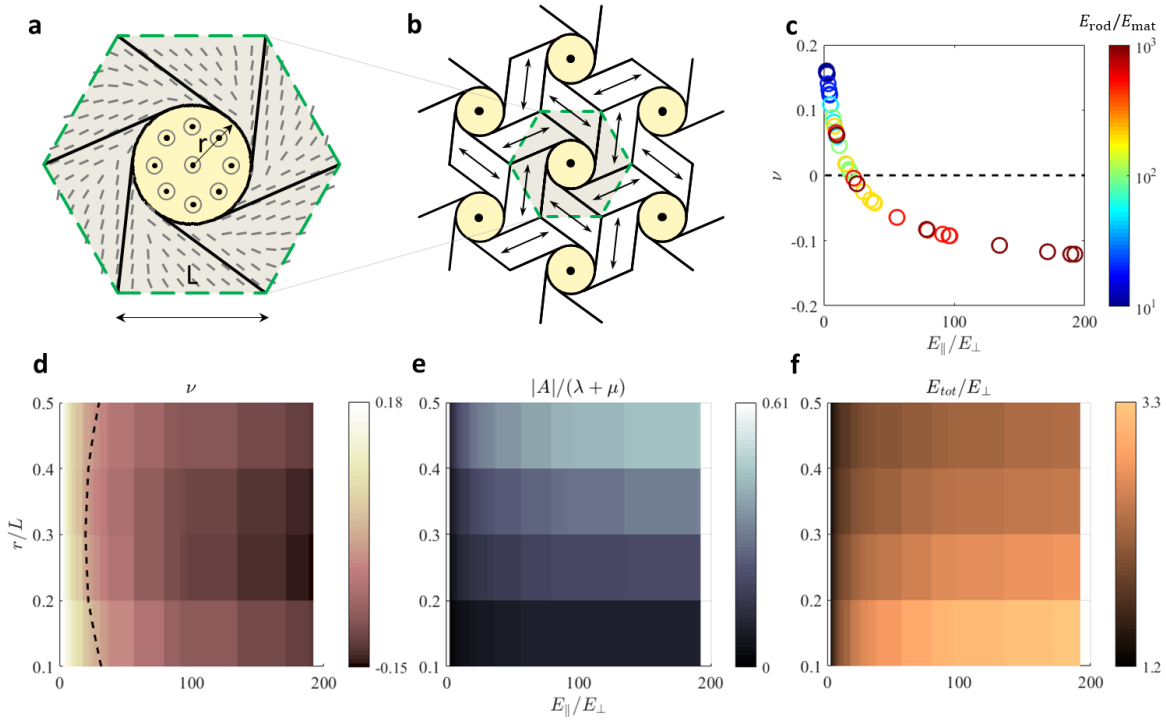

Figure 4.6. Micropolar elastic characterization of a limpet-teeth inspired hexagon representative structural element. (a) The material orientation inside the representative element. Inside the central node the orientation is out-of-plane, while in the six adjacent "arm" domains the orientation forms a revolving pattern. (b) Multiple elements assembled together and forming a chiral structure. (c) The Poisson's ratio under different $E_{\parallel}/E_{\perp}$ (volume fraction$= 51\%, r/L = 0.4$). Circles with the same color are computed with the same modulus ratios between nanorod and matrix $E_{\mathrm{rod}}/E_{\mathrm{mat}}$ yet different effective rod aspect ratio. All points fall on a master curve governed by $E_{\parallel}/E_{\perp}$. (d-f) The (d) Poisson's ratio (the approximate

boundary of $\nu < 0$ is marked by black dashed line), (e) micropolarity, defined as $|A|/(\lambda + \mu)$, and (f) Young's modulus of the element under different relative node size r/L and modulus anisotropy $E_{\parallel}/E_{\perp}$ ratio. Note here different $E_{\parallel}/E_{\perp}$ values are obtained through different effective nanorod aspect ratios and relative nanorod moduli $E_{\mathrm{rod}}/E_{\mathrm{mat}}$, but they all fall under the same master curve governed by $E_{\parallel}/E_{\perp}$.

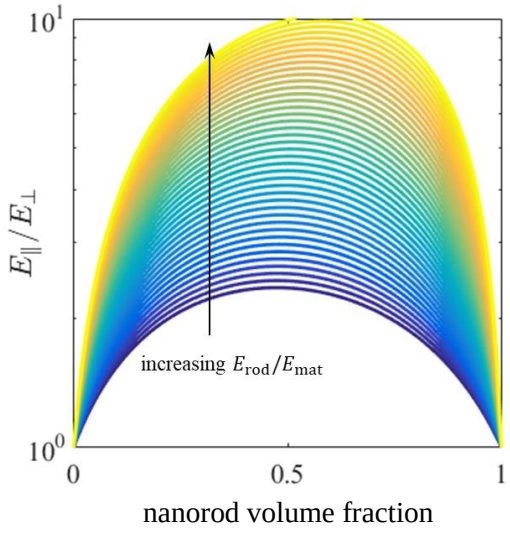

Figure 4.7. Anisotropic modulus ratio between longitudinal and transverse orientation in Mori-Tanaka theory, under different volume fraction of nanorod and modulus ratio between nanorod and matrix. Maximum anisotropy modulus ratio is usually attained between volume fraction$\sim$(0.5,0.6), which shows reasonable agreement with the experimentally observed value 0.51.

4.4 Discussion

Auxeticity is generally considered as a mutually exclusive mechanical properties with material strength in engineered materials, due to the inevitable introduction of voids to satisfy the volume variation. Yet here the limpet teeth provide a counter example to that idea. In limpet teeth, it was shown that arranging a heterogeneous micro-structure and harnessing the material anisotropy can fulfill a similar effect as placing voids and pores inside material as they share a similar deformation principle. For example, a beam unit

surrounded by voids transversely can actually be deemed as an anisotropic material with infinite longitudinal/transverse modulus ratio as the voids can be deformed indefinitely. Yet directly utilizing an anisotropic material as the structural unit can avoid the fragility accompanying the voids.

In the above study we mainly focused on the two-dimensional micro-structure of the limpet teeth in a planar sample. But the organization of the nanorods is actually three-dimensional, and the "horizontal" rods discussed above may also have vertical components in their orientation. Therefore, how the spin dominated deformation mechanism will function when extended to three-dimension can be an interesting topic. In the engineered structures three-dimensional patterns have been previously proposed to obtain either stronger auxeticity in a certain plane, or auxeticity in more than one plane (147). Besides, the observed micro-structure can imply a strong three-dimensional anisotropy of the material, and thus a full mechanical characterization of limpet teeth in multiple directions will provide valuable further insights into the behavior of this material. Actually, the area fraction of vertical bundle may be optimized to provide sufficient out-of-plane stiffness.

Right now, we have not identified what functionality limpet aim to achieve with the auxetic leading edge of their teeth. It was previously proposed that an auxetic material intrinsically possesses higher resistance against indentation as the material can flow towards the indenter upon contact, which can be a frequently-encountered loading condition given that the limpet teeth functions to scrape the rock surfaces that are usually rough and covered by other substances. We also hypothesize that the auxeticity of the limpet teeth may contribute to the high strength by interacting with the fracture process of the material as the function of teeth requires them to remain sharp even under frequent

usage.

4.5 Conclusions

In conclusion, we report a micro-structure assisted auxeticity of the leading edge of limpet teeth. By high resolution imaging techniques we identify the micro-structure of the goethite nanorods and the hydrated silica. During deformation the orientation of the nanorods is revealed to correlate with the spin distribution inside the material through DIC analysis. We further propose a structural representative element in finite element modeling to mimic the rod orientation pattern, which is characterized with micropolar elasticity theory. It is found that the micropolar elasticity can be essential to provide an effective characterization of the behavior of the structure, and highly correlated with the auxeticity. The discovery of this work sheds light on a new approach to obtain auxeticity through structure, and can provide insights on how to combine the auxeticity and strength in the future material design.

Chapter 5

Mechanical degradation of inhomogeneous liquid membrane through pore growth

5.1 Introduction

The growing antimicrobial resistance has become a global challenge. It was estimated that at least 700 thousand deaths every year were caused by antimicrobial-resistant infections, and the number could rise to 10 million every year by 2050 if no action is taken(148-150). Under such concern, an urgent need arises to accelerate the discovery of a new generation of antibiotics. One of the reasons for the failure of current antibiotics roots in the fact that under a hostile antibiotic environment certain bacteria will enter a dormant and non-growing state in which they are called persisters. Persisters can play a major role in the recalcitrance of chronic infection, yet the conventional antibiotics are ineffective against the persisters since their main target, biosynthesis, is substantially reduced in those bacteria(151). To tackle this issue, membrane-active antimicrobial agents(39) designed or selected to disrupt membrane's mechanical integrity start to attract increasing research interests and efforts because of their independence on the bacterial growth state. These agents can employ various modes of actions. For instance, daptomycin, the first clinically successful membrane-active antibiotic, was reported to induce membrane pore formation(152, 153), depolarization(154) and even lipid extraction(38). And such versatility also implies a low probability of bacterial to acquire resistance(39). Therefore, quantitative and theoretical insights into these damage mechanisms will be critical for the

purpose of future design and optimization of the membrane-active agents.

These agents usually introduce aggregation and form microdomains(38, 40, 41, 155). Previously, extensive studies have focused on the aggregation induced thermodynamic behaviors like phase segregation(156), blebbing(157), tubulation(158) and budding(159, 160) etc. Yet how it relates to membrane damage was rarely discussed in depth. In fluid mechanics a sharp interface between two infinite fluid domains was shown to facilitate bubble nucleation(161). And amyloidogenic peptides could cause leakage following their aggregation on membrane(162). Furthermore, external agents inducing curvature by an uneven distribution between leaflets were proposed to promote the pore nucleation(163, 164). Later for some membrane-rupturing peptides effective against Zika virus infection, the efficacy strongly depends on the vesicle radius at an order around 100nm, and smaller the radius, easier the rupture(165-167). These studies indicate the potential importance of inter-domain line tension and bilayer curvature during the damage process.

Another evidence connecting aggregation and damage was revealed in the recent papers on two newly discovered membrane-active molecules(40, 41) where the membrane failure processes were captured with camera (**Fig. 5.1a,b**). Initially a large number of aggregated micro-domains emerged after the antibiotic molecules entered the membrane, then the giant unilamellar vesicles (GUV) burst. And in molecular dynamics (MD) simulations the molecules would preferentially reside in the outer membrane leaflet due to a trans-leaflet energy barrier (**Fig. 5.1c,d**), which can produce an intrinsic curvature. Nevertheless, how the aggregated domains observed for both molecules quantitatively undermine the membrane resistance against rupture remains an open question.

In this chapter, to account for the experimental observation and elucidate the potential

aggregation-induced rupture mechanism, first we will go beyond the classical energy formula as a function of pore radius r for pore growth $F(r) = 2\pi r\gamma - \Sigma\pi r^2$ (with γ being the pore-edge line tension and Σ the surface tension) and establish a general theoretical framework to describe the pore growth process in a membrane with aggregated domains. Then through specific modeling of the curvature and the interface we show that, if the domain possesses an intrinsic radius of curvature below a certain characteristic length scale, the energy barrier will be significantly decreased. And a sufficiently sharp interface of a large domain could serve as a rupture site with lower energy barrier. With coarse-grained MD simulations we demonstrate that the critical tension and the work of rupture for a membrane can be lowered by both factors. The theoretical conclusions show good consistency with both the simulation and the experimental observation.

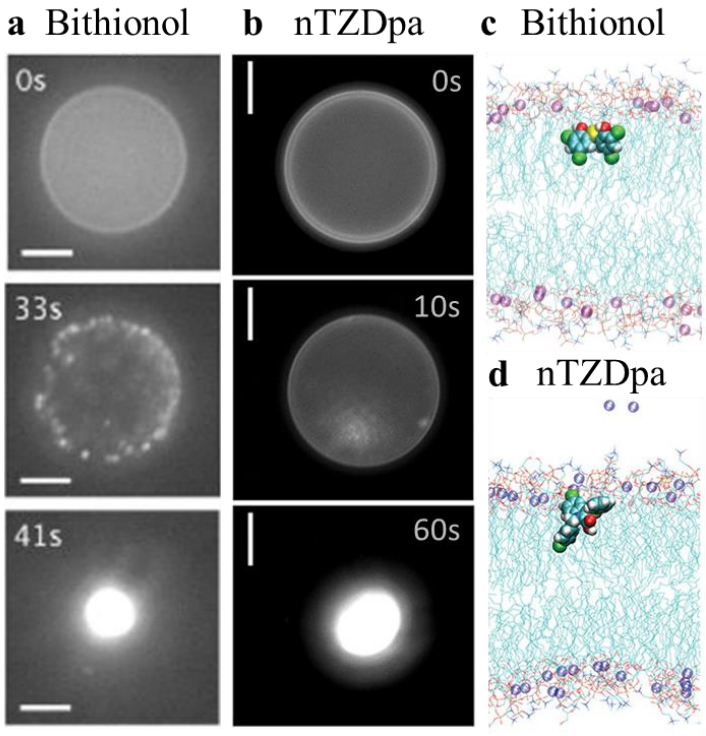

Figure 5.1. Experimental and MD simulation results of nTZDpa and bithionol interacting with GUVs mimicking bacterial membranes. Experiments on GUVs treated with 10μg/mL of (a) nTZDpa (scale

bars, 20μm) and (b) bithionol (scale bars, 10μm). Full-atom MD simulations of (c) a nTZDpa or (d) bithionol molecule penetrating bacterial membrane after 500ns. The nTZDpa images were taken from Ref (40) and the bithionol images from Ref (41).

5.2 Model and methods

5.2.1 General theoretical framework for pore growth on membrane with an inclusion

Here we consider an infinite lipid surface (L) with a finite inclusion domain (I) and a free pore edge (P) in it (**Fig. 5.2**). Note the membrane should be asymptotically flat at infinity, where a surface tension Σ is imposed. Below $\mathbf{e}$, and $\boldsymbol{\nu}$ each denotes the local tangent and tangent-normal vector along a curve while $\mathbf{n}$ is the surface normal, while κ_g denotes the geodesic curvature. The free energy can thus be written as:

$$\mathrm{F}_0 = \int_{\Omega_\mathrm{L}} \psi_L \mathrm{dA} + \int_{\Omega_I} \psi_I \mathrm{dA} + \int_{\partial\Omega_L \cap \partial\Omega_I} \gamma_{L-I} \mathrm{d}s + \int_{\partial\Omega_L \cap \partial\Omega_P} \gamma_{L-P} \mathrm{d}s + \int_{\partial\Omega_I \cap \partial\Omega_P} \gamma_{I-P} \mathrm{d}s - \int_{\partial\Omega_\Sigma} \Sigma \mathrm{u}_\nu \mathrm{d}s$$

Here ψ_L and ψ_I are non-negative bending energy densities in the lipid and the inclusion phase, as functions of mean curvature H and Gaussian curvature K. Three γs are the interfacial line tensions between domains denoted by the subscripts. u_ν is the in-plane tangent-normal displacement. Now perturb the system with infinitesimal displacement $\delta\mathbf{u}$ with three constraints: the pore-edge area increment, defined as $-\int_{\partial\Omega_P} \delta\mathbf{u}\cdot\boldsymbol{\nu}\mathrm{d}s$, needs to be $\delta A_P = \int_{\partial\Omega_P} \delta r \mathrm{d}s$ (δr can be regarded as the mean $-\delta\mathbf{u}\cdot\boldsymbol{\nu}$ on the pore edge), while the areas of the lipid and the inclusion domains should be conserved. Then with Lagrangian multipliers Π_P, Π_L and Π_I for each constraint, the free energy can be written as:

$$\delta F = \delta F_0 + \Pi_P \left(\int_{\partial\Omega_P} \delta\mathbf{u} \cdot \boldsymbol{\nu} \mathrm{d}s + \int_{\partial\Omega_P} \delta r \mathrm{d}s \right)$$
$$+ \Pi_L \left(\int_{\partial\Omega_L \cap \partial\Omega_P} \delta\mathbf{u} \cdot \boldsymbol{\nu} \mathrm{d}s - \int_{\partial\Omega_L \cap \partial\Omega_I} \delta\mathbf{u} \cdot \boldsymbol{\nu} \mathrm{d}s + \int_{\partial\Omega_L \cap \partial\Omega_\Sigma} \delta\mathbf{u} \cdot \boldsymbol{\nu} \mathrm{d}s \right)$$
$$+ \Pi_I \left(\int_{\partial\Omega_I \cap \partial\Omega_P} \delta\mathbf{u} \cdot \boldsymbol{\nu} \mathrm{d}s + \int_{\partial\Omega_L \cap \partial\Omega_I} \delta\mathbf{u} \cdot \boldsymbol{\nu} \mathrm{d}s \right)$$

Note that on $\partial\Omega_L \cap \partial\Omega_I$ the tangent-normal $\boldsymbol{\nu}$ is defined as pointing from the inclusion domain towards the lipid domain (**Fig. 5.2**), and that $\partial\Omega_I \cap \partial\Omega_\Sigma = \emptyset$ as the inclusion is finite. From above formula we know that the system energy variation from δA_P is $\int_{\partial\Omega_P} \Pi_P \delta r \mathrm{d}s$, which is the only term we are interested in. Therefore, we just need to solve for Π_P. As all multipliers are only associated with $\delta\mathbf{u} \cdot \boldsymbol{\nu} = \delta u_{\boldsymbol{\nu}}$ on the domain boundaries, below we will only consider the boundary terms with $\delta u_{\boldsymbol{\nu}}$ from δF_0 as well. From (168, 169), we know the interested terms will be:

$$\delta F_0|_{\partial\Omega, \delta\mathbf{u}\cdot\boldsymbol{\nu}} = \int_{\partial\Omega_L \cap \partial\Omega_P} \psi_L \delta u_{\boldsymbol{\nu}} \mathrm{d}s + \int_{\partial\Omega_I \cap \partial\Omega_P} \psi_I \delta u_{\boldsymbol{\nu}} \mathrm{d}s + \int_{\partial\Omega_L \cap \partial\Omega_I} (\psi_I - \psi_L) \delta u_{\boldsymbol{\nu}} \mathrm{d}s$$
$$+ \int_{\partial\Omega_L \cap \partial\Omega_I} \gamma_{L-I} \kappa_{\mathrm{g}} \delta u_{\boldsymbol{\nu}} \mathrm{d}s + \int_{\partial\Omega_L \cap \partial\Omega_P} \gamma_{L-P} \kappa_{\mathrm{g}} \delta u_{\boldsymbol{\nu}} \mathrm{d}s$$
$$+ \int_{\partial\Omega_I \cap \partial\Omega_P} \gamma_{I-P} \kappa_{\mathrm{g}} \delta u_{\boldsymbol{\nu}} \mathrm{d}s - \int_{\partial\Omega_\Sigma} \Sigma \delta u_{\boldsymbol{\nu}} \mathrm{d}s + \delta F_{0, \partial\Omega_L \cap \partial\Omega_I \cap \partial\Omega_P}$$

The term $\delta F_{0, \partial\Omega_L \cap \partial\Omega_I \cap \partial\Omega_P}$ will be zero if $\partial\Omega_L \cap \partial\Omega_I \cap \partial\Omega_P = \emptyset$ which implies $\partial\Omega_L \cap \partial\Omega_P$ and $\partial\Omega_I \cap \partial\Omega_P$ are either empty or a closed curve. Otherwise it will give the force balance:

$$\gamma_{L-P}(\mathbf{e})_{\partial\Omega_L \cap \partial\Omega_P}|_{s_0}^{s_1} + \gamma_{I-P}(\mathbf{e})_{\partial\Omega_I \cap \partial\Omega_P}|_{s_0}^{s_1} + \gamma_{L-I}(\mathbf{e})_{\partial\Omega_L \cap \partial\Omega_I}|_{s_0}^{s_1} = 0$$

Here s_0 denotes the beginning point of each curve and s_1 denotes the end point, both of which should locate on $\partial\Omega_L \cap \partial\Omega_I \cap \partial\Omega_P$. Note the directions of these curves are compatible with the definition of $\mathbf{n}$ and $\boldsymbol{\nu}$ (e.g. the ones shown in **Fig. 5.2**).

Then equating all terms with δu_v to zero we can obtain the following equations:

$$\Pi_L - \Sigma = 0 \text{ on } \partial\Omega_\Sigma$$

$$\Pi_I - \Pi_L + \psi_I - \psi_L + \gamma_{I-L}\kappa_{\mathrm{g}} = 0 \text{ on } \partial\Omega_L \bigcap \partial\Omega_I$$

$$\Pi_P + \Pi_L + \psi_L + \gamma_{L-P}\kappa_{\mathrm{g}} = 0 \text{ on } \partial\Omega_L \bigcap \partial\Omega_P$$

$$\Pi_P + \Pi_I + \psi_I + \gamma_{I-P}\kappa_{\mathrm{g}} = 0 \text{ on } \partial\Omega_I \bigcap \partial\Omega_P$$

These are the boundary conditions for the shape of the membrane. Then we can solve that

$$\Pi_P = -\left(\psi_L + \Sigma + \gamma_{L-P}\kappa_{\mathrm{g}}\right)_{\partial\Omega_L \cap \partial\Omega_P}$$

$$= \left(\psi_I - \psi_L + \gamma_{L-I}\kappa_{\mathrm{g}}\right)_{\partial\Omega_L \cap \partial\Omega_I} - \left(\psi_I + \Sigma + \gamma_{I-P}\kappa_{\mathrm{g}}\right)_{\partial\Omega_I \cap \partial\Omega_P}$$

Therefore, the energy variation associated with the pore area increment will be:

$$\delta F = \int_{\partial\Omega_P} \Pi_P \delta r \mathrm{d}s$$

$$= \int_{\partial\Omega_L \cap \partial\Omega_P} -\left(\psi_L + \Sigma + \gamma_{L-P}\kappa_{\mathrm{g}}\right)\delta r \mathrm{d}s + \int_{\partial\Omega_I \cap \partial\Omega_P} -\left(\psi_I + \Sigma + \gamma_{I-P}\kappa_{\mathrm{g}}\right)\delta r \mathrm{d}s$$

$$+ \left(\psi_I - \psi_L + \gamma_{L-I}\kappa_{\mathrm{g}}\right)_{\partial\Omega_L \cap \partial\Omega_I} \int_{\partial\Omega_I \cap \partial\Omega_P} \delta r \mathrm{d}s$$

From above formula we can immediately observe that positive bending energy densities ψ_L and ψ_I on the pore edge can induce extra driving force for pore growth, similar to the energy release rate in fracture mechanics. But if no intrinsic curvature is present in the system, ψ_L and ψ_I will be both zero. Here a resistance against pore growth can emerge from $\left(\gamma_{L-I}\kappa_{\mathrm{g}}\right)_{\partial\Omega_L \cap \partial\Omega_I}$ due to inter-domain interface if $\partial\Omega_I \bigcap \partial\Omega_P \neq \emptyset$, yet if the inclusion is much larger than the pore, $\left(\kappa_{\mathrm{g}}\right)_{\partial\Omega_L \cap \partial\Omega_I}$ will be negligible.

For the next step, on the condition that $\partial\Omega_L \cap \partial\Omega_I \cap \partial\Omega_P \neq \emptyset$ and thus the pore locates on the domain boundary, we look into a specific type of displacement perturbation

$\delta\mathbf{u}$ such that along pore edge $\delta\mathbf{u} = \delta u_{\mathbf{e}}\mathbf{e} + \delta u_{\boldsymbol{\nu}}\boldsymbol{\nu} + \delta u_{\mathbf{n}}\mathbf{n}$ satisfies $\delta u_{\boldsymbol{\nu}} = -\delta r$ and $\delta u_{\mathbf{n}} = 0$. Using the identity: $\delta\int ds = \int \left(\delta u'_{\mathbf{e}} - \kappa_n \delta u_{\mathbf{n}} + \kappa_{\mathrm{g}}\delta u_{\boldsymbol{\nu}}\right)ds$ on the pore edge and the force balance on the tri-junction points $\partial\Omega_L \bigcap \partial\Omega_I \bigcap \partial\Omega_P$ we obtain:

$$\int_{\partial\Omega_L\cap\partial\Omega_P} -\gamma_{L-P}\kappa_{\mathrm{g}}\delta r\mathrm{d}s + \int_{\partial\Omega_I\cap\partial\Omega_P} -\gamma_{I-P}\kappa_{\mathrm{g}}\delta r\mathrm{d}s$$

$$= \int_{\partial\Omega_L\cap\partial\Omega_P} \gamma_{L-P}\kappa_{\mathrm{g}}\delta u_{\boldsymbol{\nu}}\mathrm{d}s + \int_{\partial\Omega_I\cap\partial\Omega_P} \gamma_{I-P}\kappa_{\mathrm{g}}\delta u_{\boldsymbol{\nu}}\mathrm{d}s$$

$$= \gamma_{L-P}\delta\int_{\partial\Omega_L\cap\partial\Omega_P} \mathrm{d}s + \gamma_{I-P}\delta\int_{\partial\Omega_I\cap\partial\Omega_P} \mathrm{d}s - \gamma_{L-P}(\mathbf{e}\cdot\delta\mathbf{u})_{\partial\Omega_L\cap\partial\Omega_P}|_{s_0}^{s_1}$$

$$- \gamma_{I-P}(\mathbf{e}\cdot\delta\mathbf{u})_{\partial\Omega_I\cap\partial\Omega_P}|_{s_0}^{s_1}$$

$$= \gamma_{L-P}\delta\int_{\partial\Omega_L\cap\partial\Omega_P} \mathrm{d}s + \gamma_{I-P}\delta\int_{\partial\Omega_I\cap\partial\Omega_P} \mathrm{d}s + \gamma_{L-I}(\mathbf{e}\cdot\delta\mathbf{u})_{\partial\Omega_L\cap\partial\Omega_I}|_{s_0}^{s_1}$$

Here the first two terms represent the total increment of line tension along the pore edge, while the last term shows the increment/reduction of the inter-domain line tension. Usually for a displacement on an expanding pore edge we will have $(\mathbf{e}\cdot\delta\mathbf{u})_{\partial\Omega_L\cap\partial\Omega_I\cap\partial\Omega_P} < 0$, another extra driving force for pore growth. Thus, combining the all previous derivations we conclude that both the inter-domain line tension and the curvature can contribute extra driving force for the pore growth, when the inclusion is adequately large.

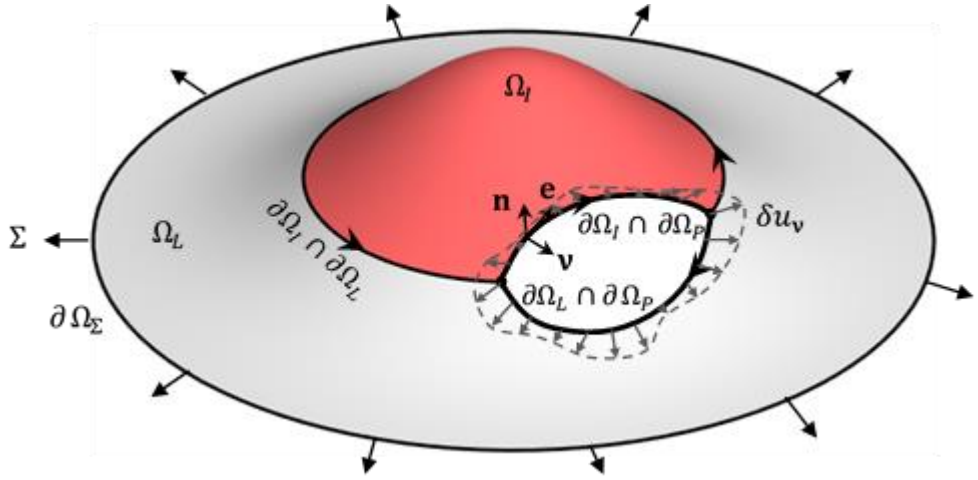

Figure 5.2. A general setup with an infinite lipid domain Ω_L, a finite inclusion domain Ω_I and a pore.

5.2.2 Pore in an inclusion with intrinsic curvature

We start with a scenario with a positive bending energy in the system caused by an intrinsic curvature of the inclusion, yet $\partial\Omega_L \cap \partial\Omega_I \cap \partial\Omega_P = \emptyset$ and $\gamma_{L-I} = 0$. Specifically, for simplicity we assume that the system is axisymmetric for which the highest bending energy density will be at the system center, and that the pore emerges at the center of the inclusion. The schematic of the system is demonstrated in **Fig. 5.4a**. For simplicity, we assume the pore of given radius r_0 exists at the center of a circular inclusion domain with intrinsic curvature c_0 and the same bending modulus κ_b, Gaussian modulus κ_G and pore-edge line-tension γ as the matrix. We also assume no line tension between two phases. Under an axisymmetric setup, the geometry of the membrane can be described by the tangent angle $\psi(s)$ and the radius $r(s)$ along the arc length s. The membrane is under a surface tension Σ and the inclusion area is conserved as $A_I = \pi R_I^2$. We adopt the non-dimensionalization: $\bar{s} = s\gamma_{L-P}/\kappa_b$, $\bar{r} = r\gamma_{L-P}/\kappa_b$, $\bar{R}_I = R_I\gamma_{L-P}/\kappa_b$, $\bar{c}_0 = c_0\kappa_b/\gamma_{L-P}$, $\bar{\Sigma} = \Sigma\kappa_b/\gamma_{L-P}^2$, $\bar{\kappa}_G = \kappa_G/\kappa_b$ and the free energy $\bar{F} = F/(2\pi\kappa_b)$. Then the system free

energy reads as(170):

$$\bar{F} = \int_0^{\infty} \bar{r}\left[\frac{1}{2}\left(\dot{\psi} + \frac{\sin\psi}{\bar{r}} + \bar{c}_0\right)^2 + \bar{\Sigma}(1-\cos\psi)\right]\mathrm{d}\bar{s} + \bar{\kappa}_G(\cos\psi(0)-1)$$

$$+ \Gamma\left(\int_{\Omega_I} \bar{r}\mathrm{d}\bar{s} - \frac{\bar{R}_I^2}{2}\right)$$

Here note that $\bar{c}_0$ is non-zero only inside the inclusion domain. Γ is the Lagrangian multiplier to enforce the inclusion area conservation. The overhead dot means derivative with respect to the arclength. Minimizing the axisymmetric membrane free energy yields the governing equations for the membrane shape (160):

$$\begin{cases} \ddot{\psi} = \frac{1}{\bar{r}}\left(\frac{\sin\psi\cos\psi}{\bar{r}} + \bar{\Sigma}\bar{r}\sin\psi - \dot{\psi}\cos\psi + \frac{\mu}{2}\sin\psi\right) \\ \dot{\mu} = \left(\dot{\psi} + \bar{c}_0\right)^2 - \frac{\sin^2\psi}{\bar{r}^2} + 2\bar{\Sigma}(1-\cos\psi) + \Gamma \\ \dot{\bar{r}} = \cos\psi \end{cases}$$

The associated boundary condition at the free pore edge is $\dot{\psi}(0) + \left(1+\bar{\kappa}_g\right)\sin\psi(0)/\bar{r}_0 + \bar{c}_0 = 0$. On the outer boundary we have asymptotic flatness conditions $\lim_{t\to\infty}\psi(t) = 0$ and $\lim_{t\to\infty}\dot{\psi}(t) = 0$. Inside the inclusion domain the solution is called the inner solution, otherwise it's called the outer solution. At the inclusion-matrix interface we need three balance conditions (denoting the arclength of the inner solution as S)

$$\dot{\psi}^2(S^+) - \dot{\psi}^2(S^-) = \left(\frac{\sin\psi(S)}{r(S)}\right)^2 - \left(\frac{\sin\psi(S)}{r(S)} + \bar{c}_0\right)^2 - \Gamma$$

$$\ddot{\psi}(S^+) - \ddot{\psi}(S^-) = -\bar{c}_0\frac{\cos\psi(S)}{r(S)}$$

$$\dot{\psi}(S^+) - \dot{\psi}(S^-) = \bar{c}_0$$

which each implies the balance of tangential force, normal force and torque, respectively. But to solve this problem numerically, instead of directly imposing above conditions at the

interface we vary $\psi(S)$ and $\bar{r}(S)$ within a certain range and use them as boundary conditions for both inner and outer solutions. Then we choose the one with lowest energy from all solutions, as was shown to satisfy all three balance conditions(171). Here we vary $\bar{r}_0$ and record the free energy to obtain the energy barrier. We take $\bar{\Sigma} = 0.25$ and $\bar{\kappa}_G = -0.9$(172, 173).

5.2.3 Pore in a gradient transition zone between two domains: theory

In this section we aim to analyze a general scenario of domain boundary. Instead of a sharp interface separating two distinct phases, we consider a gradient zone where the composition varies smoothly due to entropic effect. In fact physically this is a more realistic scenario while the sharp interface is only a simplified mathematical representation. For this purpose, the following model system is constructed (**Fig. 5.5a**). We assume, as a simple representation of a gradient zone with width L, that the pore-edge line tension varies linearly across it, $\gamma_P = \gamma_{L-P} + g \cdot x$. For the inclusion-lipid interaction we impose a positive gradient energy: $G(g)$. We also take $g > 0$, and the system is under surface tension Σ. For simplicity we ignore the bending energy density in the free energy and thus only consider a planar membrane. This way the total energy of the system can be written as:

$$\delta F = \sum_{i=1,2,3} \delta \int \left(\gamma_P^{(i)} - \Sigma y^{(i)} \cos\varphi^{(i)}\right) \mathrm{d}s^{(i)} - G(g)\delta \int y^{(2)} \cos\varphi^{(2)}\ \mathrm{d}s^{(2)} + \Pi_P \left(\int_{\partial\Omega_P} \delta u_{\mathbf{v}} \mathrm{d}s + \int_{\partial\Omega_P} \delta r \mathrm{d}s\right)$$

We use superscripts i =1,2 and 3 to indentify pore edge in the matrix phase, gradient zone and inclusion phase, respectively. $s^{(i)}$ is the arclength and $\varphi^{(i)}$ and $y^{(i)}$ are the associated

pore edge tangent angle and height.

Note in above formula, the term $-G(g)\delta\int y^{(2)}\cos\varphi^{(2)}\ \mathrm{d}s^{(2)}$ is physically the same as the $\gamma_{L-I}(\mathbf{e}\cdot\delta\mathbf{u})_{\partial\Omega_L\cap\partial\Omega_I}|_{s_0}^{s_1}$ term in the general theoretical framework. Therefore, we only need to analyze the contribution from $\delta\int\left(\gamma_P^{(2)}-\Sigma y^{(2)}\cos\varphi^{(2)}\right)\mathrm{d}s^{(2)}$. After collecting all the terms in front of $\delta u_{\boldsymbol{\nu}}$ and equal them to zero, we obtain:

$$\Pi_P+\Sigma+\gamma_{L-P}\kappa_g=0 \text{ on } \partial\Omega_L\bigcap\partial\Omega_I$$

$$\Pi_P+\Sigma+\gamma_{I-P}\kappa_g=0 \text{ on } \partial\Omega_I\bigcap\partial\Omega_P$$

$$\Pi_P+G(g)+\Sigma+\gamma_P\kappa_g+g\boldsymbol{\nu}\cdot\hat{\boldsymbol{x}}=0 \text{ on } \partial\Omega_G\bigcap\partial\Omega_P$$

Here $\partial\Omega_G$ is the pore edge in the gradient zone, while $\hat{\boldsymbol{x}}$ is the unit basis vector in x-direction. Note the first two equations conform to the classical 2D Young-Laplace equation. As we are interested in the height of energy barrier, $\Pi_P=\delta F/\delta r$ can be assumed positive. $G(g)$, the gradient energy, also needs to be positive. Thus the terms $\Sigma+\gamma_P\kappa_g+g\boldsymbol{\nu}\cdot\hat{\boldsymbol{x}}$ must be negative. Furthermore from the third equation we can solve $\Pi_P=\delta F/\delta r=-G(g)-(\Sigma+\gamma_P\kappa_g+g\boldsymbol{\nu}\cdot\hat{\boldsymbol{x}})$. Therefore, we know $-(\Sigma+\gamma_P\kappa_g+g\boldsymbol{\nu}\cdot\hat{\boldsymbol{x}})$, which comes from $\delta\int\left(\gamma_P^{(2)}-\Sigma y^{(2)}\cos\varphi^{(2)}\right)\mathrm{d}s^{(2)}$, actually induces an resistance against pore growth by increasing the system energy. We conclude that a sharp interface between domains is required to promote the pore growth.

5.2.4 Pore in a gradient transition zone between two domains: numerical solution

In the previous section we proved a gradient boundary produces an energy increase during a differential pore growth process. Here we aim to fully compute the energy barrier numerically for pore growth in gradient boundary. Under the same energetic setup as the

previous section, we employ the non-dimensionalization: $\bar{s}^{(i)} = \Sigma s^{(i)}/\gamma_{L-P}$, $\bar{y}^{(i)} = \Sigma y^{(i)}/\gamma_{L-P}$, $\bar{g} = g/\Sigma$, $\bar{\lambda} = \lambda\Sigma$. Under such a setup, the shape of the pore edge inside the gradient zone would follow the integral equation below:

$$\frac{\mathrm{d}\phi^{(2)}}{\mathrm{d}\bar{s}^{(2)}} = -\frac{1 + G(g) + g\sin\phi}{1 + \bar{g}\int_0^{\bar{s}^{(2)}} \cos\varphi^{(2)}(\bar{s})\,\mathrm{d}\bar{s}}$$

While in the inclusion/lipid phase domains, the pore shapes are still circular arcs following the Young-Laplace equations, and thus effective provide the boundary conditions for the pore shape in the gradient zone on its two ends: (assuming the total pore-edge arclength in the gradient zone was $\bar{S}$)

$$\bar{y}^{(2)}(0) = \cos\varphi\,(0)$$

$$\bar{y}^{(2)}(S) = \frac{\gamma_{I-P}}{\gamma_{L-P}}\cos\varphi\,(S)$$

Note that the pore can potentially adopt a lopsided profile with the pore edge not reaching the inclusion phase but terminating inside the gradient zone (**Fig. 5.5a**). Such solution can emerge when the cross-domain profile becomes energetically unfavorable/inadmissible. The problem is solved with shooting method by considering both possible profiles, and the one with lower energy is selected if they both exist.

5.2.5 Coarse-grained MD simulation

We performed MD simulation with the one-bead coarse-grained lipid model(174) in LAMMPS(175) to validate the above theoretical conclusions. Here we adopt the one-bead lipid model originally developed in Ref (174). Its details were briefly summarized here. In this model, all lipid particles were assumed to be axisymmetric. For two particles, denoted by i and j as shown in **Fig. 5.3**, their interaction potential consists of two functions, $E(r)$

and $\phi(\hat{\mathbf{r}}_{ij}, \mathbf{n}_i, \mathbf{n}_j)$, each describing the distance and the orientation dependencies of the potential. The formula for the potential were given by the equations below:

$$a = (\mathbf{n}_i \times \hat{\mathbf{r}}_{ij}) \cdot (\mathbf{n}_j \times \hat{\mathbf{r}}_{ij}) + \sin\theta_0 (\mathbf{n}_j - \mathbf{n}_i) \cdot \hat{\mathbf{r}}_{ij} - \sin^2\theta_0$$

$$\phi = 1 + \mu(a(\hat{\mathbf{r}}_{ij}, \mathbf{n}_i, \mathbf{n}_j) - 1)$$

$$U(\mathbf{r}_{ij}, \mathbf{n}_i, \mathbf{n}_j) = \begin{cases} \epsilon\left[\left(\frac{r_{\min}}{r}\right)^4 - 2\left(\frac{r_{\min}}{r}\right)^2\right] + [1 - \phi(\hat{\mathbf{r}}_{ij}, \mathbf{n}_i, \mathbf{n}_j)]\epsilon, & r < r_{\min} \\ -\epsilon\cos^{2\zeta}\left[\frac{\pi}{2}\frac{(r - r_{\min})}{(r_c - r_{\min})}\right]\phi(\hat{\mathbf{r}}_{ij}, \mathbf{n}_i, \mathbf{n}_j), & r_{\min} < r < r_c \end{cases}$$

Here the angle θ_0 characterizes the spontaneous curvature and the system has lowest orientational energy when $\theta_i = \theta_j = \theta_0$. ϵ controls the interaction intensity between particles. In our simulations we used LJ units where the length unit is σ and time unit is τ, and set $\mu = 3$, $\zeta = 5$, $r_{\min}/\sigma = \sqrt[6]{2}$, $r_c/\sigma = 2.6$ and $k_BT/\epsilon_{L-L} = 0.11$, $\epsilon_{I-I}/\epsilon_{L-L} = 1$, $\theta_{0,L-L} = \theta_{0,L-I} = 0$. Note under this set of parameters we can ensure that all particles were in the fluid phase.

We constructed a planar patch with an aggregated inclusion domain with 10159 lipid particles and 1941 inclusion particles. Periodic boundary conditions were applied on all sides. In LAMMPS we used the LJ units with length unit σ and time unit τ. We tuned two parameters: the cohesion intensity between the inclusion and the lipid particles $\epsilon_{\mathrm{I-L}}$, and the equilibrium angle between inclusion particles $\sin\theta_0$. We set $\epsilon_{\mathrm{L-L}} = \epsilon_{\mathrm{I-I}}$, so the inclusion-inclusion interaction was the same as the lipid-lipid interaction. Smaller the $\epsilon_{\mathrm{I-L}}/\epsilon_{\mathrm{L-L}}$, larger the line tension. Besides, $\sin\theta_0$ could be approximately associated with the intrinsic curvature: $c_0 \sim 2\sin\theta_0/d_0$, where d_0 is the inter-particle spacing. Note that the lipid matrix was set as curvature-free.

The following procedures are similar to those in Ref(176), and the schematics are

shown in **Fig. 5.6a**. After an initial relaxation under a low tension, we created an artificial radial force field in the center of the membrane to produce a pore of controlled radius. At the same time, the entire system was expanded accordingly with no area strain in the patch. At different pore radii, we removed the force field with the box boundary fixed and relaxed the system under an NVT ensemble to record the membrane tension Σ and observe whether the pore closes spontaneously. Hereby we measured the critical tensions Σ_{cr} for pore development. In our simulation procedures, the initial relaxation processes took $5.5 \times 10^4\tau$, while the artificial pore expansion/area straining processes took $2.5 \times 10^5\tau$ to produce a pore of 20σ in radius (but the membrane could fail before the straining processes were completed). And the final NVT relaxation processes at each pore radius took $5 \times 10^4\tau$. The timestep for all simulations was 0.005τ.

Additionally, on a pristine membrane we extracted its bending modulus and pore-edge line tension so we could non-dimensionalize the intrinsic curvature: $\bar{c}_0 = c_0\kappa_b/\gamma_{L-P}$. To obtain the membrane bending modulus, we characterized its fluctuation spectrum. Given a profile function $h(x, y)$ of the planar square membrane patch with side length L, its Fourier transform

$$h(q) = \frac{1}{L}\sum_n h(\boldsymbol{r})\exp\left(i\boldsymbol{q}\cdot\boldsymbol{r}\right)$$

where the wave vector $\boldsymbol{q} = 2\pi(n_x, n_y)/L$ and the wavenumber q is the norm of wave vector $\boldsymbol{q}$. Following Ref(177), the bending rigidity κ_b and the membrane tension Σ for the membrane patch in a periodic domain can be approximated by the following formula

$$\langle|h(q)|^2\rangle = \frac{k_{\mathrm{B}}T}{L^2(\kappa q^4 + \Sigma \mathrm{q}^2)}$$

In this study, we generate a large membrane patch in a periodic domain with size

$L{\sim}100\sigma$. The particle number is N=12100 and the time step size is $\Delta t = 0.005\tau$. The total steps for simulation are 5×10^7 and we dump the trajectories of the membrane every 1000 time steps. After running $5 \times 10^4\tau$ for equilibrium, the rest $2 \times 10^5\tau$ simulation trajectories were used for the fluctuation analysis. We calculate the values of fluctuation spectra by two-dimensional Fourier transform in Python and the membrane bending rigidity κ_b can be obtained by fitting the measured fluctuation spectrum between $0.1 \leq q \leq 0.5$ according to above equation (174, 177, 178). Here the bending rigidity is $\kappa_b \approx 31k_{\mathrm{B}}T$. Also judging from how well a q^{-4} term can fit the spectrum $h(q)$, we could find a tension-free state of the membrane, which gives $d_0/\sigma = 0.928$.

Then for the pore-edge line tension, we used the same procedure of pore creation and NVT relaxation as described above on a pristine lipid membrane. We recorded the radius of pore $\bar{R}$ under different relative increase of system area, and then used the equations given in Ref(176) and listed below to fit for the lipid-pore edge line tension under the adopted parameter set in the previous section. The corresponding line tension was $\gamma_{L-P} = 12k_BT/\sigma$.

$$R_{\min} = 2\left(\frac{\Delta A}{3\pi}\right)^{1/2}\cos\frac{\alpha}{3}$$

$$\cos\alpha = -\frac{\gamma}{2K_A}\frac{A_0}{\pi}\left(\frac{\Delta A}{3\pi}\right)^{-3/2}$$

$$F(r) = 2\pi\gamma r + \frac{K_A}{2A_0}(\Delta A - \pi r^2)^2$$

$$\bar{R} = \begin{cases} R_{\min}, & \text{if } F(R_{\min}) < F(0) \\ 0, & \text{otherwise} \end{cases}$$

Above K_A is the area modulus of the membrane, which could also be fitted with the stress-

strain curve.

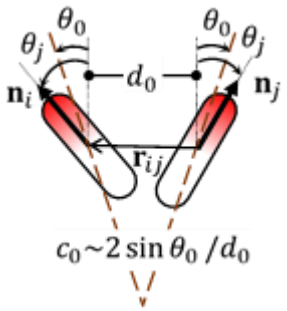

Figure 5.3. Schematics of the one-bead lipid molecule, where $\mathbf{n}_i$ and $\mathbf{n}_j$ each denotes the orientation of the corresponding particle, and $\mathbf{r}_{ij}$ is the distance vector from j to i. The angle θ_0 characterizes the spontaneous curvature and the system has lowest orientational energy when $\theta_i = \theta_j = \theta_0$.

5.3 Results

5.3.1 Axisymmetric pore in an inclusion with intrinsic curvature

Two parameters may play important roles in the system: $\bar{c}_0 = c_0\kappa_b/\gamma_{L-P}$, the ratio between the bending energy and the pore-edge line tension, and $\bar{R}_I = R_I\gamma_{L-P}/\kappa_b$, the size of the inclusion. The energy barriers normalized by $\pi\gamma_{L-P}^2/\Sigma$ under different $\bar{c}_0$ and $\bar{R}_I$ are shown in **Fig. 5.4b**. We can conclude that the energy barrier will be reduced for any non-zero $\bar{c}_0$ and $\bar{R}_I$, and the larger they are, the lower the barrier. But if both are too large, they will trigger a budding process without the pore (e.g. the $\bar{c}_0 = 0.9$ and 1). The drop of barrier is significant only when $\bar{c}_0$'s order is above 0.1 and therefore the bending energy is of the same order as the pore-edge line tension. We can establish a characteristic length order on the inclusion's intrinsic radius of curvature, below which the curvature can play a crucial role in pore growth. If we take(177, 179-181) $\kappa_b \sim 10^{-19}$J and $\gamma_{L-P} \sim 5 \times 10^{-12}$J/m, $\bar{c}_0 \sim (0.1,1)$ will give a radius of approximately between 40nm and 400nm. Also note that

the bending modulus of membrane under high curvature can be larger than that of a flat membrane, and therefore this length scale could also be larger. As $\bar{R}_I$ grows towards 10 the barrier drop gradually saturates and is determined purely by the value of $\bar{c}_0$. This suggests that $\bar{c}_0$ could be the leading design parameter for engineering the rupture process through inclusion curvature. Another observation is the approximate linear scaling between barrier drop and $\bar{c}_0$, implying an exponential growth in rupture rate(180) with $\bar{c}_0$.

Some energy variations with the pore radius are shown in **Fig. 5.4c-d**, with typical membrane shapes plotted accordingly in **Fig. 5.4e-f**. First, the bending energy stored in the membrane is relieved remarkably as the pore expands even at large pore radius, reducing the energy barrier. Additionally, when the inclusion is small (**Fig. 5.4c** and **5.4e**) and thus the curvature around its center is relatively high, the membrane will adopt flatter shape as pore grows and thus induce more work on surface tension. This could also be understood as following: when a pore expands on a spherical surface, the ratio between its enclosed spherical area to its circumference will increase as the curvature increases. Yet on larger inclusion (**Fig. 5.4d** and **5.4f**) with lower curvature at center, this mechanism becomes suppressed. Here we assumed that the pore develops from the center, a region with the lowest curvature in the entire inclusion, but it can also develop near the interface where the highest curvature tends to reside. Therefore, the tensional work can be more influential than predicted above.

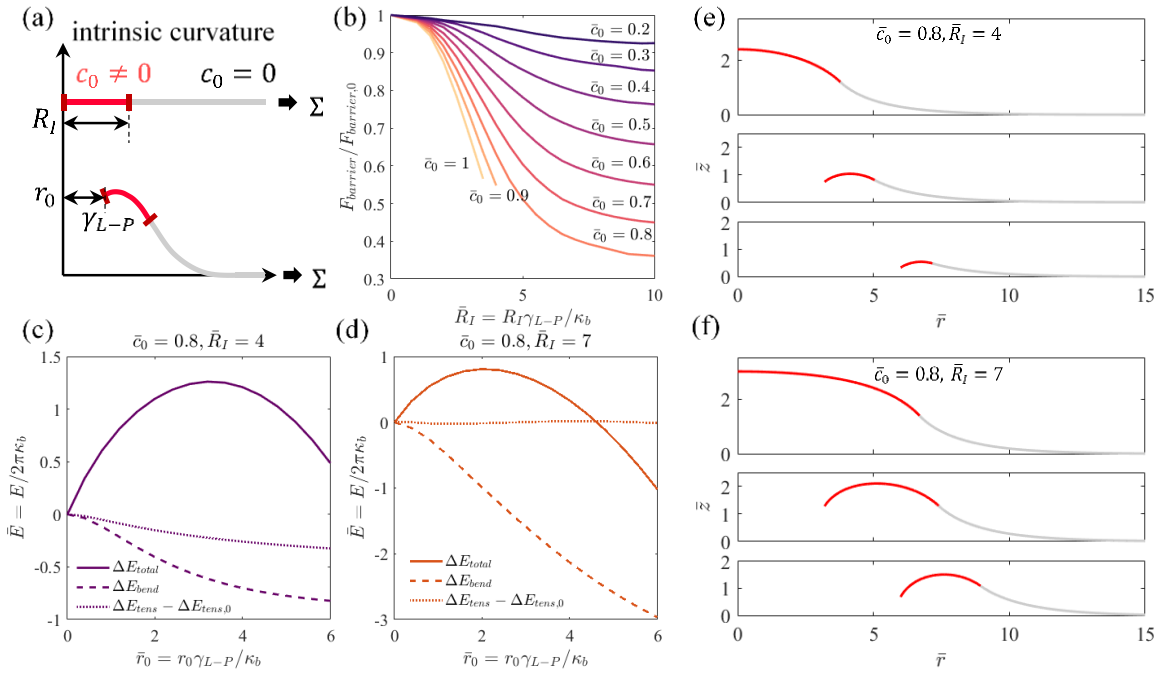

Figure 5.4. Intrinsic curvature reduces pore growth energy barrier. (a) schematics of the continuum problem setup. (b) the energy barrier relative to the pristine case under various intrinsic curvatures and inclusion sizes. (c-d) membrane energy variations as the pore radius increased with $\bar{c}_0 = 0.8$ for (c) $\bar{R}_I = 4$ and (d) $\bar{R}_I = 7$, with (e-f) associated example membrane shapes under different pore radius. The inclusion was marked in red and the matrix in gray. Here we take $\Sigma\kappa_b/\gamma_{L-P}^2 = 0.25$ and $\kappa_G/\kappa_b = -0.9$(172, 173)

5.3.2 Pore in a gradient transition zone: numerical result

The energy barrier for the numerical solution, normalized by that of a pristine membrane, is shown in **Fig. 5.5b**. Note here we took $G(g) = \lambda g$ so $\int_0^L G(g)\mathrm{d}x = 0.5\lambda\gamma_{L-P}$ so effectively the "inter-domain line tension" is equal to $0.5\lambda\gamma_{L-P}$ if the setup is represented by a sharp-interface formula. We chose a linear form of $G(g)$ so the effective line tension is constant regardless the value of g. It can be immediately noticed that higher g yields a lower energy barrier from a cross-domain pore solution. In comparison, lower g tends to yield a lopsided solution with relatively higher barrier. Also generally high λ

produces lower barrier, consistent with our intuition and results in sharp-interface solution. Such observation further proves the pore-repelling nature of a smooth and mild transition boundary between phases.

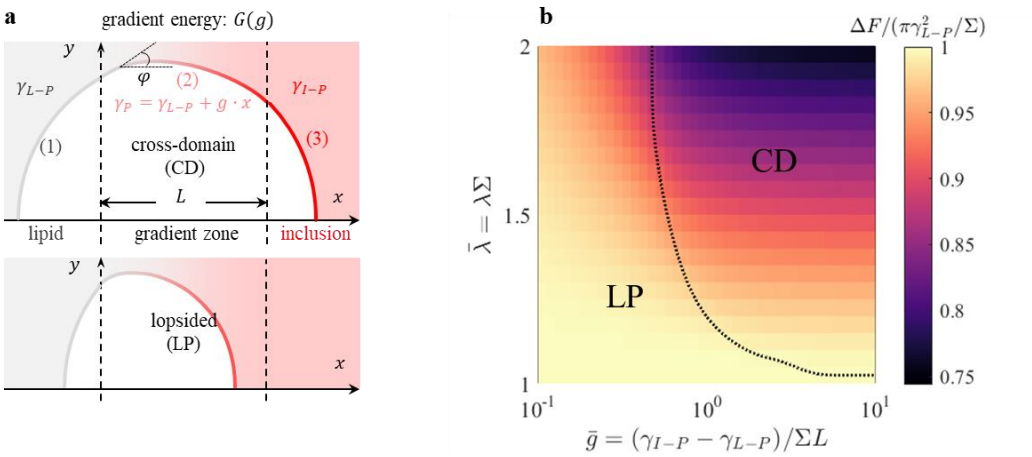

Figure 5.5. Pore growth on a gradient transition boundary between the lipid phase and the inclusion phase. (a) Two types of solution can exist: the cross-domain (CD) solution with pore spanning from one phase to another (top), and the lopsided (LP) solution with pore edge terminated inside the transition boundary. (b) The energy barrier normalized by that of a pristine membrane. The black dotted line separates the regime where the cross-domain or lopsided solution has lower energy. Here we chose $gL/\gamma_{L-P} = 0.5$ and $G(g) = \lambda|g|$.

5.3.3 MD simulation of pore growth with an inclusion domain

The measured critical tensions, normalized by that without inclusion $\Sigma_{\mathrm{cr},0}$, are shown in **Fig. 5.6b**. We come to an immediate conclusion that any positive line tension and intrinsic curvature reduces the critical tension. Specifically, the curvature plays a critical role in the characteristic range $\bar{c}_0 \sim (0,1)$. Note if we assume the energy barrier a membrane can overcome is constant, then the critical tension here is approximately proportional to the energy barrier for pore growth in a constant-tension setup as in previous sections (see

SI for details). Membrane screenshots at the critical frame when the pore developed are shown in **Fig. 5.6c**. Here pores prefer to form on the interface between two domains regardless the value of $\bar{c}_0$, suggesting a concomitant contribution from both the interface and the curvature. Additionally, with a low $\bar{c}_0$, the pore and the inclusion could exist stably inside the membrane under NVT ensemble (e.g. $\bar{c}_0 = 0.35$ in **Fig. 5.6c**). In comparison if $\bar{c}_0$ was high (e.g. $\bar{c}_0 = 0.70$ in **Fig. 5.6c**), the pore development process eventually led to the budding out of the inclusion and left behind a fission pore. But note that without a pore above certain radius the budding would not occur, thus it is still a consequence of the pore development process. Also, we measured the work of rupture defined as $W_{\bar{\Sigma}=0.25} = A\int_{\epsilon_{\bar{\Sigma}=0.25}}^{\epsilon_{cr}} \Sigma \mathrm{d}\epsilon$. Here $\epsilon_{\bar{\Sigma}=0.25}$ is the areal strain at tension $\bar{\Sigma} = 0.25$ while ϵ_{cr} is the rupture strain. This work can be regarded as the energy barrier defined on a path with areal strain as the reaction coordinate between the intact and the perforated state. Again, we observed that both curvature and inter-domain line tension can reduce it (**Fig. 5.6d**). These observations imply the fragile nature of membrane with a highly curved inclusion and validate our previous theoretical predictions.

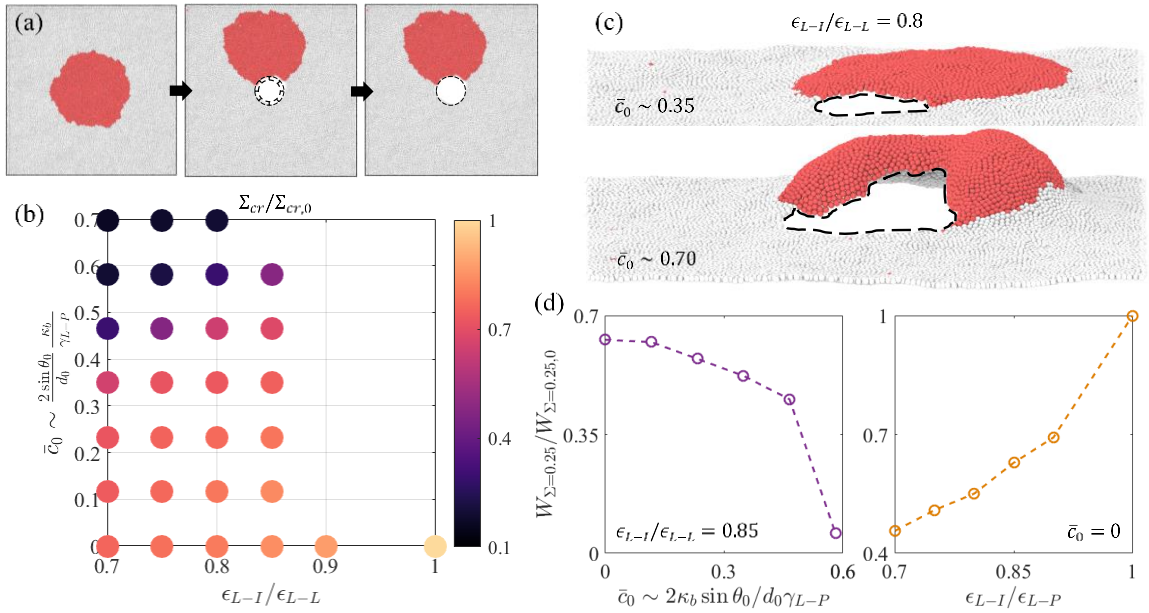

Figure 5.6. CGMD simulation of pore growth in the presence of an inclusion domain. (a) Schematic for the system setup of the MD simulation. (b) the critical tension normalized by that of a pristine membrane. The inclusion failed to aggregate into a single stable domain in the region without data. (c) two example membrane configurations at the critical moment of pore development. The edges of the pore were marked with black dashed lines. For the $\bar{c}_0 \sim 0.70$ case the inclusion would proceed to bud out and leave behind a large pore in the membrane. (d) example work of rupture normalized by that of a pristine membrane.

5.4 Discussion

Above we showed two potential mechanisms how the aggregation can contribute to rupture observed in Ref (40, 41). But there are several other points to be noted in our theoretical modeling. In Ref (165-167) the researchers studied the rupturing efficacy of an AH peptide. In general, they recorded more rupture in shorter time on smaller vesicles with radii near or below the order of 100nm. And for radii above 400nm no rupture was observed. Here we also reach the conclusion that larger curvature yields lower barrier, and the characteristic length scale we obtained for radius of curvature is approximately 80nm, also

comparable with the vesicle radii in their experiments. However, for simplicity we only worked with an infinite membrane patch. To fully capture the phenomenon on the cells or the GUVs used in experiments, a vesicle could be the more realistic setup and calls for further investigation. Besides, we observed that if both c_0 and R_I are too large, a budding process can be initiated. That can effectively serve as a lipid extraction, and may also rupture the membrane as suggested in Ref (159). Finally, as the pores always develop at the locations with lowest energy barrier, barriers computed above models can be regarded as upper bounds for the actual situations whose barriers can be even lower.

Here we pointed out the potential importance of domain aggregation on the membrane mechanical integrity. Specifically, for curvature there exist single important parameter $\bar{c}_0 = c_0\kappa_b/\gamma_{L-P}$, the ratio between the bending energy and pore-edge line tension. To increase this parameter, agents should exhibit an affinity to enter membrane yet also a trans-leaflet barrier so it can distribute asymmetrically between leaflets and thus introduce curvature. To induce the aggregation, various mechanisms can be employed such as the l_o/l_d phase separation(182), spinodal decomposition-like domain segregation(183) or the curvature-induced aggregation(183, 184). To study such parameter and mechanisms, simulations can play a pivotal role in future study to provide the necessary information on the lipid-agent interaction to be incorporated by both theoretical analysis and agent design.

5.5 Conclusions

In summary, we first derived a general framework on the energy variation of membrane with an inclusion under an infinitesimal pore growth. We combined both

theories and simulations to illustrate that the energy barrier for rupture can be significantly alleviated through interfaces and curvatures. In our theories, we showed that to induce such effect the inclusion should be large enough while possessing a sharp interface and a non-trivial intrinsic curvature. We noticed that when the intrinsic curvature reaches a certain range ($\bar{c}_0 \sim (0.1,1)$) the energy barrier could drop significantly due to the relief of strain energy, approximately linearly with $\bar{c}_0$. Such conclusions suggest that designing the external agents to introduce domain interfaces and curvatures could be an effective approach to engineer the rupture process and can lay a foundation for future membrane-active agent design.

Chapter 6

Conclusions and Perspectives

6.1 Concluding remarks

By employing both theories and numerical simulations and supplemented by experimental observations, we studied the mechanical behaviors, including pre-straining, elasticity, active contractility, remodeling and damaging, of biological tissues and materials at various scales. Below we summarize the scientific findings of each chapter.

In Chapter 2, a pre-straining is discovered inside the natural epicardial layer on porcine ventricle. By placing tracers on epicardium samples at multiple locations and tracking their displacements upon dissection from the ventricle we generate a mapping of pre-strains on the surface of epicardium. Such mapping and biaxial tension test data are incorporated into a finite element model of porcine left ventricle. We find that the ventricular cavity volume together with the volume averaged first principle myocardial stress will be significantly decreased under a pre-strained epicardium, yet in comparison the model with non pre-strained epicardial layer shows little difference from the model without epicardial layer at all. Such comparison points out the importance of pre-straining in both future modeling and medical device design for ventricular system.

In Chapter 3, we perform finite element modeling to reveal the importance of pre-straining to mechanically support infarct ventricle with elastic epicardial patch as demonstrated by ventricle stroke volume and the cavity dilatation, both of which show

strong sensitivity to the pre-straining of the patch. We further propose a viscoelastic material design for the patch where the static stiffness is replaced by the dynamic stiffness in order to avoid the complexity of tuning pre-strain, and identify an optimal choice for the dynamic moduli which is satisfied on gel point. Under such design the effective pre-straining will be adaptively determined by the ventricular beating and the only parameter to tune is the storage modulus. A starch-gel based material is then fabricated in accordance with the simulation-guided design and deployed in animal test of both acute and sub-acute myocardial infarction treatment. The therapeutic efficacies in experiments confirm the optimality of the material parameters, in comparisons with materials of different viscoelastic traits, and thereby justify our prediction. The principle of utilizing viscoelasticity instead of static elasticity elucidated in this chapter can be extrapolated to the design of materials that provide mechanical support for many other dynamically loaded systems.

In Chapter 4, the microstructure and the deformation mechanism of limpet teeth is characterized through high resolution microscopic imaging and digital image correlation. We discover the auxeticity on the leading edge of the teeth, and reveal its correlation with the underlying spin pattern, which is a consequence of the microstructure in the orientation of goethite nanorods. Inspired by the revolving orientational pattern, we construct a representative structural element that aims to mimic the deformation mechanism observed in the experiment images by homogenizing the nanorod-matrix complex into an anisotropic material. The structural element is shown to possess micropolar elasticity instead of the conventional elasticity, which is strongly correlated with its auxeticity. The observed microstructure achieves auxeticity by tuning its local material orientation, and without the

presence of voids, a constituent considered necessary in most of engineered auxetic materials and structure, and thus avoids the potential drawback of low strength.

In Chapter 5, a general theoretical framework is first established to study the pore growth on liquid membrane in the presence of an aggregated inclusion domain, where we discover the driving force from bending energy density and inter-domain line tension on promoting the pore growth. We also prove mathematically that a smooth gradient boundary between domains produces higher energy barrier for pore growth than a sharp interface. Numerical solutions are given on both the axisymmetric pore growing on the inclusion center and the pore growing on a gradient boundary, which confirm the theory. Specifically, a characteristic range of inclusion intrinsic curvature is revealed which leads to significant energy barrier drop for pore growth, and shows consistency with previous experimental results. We also perform a coarse-grained molecular dynamics simulation that verifies the theoretical predictions by showing a reduced critical membrane tension and work of rupture for pore development when the membrane has an inclusion with intrinsic curvature and inter-domain line tension.

6.2 Outlook of future research

As discussed in current thesis and many other studies, mechanics plays an essential role in understanding the behaviors of biological bodies and developing future biomedical technology. But in this thesis the connection between the mechanical behaviors and the underlying biological signals and processes is still limited and has a highly coarse-grained nature. Knowledge of the interplay between different physical dynamics across different scales inside the active biological bodies is still insufficient, and many interesting questions

remain open, some of which are listed below.

(1) Extensive studies and investigation have been performed to model the stress, passive or active, as the major mechanical cue inside both healthy and infarct ventricle, yet how it exactly participates in the recovering or deteriorating process of the myocardium is unknown. The muscle tissue is known to require mechanical stimulus for growth, yet an excessive stress can always lead to material failure. And thus it is of great interests to understand whether the myocardium expects an optimal stress or strain under various physiological conditions on both the continuum and the cellular level. The differentiation between active and passive stress can also be vital.

(2) The structure, such as the microstructure in limpet teeth, and the mechanical interaction, such as the epicardial pre-straining in porcine ventricle, of the various components inside biological bodies can be the outcome of an optimal design. But it is also a natural result of its growth process. Therefore how the active growth leads to the observed system can provide critical insight for tissue physiology and development, and derive novel fabrication principle for engineering system. This dynamic process is intrinsically multi-physical, and requires expertise in mechanics, chemistry, physics and biology.

(3) The active response of cells with respect to the external mechanical stimulus is still under-represented in current biomechanics studies. For example, when under the infarction, whether the myocardium and myocyte will produce active mechanical remedy against the disease deterioration can be an interesting question. And when the cell membrane has a degraded mechanical integrity, will the cells initiate certain self-protection mechanism to maintain their viability? If so, does it mean that a threshold level of mechanical damage exists below which cells can survive? Following this line there is a series of open questions

to be explored.

(4) In Chapter 3 we consider the remodeling of myocardium through its lengthening and the induced cavity dilatation. Yet from the viewpoint of pathology, another important degrading process is the cell fibrosis and death, which is the true reason of the stiffening and the thinning of ventricular wall behind the simplified assumption we made in our modeling. It can be of great interests to incorporate those processes into the model and observe how they interact with the mechanical processes.

(5) In Chapter 4 we demonstrate the auxeticity of limpet teeth together with its microstructure. But the it is still unclear how the microstructure interact with the crack. Apart from the absence of voids, does the microstructure provide certain protection mechanism against mechanical failure? How is the spin-dominated deformation mechanism we observed involved in the fracture process?

(6) In Chapter 5 the pore growth process is considered and investigated through the minimization of free energy, and thus regarded as a quasi-static process. But for cell membrane it has a highly kinetic nature with a large number of out-of-equilibrium processes in progress. Thus developing a kinetic theory for the pore growth can be important. Potential kinetics include the transport of lipid molecules between the membrane and the intracellular reservoir which can tune the membrane tension, transport of curvature-inducing agents between the leaflets which can tune the membrane bending energy density, and the thermal fluctuation of the membrane itself, including both the out-of-plane displacement and the local heterogeneity distribution. These physical aspects combined together will provide a more comprehensive description of the membrane degradation process and its potential influence on the biological activities of cells.

(7) In Chapter 5 only a theoretical treatment is given on the potential mechanical damage from an aggregated domain on liquid membrane. Yet how to utilize the theoretical principle and engineer the molecular agents to achieve the expected outcome is still an open question. One potential solution can be combining the theories, full-atom simulations, experiments and possibly artificial intelligence to establish a new generation of drug discovery protocol, which can be a major scientific and technological challenge for the future.

Bibliography

1. Taber LA & Humphrey JD (2001) Stress-modulated growth, residual stress, and vascular heterogeneity. *J Biomech Eng-T Asme* 123(6):528-535.
2. Genet M*, et al.* (2015) Heterogeneous growth-induced prestrain in the heart. *J Biomech* 48(10):2080-2089.
3. Fung YCB (1967) Elasticity of Soft Tissues in Simple Elongation. *Am J Physiol* 213(6):1532-+.
4. Pinto JG & Fung Y (1973) Mechanical properties of the heart muscle in the passive state. *J Biomech* 6(6):597-616.
5. Costa KD, Holmes JW, & McCulloch AD (2001) Modelling cardiac mechanical properties in three dimensions. *Philos T R Soc A* 359(1783):1233-1250.
6. Holzapfel GA & Ogden RW (2009) Constitutive modelling of passive myocardium: a structurally based framework for material characterization. *Philos T R Soc A* 367(1902):3445-3475.
7. Rausch MK & Kuhl E (2013) On the effect of prestrain and residual stress in thin biological membranes. *J Mech Phys Solids* 61(9):1955-1969.
8. Krishnamurthy G*, et al.* (2008) Material properties of the ovine mitral valve anterior leaflet in vivo from inverse finite element analysis. *Am J Physiol-Heart C* 295(3):H1141-H1149.
9. Fung YC & Liu SQ (1989) Change of Residual Strains in Arteries Due to Hypertrophy Caused by Aortic Constriction. *Circ Res* 65(5):1340-1349.
10. Fung YC (1991) What Are the Residual-Stresses Doing in Our Blood-Vessels. *Ann Biomed Eng* 19(3):237-249.
11. Omens JH & Fung YC (1990) Residual Strain in Rat Left-Ventricle. *Circ Res* 66(1):37-45.
12. Shi XD*, et al.* (2019) Epicardial prestrained confinement and residual stresses: a newly observed heart ventricle confinement interface. *J R Soc Interface* 16(152).
13. Morel V, Mercay A, & Quinn TM (2005) Prestrain decreases cartilage susceptibility to injury by ramp compression in vitro. *Osteoarthr Cartilage* 13(11):964-970.
14. Halonen KS*, et al.* (2016) Optimal graft stiffness and pre-strain restore normal joint motion and cartilage responses in ACL reconstructed knee. *J Biomech* 49(13):2566-2576.
15. Mesfar W & Shirazi-Adl A (2006) Biomechanics of changes in ACL and PCL material properties or prestrains in flexion under muscle force-implications in ligament reconstruction. *Computer methods in biomechanics and biomedical engineering* 9(4):201-209.
16. Lin X*, et al.* (2019) A viscoelastic adhesive epicardial patch for treating myocardial infarction. *Nat Biomed Eng* 3(8):632-643.
17. Gao HJ, Ji BH, Jager IL, Arzt E, & Fratzl P (2003) Materials become insensitive to flaws at nanoscale: Lessons from nature. *P Natl Acad Sci USA* 100(10):5597-5600.
18. Ji BH & Gao HJ (2004) Mechanical properties of nanostructure of biological materials. *J Mech Phys Solids* 52(9):1963-1990.
19. Fratzl P, Burgert I, & Gupta HS (2004) On the role of interface polymers for the

mechanics of natural polymeric composites. *Phys Chem Chem Phys* 6(24):5575-5579.
20. Zhang ZQ, Zhang YW, & Gao HJ (2011) On optimal hierarchy of load-bearing biological materials. *P Roy Soc B-Biol Sci* 278(1705):519-525.
21. Jager I & Fratzl P (2000) Mineralized collagen fibrils: A mechanical model with a staggered arrangement of mineral particles. *Biophys J* 79(4):1737-1746.
22. Rho JY, Kuhn-Spearing L, & Zioupos P (1998) Mechanical properties and the hierarchical structure of bone. *Med Eng Phys* 20(2):92-102.
23. Puxkandl R*, et al.* (2002) Viscoelastic properties of collagen: synchrotron radiation investigations and structural model. *Philos T R Soc B* 357(1418):191-197.
24. Menig R, Meyers MH, Meyers MA, & Vecchio KS (2001) Quasi-static and dynamic mechanical response of Strombus gigas (conch) shells. *Mat Sci Eng a-Struct* 297(1-2):203-211.
25. Yao HM*, et al.* (2010) Protection mechanisms of the iron-plated armor of a deep-sea hydrothermal vent gastropod. *P Natl Acad Sci USA* 107(3):987-992.
26. Yin S*, et al.* (2019) Hyperelastic phase-field fracture mechanics modeling of the toughening induced by Bouligand structures in natural materials. *J Mech Phys Solids* 131:204-220.
27. Barber AH, Lu D, & Pugno NM (2015) Extreme strength observed in limpet teeth. *J R Soc Interface* 12(105).
28. Li YQ, Yu T, Yang TY, Zheng LX, & Liao K (2012) Bio-Inspired Nacre-like Composite Films Based on Graphene with Superior Mechanical, Electrical, and Biocompatible Properties. *Adv Mater* 24(25):3426-3431.
29. Dimas LS, Bratzel GH, Eylon I, & Buehler MJ (2013) Tough Composites Inspired by Mineralized Natural Materials: Computation, 3D printing, and Testing. *Adv Funct Mater* 23(36):4629-4638.
30. Podsiadlo P*, et al.* (2005) Layer-by-layer assembly of nacre-like nanostructured composites with antimicrobial properties. *Langmuir* 21(25):11915-11921.
31. Martin JJ, Fiore BE, & Erb RM (2015) Designing bioinspired composite reinforcement architectures via 3D magnetic printing. *Nat Commun* 6.
32. Hawkey PM (2008) Pre-clinical experience with daptomycin. *J Antimicrob Chemoth* 62:7-14.
33. Zhanel GG*, et al.* (2010) New Lipoglycopeptides A Comparative Review of Dalbavancin, Oritavancin and Telavancin. *Drugs* 70(7):859-886.
34. Belley A*, et al.* (2009) Oritavancin Kills Stationary-Phase and Biofilm Staphylococcus aureus Cells In Vitro. *Antimicrob Agents Ch* 53(3):918-925.
35. Straus SK & Hancock REW (2006) Mode of action of the new antibiotic for Gram-positive pathogens daptomycin: Comparison with cationic antimicrobial peptides and lipopeptides. *Bba-Biomembranes* 1758(9):1215-1223.
36. Domenech O*, et al.* (2009) Interactions of oritavancin, a new lipoglycopeptide derived from vancomycin, with phospholipid bilayers: Effect on membrane permeability and nanoscale lipid membrane organization. *Bba-Biomembranes* 1788(9):1832-1840.
37. Zhang LJ, Dhillon P, Yan H, Farmer S, & Hancock REW (2000) Interactions of bacterial cationic peptide antibiotics with outer and cytoplasmic membranes of Pseudomonas aeruginosa. *Antimicrob Agents Ch* 44(12):3317-3321.
38. Chen YF, Sun TL, Sun Y, & Huang HW (2014) Interaction of Daptomycin with Lipid Bilayers: A Lipid Extracting Effect. *Biochemistry-Us* 53(33):5384-5392.

39. Hurdle JG, O'Neill AJ, Chopra I, & Lee RE (2011) Targeting bacterial membrane function: an underexploited mechanism for treating persistent infections. *Nat Rev Microbiol* 9(1):62-75.
40. Kim W*, et al.* (2018) Discovery and Optimization of nTZDpa as an Antibiotic Effective Against Bacterial Persisters. *Acs Infect Dis* 4(11):1540-1545.
41. Kim W*, et al.* (2019) A selective membrane-targeting repurposed antibiotic with activity against persistent methicillin-resistant Staphylococcus aureus. *P Natl Acad Sci USA* 116(33):16529-16534.
42. Benjamin EJ*, et al.* (2017) Heart Disease and Stroke Statistics-2017 Update: A Report From the American Heart Association. *Circulation* 135(10):e146-e603.
43. Raab W (1963) The Nonvascular Metabolic Myocardial Vulnerability Factor in "Coronary Heart Disease". Fundamentals of Pathogenesis, Treatment, and Prevention. *Am Heart J* 66:685-706.
44. Baroldi G (1973) Coronary heart disease: significance of the morphologic lesions. *Am Heart J* 85(1):1-5.
45. Baroldi G (1965) Acute coronary occlusion as a cause of myocardial infarct and sudden coronary heart death. *Am J Cardiol* 16(6):859-880.
46. Erhardt LR, Unge G, & Boman G (1976) Formation of coronary arterial thrombi in relation to onset of necrosis in acute myocardial infarction in man. A clinical and autoradiographic study. *Am Heart J* 91(5):592-598.
47. Reichenbach DD & Moss NS (1975) Myocardial cell necrosis and sudden death in humans. *Circulation* 52(6 Suppl):III60-62.
48. Silver MD, Anderson TW, Vand Dreumel AA, & Hutson RE (1973) Letter: Nutritional muscular dystrophy and human myocardial infarction. *Lancet* 2(7834):912-913.
49. Narula J*, et al.* (1996) Apoptosis in myocytes in end-stage heart failure. *N Engl J Med* 335(16):1182-1189.
50. Robin ED (1977) Special report: dysoxia. Abnormal tissue oxygen utilization. *Arch Intern Med* 137(7):905-910.
51. Cleutjens JP, Blankesteijn WM, Daemen MJ, & Smits JF (1999) The infarcted myocardium: simply dead tissue, or a lively target for therapeutic interventions. *Cardiovasc Res* 44(2):232-241.
52. De Celle T*, et al.* (2004) Long-term structural and functional consequences of cardiac ischaemia-reperfusion injury in vivo in mice. *Exp Physiol* 89(5):605-615.
53. Gaby AR (2010) Nutritional treatments for acute myocardial infarction. *Alternative medicine review : a journal of clinical therapeutic* 15(2):113-123.
54. Janicki JS, Brower GL, Gardner JD, Chancey AL, & Stewart JA, Jr. (2004) The dynamic interaction between matrix metalloproteinase activity and adverse myocardial remodeling. *Heart failure reviews* 9(1):33-42.
55. Spinale FG, Janicki JS, & Zile MR (2013) Membrane-associated matrix proteolysis and heart failure. *Circulation research* 112(1):195-208.
56. Tsuruda T, Costello-Boerrigter LC, & Burnett JC, Jr. (2004) Matrix metalloproteinases: pathways of induction by bioactive molecules. *Heart failure reviews* 9(1):53-61.
57. Katz AM (2006) *Physiology of the heart* (Lippincott Williams & Wilkins, Philadelphia) 4th Ed pp xix, 644 p.
58. Kwon MH, Cevasco M, Schmitto JD, & Chen FY (2012) Ventricular restraint therapy for heart failure: A review, summary of state of the art, and future directions. *J Thorac*

Cardiovasc Surg 144(4):771-777 e771.
59. Lee LS*, et al.* (2010) Ventricular restraint therapy for heart failure: the right ventricle is different from the left ventricle. *J Thorac Cardiovasc Surg* 139(4):1012-1018.
60. Naveed M*, et al.* (2018) The promising future of ventricular restraint therapy for the management of end-stage heart failure. *Biomed Pharmacother* 99:25-32.
61. Jöbsis PD*, et al.* (2007) The visceral pericardium: macromolecular structure and contribution to passive mechanical properties of the left ventricle. *American Journal of Physiology-Heart and Circulatory Physiology* 293(6):H3379-H3387.
62. Williams C & Black III LD (2015) The Role of Extracellular Matrix in Cardiac Development. *Biomaterials for Cardiac Regeneration*, (Springer), pp 1-35.
63. Farquharson C & Robins SP (1989) The distribution of elastin in developing and adult rat organs using immunocytochemical techniques. *Journal of anatomy* 165:225.
64. Fomovsky GM, Thomopoulos S, & Holmes JW (2010) Contribution of extracellular matrix to the mechanical properties of the heart. *J Mol Cell Cardiol* 48(3):490-496.
65. Borg T & Caulfield J (1981) The collagen matrix of the heart. *Federation proceedings*, pp 2037-2041.
66. Sussman MA, McCulloch A, & Borg TK (2002) Dance band on the titanic biomechanical signaling in cardiac hypertrophy. *Circulation research* 91(10):888-898.
67. Granzier HL & Irving TC (1995) Passive tension in cardiac muscle: contribution of collagen, titin, microtubules, and intermediate filaments. *Biophysical Journal* 68(3):1027-1044.
68. Kang T, Humphrey J, & Yin F (1996) Comparison of biaxial mechanical properties of excised endocardium and epicardium. *American Journal of Physiology-Heart and Circulatory Physiology* 270(6):H2169-H2176.
69. Kluge T & Hovig T (1967) The ultrastructure of human and rat pericardium. *Acta Pathologica Microbiologica Scandinavica* 71(4):547-563.
70. Chadwick R (1982) Mechanics of the left ventricle. *Biophysical journal* 39(3):279.
71. Fung Y (1991) What are the residual stresses doing in our blood vessels? *Annals of biomedical engineering* 19(3):237-249.
72. Omens JH & Fung Y-C (1990) Residual strain in rat left ventricle. *Circulation research* 66(1):37-45.
73. Genet M*, et al.* (2015) Heterogeneous growth-induced prestrain in the heart. *Journal of biomechanics* 48(10):2080-2089.
74. Eriksson TSE, Prassl AJ, Plank G, & Holzapfel GA (2013) Influence of myocardial fiber/sheet orientations on left ventricular mechanical contraction. *Math Mech Solids* 18(6):592-606.
75. Goktepe S, Acharya SNS, Wong J, & Kuhl E (2011) Computational modeling of passive myocardium. *Int J Numer Meth Bio* 27(1):1-12.
76. Streeter DD & Bassett DL (1966) An Engineering Analysis of Myocardial Fiber Orientation in Pigs Left Ventricle in Systole. *Anat Rec* 155(4):503-&.
77. Maas SA, Ellis BJ, Ateshian GA, & Weiss JA (2012) FEBio: Finite Elements for Biomechanics. *J Biomech Eng-T Asme* 134(1).
78. Amirhamzeh MMR*, et al.* (1996) Iatrogenic myocardial edema: Increased diastolic compliance and time course of resolution in vivo. *Ann Thorac Surg* 62(3):737-743.
79. Rane AA & Christman KL (2011) Biomaterials for the Treatment of Myocardial Infarction: A 5-Year Update. *Journal of the American College of Cardiology*

58(25):2615-2629.
80. Laflamme MA & Murry CE (2011) Heart regeneration. *Nature* 473:326.
81. Wei K*, et al.* (2015) Epicardial FSTL1 reconstitution regenerates the adult mammalian heart. *Nature* 525:479.
82. Shadrin IY*, et al.* (2017) Cardiopatch platform enables maturation and scale-up of human pluripotent stem cell-derived engineered heart tissues. *Nature Communications* 8:1825.
83. Fujimoto KL*, et al.* (2007) An Elastic, Biodegradable Cardiac Patch Induces Contractile Smooth Muscle and Improves Cardiac Remodeling and Function in Subacute Myocardial Infarction. *Journal of the American College of Cardiology* 49(23):2292-2300.
84. Didie M*, et al.* (2013) Parthenogenetic stem cells for tissue-engineered heart repair. *J Clin Invest* 123(3):1285-1298.
85. Liao S-Y*, et al.* (2010) Attenuation of Left Ventricular Adverse Remodeling With Epicardial Patching After Myocardial Infarction. *Journal of Cardiac Failure* 16(7):590-598.
86. Stuckey DJ*, et al.* (2010) Magnetic resonance imaging evaluation of remodeling by cardiac elastomeric tissue scaffold biomaterials in a rat model of myocardial infarction. *Tissue Eng Part A* 16(11):3395-3402.
87. Fujimoto KL*, et al.* (2012) Placement of an Elastic Biodegradable Cardiac Patch on a Subacute Infarcted Heart Leads to Cellularization With Early Developmental Cardiomyocyte Characteristics. *Journal of Cardiac Failure* 18(7):585-595.
88. Chi N-H, Yang M-C, Chung T-W, Chou N-K, & Wang S-S (2013) Cardiac repair using chitosan-hyaluronan/silk fibroin patches in a rat heart model with myocardial infarction. *Carbohydrate Polymers* 92(1):591-597.
89. Serpooshan V*, et al.* (2013) The effect of bioengineered acellular collagen patch on cardiac remodeling and ventricular function post myocardial infarction. *Biomaterials* 34(36):9048-9055.
90. Vilaeti AD*, et al.* (2013) Short-term ventricular restraint attenuates post-infarction remodeling in rats. *International Journal of Cardiology* 165(2):278-284.
91. D'Amore A*, et al.* (2016) Bi-layered polyurethane – Extracellular matrix cardiac patch improves ischemic ventricular wall remodeling in a rat model. *Biomaterials* 107:1-14.
92. Moainie SL*, et al.* (2002) Infarct restraint attenuates remodeling and reduces chronic ischemic mitral regurgitation after postero-lateral infarction. *The Annals of Thoracic Surgery* 74(2):444-449.
93. Fomovsky GM, Clark SA, Parker KM, Ailawadi G, & Holmes JW (2012) Anisotropic Reinforcement of Acute Anteroapical Infarcts Improves Pump Function. *Circulation: Heart Failure* 5(4):515-522.
94. Enomoto Y*, et al.* (2005) Early Ventricular Restraint After Myocardial Infarction: Extent of the Wrap Determines the Outcome of Remodeling. *The Annals of Thoracic Surgery* 79(3):881-887.
95. Clarke SA, Ghanta RK, Ailawadi G, & Holmes JW (2014) Cardiac Restraint and Support Following Myocardial Infarction. *Cardiovascular and Cardiac Therapeutic Devices*, ed Franz T (Springer Berlin Heidelberg, Berlin, Heidelberg), pp 169-206.
96. Clarke SA, Goodman NC, Ailawadi G, & Holmes JW (2015) Effect of Scar Compaction on the Therapeutic Efficacy of Anisotropic Reinforcement Following Myocardial

Infarction in the Dog. *Journal of Cardiovascular Translational Research* 8(6):353-361.
97. Piao H*, et al.* (2007) Effects of cardiac patches engineered with bone marrow-derived mononuclear cells and PGCL scaffolds in a rat myocardial infarction model. *Biomaterials* 28(4):641-649.
98. Sarig U*, et al.* (2016) Natural myocardial ECM patch drives cardiac progenitor based restoration even after scarring. *Acta Biomaterialia* 44:209-220.
99. Gu X*, et al.* (2017) Sustained viral gene delivery from a micro-fibrous, elastomeric cardiac patch to the ischemic rat heart. *Biomaterials* 133:132-143.
100. Hassaballah AI, Hassan MA, Mardi AN, & Hamdi M (2013) An Inverse Finite Element Method for Determining the Tissue Compressibility of Human Left Ventricular Wall during the Cardiac Cycle. *Plos One* 8(12).
101. Wang HM*, et al.* (2013) Structure-based finite strain modelling of the human left ventricle in diastole. *Int J Numer Meth Bio* 29(1):83-103.
102. Gao H, Carrick D, Berry C, Griffith BE, & Luo XY (2014) Dynamic finite-strain modelling of the human left ventricle in health and disease using an immersed boundary-finite element method. *Ima J Appl Math* 79(5):978-1010.
103. Hall JE (2015) *Guyton and Hall textbook of medical physiology e-Book* (Elsevier Health Sciences).
104. Mielniczuk LM*, et al.* (2007) Left ventricular end-diastolic pressure and risk of subsequent heart failure in patients following an acute myocardial infarction. *Congest Heart Fail* 13(4):209-214.
105. Guccione JM & Mcculloch AD (1993) Mechanics of Active Contraction in Cardiac-Muscle .1. Constitutive Relations for Fiber Stress That Describe Deactivation. *J Biomech Eng-T Asme* 115(1):72-81.
106. Guccione JM, Waldman LK, & Mcculloch AD (1993) Mechanics of Active Contraction in Cardiac-Muscle .2. Cylindrical Models of the Systolic Left-Ventricle. *J Biomech Eng-T Asme* 115(1):82-90.
107. Rodriguez EK, Omens JH, Waldman LK, & Mcculloch AD (1993) Effect of Residual-Stress on Transmural Sarcomere-Length Distributions in Rat Left-Ventricle. *Am J Physiol* 264(4):H1048-H1056.
108. Walker JC*, et al.* (2008) Magnetic resonance imaging-based finite element stress analysis after linear repair of left ventricular aneurysm. *J Thorac Cardiov Sur* 135(5):1094-U1057.
109. Goktepe S, Abilez OJ, & Kuhl E (2010) A generic approach towards finite growth with examples of athlete's heart, cardiac dilation, and cardiac wall thickening. *J Mech Phys Solids* 58(10):1661-1680.
110. Himpel G, Kuhl E, Menzel A, & Steinmann P (2005) Computational modelling of isotropic multiplicative growth. *Cmes-Comp Model Eng* 8(2):119-134.
111. Genet M, Lee LC, Baillargeon B, Guccione JM, & Kuhl E (2016) Modeling Pathologies of Diastolic and Systolic Heart Failure. *Ann Biomed Eng* 44(1):112-127.
112. Puso MA & Weiss JA (1998) Finite element implementation of anisotropic quasi-linear viscoelasticity using a discrete spectrum approximation. *J Biomech Eng-T Asme* 120(1):62-70.
113. Mazza E & Ehret AE (2015) Mechanical biocompatibility of highly deformable biomedical materials. *Journal of the Mechanical Behavior of Biomedical Materials* 48:100-124.

114. Winter HH & Chambon F (1986) Analysis of Linear Viscoelasticity of a Crosslinking Polymer at the Gel Point. *Journal of Rheology* 30(2):367-382.
115. Chambon F & Winter HH (1987) Linear Viscoelasticity at the Gel Point of a Crosslinking PDMS with Imbalanced Stoichiometry. *Journal of Rheology* 31(8):683-697.
116. Zhang YS & Khademhosseini A (2017) Advances in engineering hydrogels. *Science* 356(6337).
117. Oz MC*, et al.* (2003) Global surgical experience with the acorn cardiac support device. *J Thorac Cardiov Sur* 126(4):983-991.
118. Ghanta RK*, et al.* (2007) Adjustable, physiological ventricular restraint improves left ventricular mechanics and reduces dilatation in an ovine model of chronic heart failure. *Circulation* 115(10):1201-1210.
119. Omens JH, Mackenna DA, & Mcculloch AD (1993) Measurement of Strain and Analysis of Stress in Resting Rat Left-Ventricular Myocardium. *J Biomech* 26(6):665-676.
120. Lin YD*, et al.* (2014) A nanopatterned cell-seeded cardiac patch prevents electro-uncoupling and improves the therapeutic efficacy of cardiac repair. *Biomaterials science* 2(4):567-580.
121. Kutschka I*, et al.* (2006) Collagen matrices enhance survival of transplanted cardiomyoblasts and contribute to functional improvement of ischemic rat hearts. *Circulation* 114(1 Suppl):I167-173.
122. Simpson D, Liu H, Fan TH, Nerem R, & Dudley SC, Jr. (2007) A tissue engineering approach to progenitor cell delivery results in significant cell engraftment and improved myocardial remodeling. *Stem cells (Dayton, Ohio)* 25(9):2350-2357.
123. Liang S*, et al.* (2018) Paintable and Rapidly Bondable Conductive Hydrogels as Therapeutic Cardiac Patches. *Advanced Materials*:1704235.
124. Efraim Y*, et al.* (2017) Biohybrid cardiac ECM-based hydrogels improve long term cardiac function post myocardial infarction. *Acta Biomater* 50:220-233.
125. Ravi S*, et al.* (2012) Effect of bone marrow-derived extracellular matrix on cardiac function after ischemic injury. *Biomaterials* 33(31):7736-7745.
126. Friis E, Lakes R, & Park J (1988) Negative Poisson's ratio polymeric and metallic foams. *Journal of Materials Science* 23(12):4406-4414.
127. Hengsbach S & Lantada AD (2014) Direct laser writing of auxetic structures: present capabilities and challenges. *Smart Mater Struct* 23(8).
128. Bertoldi K, Reis PM, Willshaw S, & Mullin T (2010) Negative Poisson's Ratio Behavior Induced by an Elastic Instability. *Adv Mater* 22(3):361-+.
129. Sha ZD*, et al.* (2017) Metallic glass-based chiral nanolattice: Light weight, auxeticity, and superior mechanical properties. *Mater Today* 20(10):569-576.
130. Choi J & Lakes R (1991) Design of a fastener based on negative Poisson's ratio foam. *Cellular Polymers* 10(3):205-212.
131. Evans KE & Alderson A (2000) Auxetic materials: Functional materials and structures from lateral thinking! *Adv Mater* 12(9):617-+.
132. Scarpa F, Ciffo LG, & Yates JR (2004) Dynamic properties of high structural integrity auxetic open cell foam. *Smart Materials & Structures* 13(1):49-56.
133. Papadopoulou A, Laucks J, & Tibbits S (2017) Auxetic materials in design and architecture. *Nat Rev Mater* 2(12).

134. Veronda DR & Westmann RA (1970) Mechanical Characterization of Skin-Finite Deformations. *J Biomech* 3(1):111-&.
135. Lees C, Vincent JF, & Hillerton JE (1991) Poisson's ratio in skin. *Bio-medical materials and engineering* 1(1):19-23.
136. Williams JL & Lewis JL (1982) Properties and an Anisotropic Model of Cancellous Bone from the Proximal Tibial Epiphysis. *J Biomech Eng-T Asme* 104(1):50-56.
137. Gatt R*, et al.* (2015) Negative Poisson's ratios in tendons: An unexpected mechanical response. *Acta Biomater* 24:201-208.
138. Vanderwal P (1989) Structural and Material Design of Mature Mineralized Radula Teeth of Patella-Vulgata (Gastropoda). *J Ultra Mol Struct R* 102(2):147-161.
139. Blaber J, Adair B, & Antoniou A (2015) Ncorr: Open-Source 2D Digital Image Correlation Matlab Software. *Exp Mech* 55(6):1105-1122.
140. Preibisch S, Saalfeld S, & Tomancak P (2009) Globally optimal stitching of tiled 3D microscopic image acquisitions. *Bioinformatics* 25(11):1463-1465.
141. Tandon GP & Weng GJ (1984) The Effect of Aspect Ratio of Inclusions on the Elastic Properties of Unidirectionally Aligned Composites. *Polym Composite* 5(4):327-333.
142. Tucker CL & Liang E (1999) Stiffness predictions for unidirectional short-fiber composites: Review and evaluation. *Compos Sci Technol* 59(5):655-671.
143. Liu XN, Huang GL, & Hu GK (2012) Chiral effect in plane isotropic micropolar elasticity and its application to chiral lattices. *J Mech Phys Solids* 60(11):1907-1921.
144. Greaves GN, Greer AL, Lakes RS, & Rouxel T (2011) Poisson's ratio and modern materials. *Nat Mater* 10(11):823-837.
145. Song F, Zhou JB, Xu XH, Xu Y, & Bai YL (2008) Effect of a negative Poisson ratio in the tension of ceramics. *Phys Rev Lett* 100(24).
146. Rinkevich AB, Perov DV, Samoilovich MI, & Kleshcheva SM (2010) Elastic properties and heat capacity of opal matrices and related 3D-nanocomposite materials. *Phys Solid State+* 52(12):2570-2576.
147. Saxena KK, Das R, & Calius EP (2016) Three Decades of Auxetics Research - Materials with Negative Poisson's Ratio: A Review. *Adv Eng Mater* 18(11):1847-1870.
148. O'neill J (2014) Antimicrobial resistance: tackling a crisis for the health and wealth of nations. *Rev. Antimicrob. Resist* 20:1-16.
149. Adeyi O*, et al.* (2017) Drug-resistant infections: a threat to our economic future. *World Bank Group, Washington, DC*.
150. United I (2019) No Time to Wait–Securing the Future from Drug-resistant Infections. *Report to the Secretary General of the Nations*.
151. Lewis K (2010) Persister Cells. *Annu Rev Microbiol* 64:357-372.
152. Jung D, Rozek A, Okon M, & Hancock REW (2004) Structural transitions as determinants of the action of the calcium-dependent antibiotic daptomycin. *Chem Biol* 11(7):949-957.
153. Zhang TH, Muraih JK, MacCormick B, Silverman J, & Palmer M (2014) Daptomycin forms cation- and size-selective pores in model membranes. *Bba-Biomembranes* 1838(10):2425-2430.
154. Silverman JA, Perlmutter NG, & Shapiro HM (2003) Correlation of daptomycin bactericidal activity and membrane depolarization in Staphylococcus aureus. *Antimicrob Agents Ch* 47(8):2538-2544.
155. Kim W*, et al.* (2018) A new class of synthetic retinoid antibiotics effective against

bacterial persisters. *Nature* 556(7699):103-+.
156. Jiang Y, Lookman T, & Saxena A (2000) Phase separation and shape deformation of two-phase membranes. *Phys Rev E* 61(1):R57-R60.
157. Brogden KA (2005) Antimicrobial peptides: Pore formers or metabolic inhibitors in bacteria? *Nat Rev Microbiol* 3(3):238-250.
158. Stachowiak JC, Hayden CC, & Sasaki DY (2010) Steric confinement of proteins on lipid membranes can drive curvature and tubulation. *P Natl Acad Sci USA* 107(17):7781-7786.
159. Lipowsky R (1992) Budding of Membranes Induced by Intramembrane Domains. *J Phys Ii* 2(10):1825-1840.
160. Julicher F & Lipowsky R (1996) Shape transformations of vesicles with intramembrane domains. *Phys Rev E* 53(3):2670-2683.
161. Jarvis TJ, Donohue MD, & Katz JL (1975) Bubble Nucleation Mechanisms of Liquid Droplets Superheated in Other Liquids. *J Colloid Interf Sci* 50(2):359-368.
162. Friedman R, Pellarin R, & Caflisch A (2009) Amyloid Aggregation on Lipid Bilayers and Its Impact on Membrane Permeability. *J Mol Biol* 387(2):407-415.
163. Pokorny A & Almeida PFF (2004) Kinetics of dye efflux and lipid flip-flop induced by delta-lysin in phosphatidylcholine vesicles and the mechanism of graded release by amphipathic, alpha-helical peptides. *Biochemistry-Us* 43(27):8846-8857.
164. Pokorny A & Almeida PFF (2005) Permeabilization of raft-containing lipid vesicles by delta-lysin: A mechanism for cell sensitivity to cytotoxic peptides. *Biochemistry-Us* 44(27):9538-9544.
165. Jackman JA*, et al.* (2018) Therapeutic treatment of Zika virus infection using a brain-penetrating antiviral peptide. *Nat Mater* 17(11):971-+.
166. Jackman JA, Saravanan R, Zhang YB, Tabaei SR, & Cho NJ (2015) Correlation between Membrane Partitioning and Functional Activity in a Single Lipid Vesicle Assay Establishes Design Guidelines for Antiviral Peptides. *Small* 11(20):2372-2379.
167. Jackman JA, Zan GH, Zhdanov VP, & Cho NJ (2013) Rupture of Lipid Vesicles by a Broad-Spectrum Antiviral Peptide: Influence of Vesicle Size. *J Phys Chem B* 117(50):16117-16128.
168. Biria A, Maleki M, & Fried E (2013) Continuum Theory for the Edge of an Open Lipid Bilayer. *Adv Appl Mech* 46:1-68.
169. Tu ZC & Ou-Yang ZC (2003) Lipid membranes with free edges. *Phys Rev E* 68(6).
170. Helfrich W (1973) Elastic Properties of Lipid Bilayers - Theory and Possible Experiments. *Z Naturforsch C* C 28(11-1):693-703.
171. Yi X, Shi XH, & Gao HJ (2011) Cellular Uptake of Elastic Nanoparticles. *Phys Rev Lett* 107(9).
172. Zelisko M, Ahmadpoor F, Gao HJ, & Sharma P (2017) Determining the Gaussian Modulus and Edge Properties of 2D Materials: From Graphene to Lipid Bilayers. *Phys Rev Lett* 119(6).
173. Hu MY, Briguglio JJ, & Deserno M (2012) Determining the Gaussian Curvature Modulus of Lipid Membranes in Simulations. *Biophys J* 102(6):1403-1410.
174. Yuan HY, Huang CJ, Li J, Lykotrafitis G, & Zhang SL (2010) One-particle-thick, solvent-free, coarse-grained model for biological and biomimetic fluid membranes. *Phys Rev E* 82(1).
175. Plimpton S (1995) Fast Parallel Algorithms for Short-Range Molecular-Dynamics. *J*

Comput Phys 117(1):1-19.
176. Tolpekina TV, den Otter WK, & Briels WJ (2004) Simulations of stable pores in membranes: System size dependence and line tension. *J Chem Phys* 121(16):8014-8020.
177. Boal D & Boal DH (2012) *Mechanics of the Cell* (Cambridge University Press).
178. Fu SP, Peng Z, Yuan H, Kfoury R, & Young YN (2017) Lennard-Jones type pair-potential method for coarse-grained lipid bilayer membrane simulations in LAMMPS. *Comput Phys Commun* 210:193-203.
179. Zhelev DV & Needham D (1993) Tension-Stabilized Pores in Giant Vesicles - Determination of Pore-Size and Pore Line Tension. *Biochim Biophys Acta* 1147(1):89-104.
180. Evans E & Ludwig F (2000) Dynamic strengths of molecular anchoring and material cohesion in fluid biomembranes. *J Phys-Condens Mat* 12(8a):A315-A320.
181. Loi S, Sun G, Franz V, & Butt HJ (2002) Rupture of molecular thin films observed in atomic force microscopy. II. Experiment. *Phys Rev E* 66(3).
182. Veatch SL & Keller SL (2003) Separation of liquid phases in giant vesicles of ternary mixtures of phospholipids and cholesterol. *Biophys J* 85(5):3074-3083.
183. Givli S, Giang H, & Bhattacharya K (2012) Stability of Multicomponent Biological Membranes. *Siam J Appl Math* 72(2):489-511.
184. Reynwar BJ*, et al.* (2007) Aggregation and vesiculation of membrane proteins by curvature-mediated interactions. *Nature* 447(7143):461-464.